OPTIMIZATION AND CONTROL OF VIRUS-HOST SYSTEMS

A Dissertation
Presented to
The Academic Faculty

By

Guanlin Li

In Partial Fulfillment
of the Requirements for the Degree
Doctor of Philosophy in the
Quantitative Biosciences in the School of Physics

Georgia Institute of Technology

August 2021

OPTIMIZATION AND CONTROL OF VIRUS-HOST SYSTEMS

Thesis committee:

Dr. Joshua S. Weitz, Advisor
School of Biological Sciences
School of Physics
Georgia Institute of Technology

Dr. Yao Yao, Co-advisor
School of Mathematics
Georgia Institute of Technology

Dr. Yorai Wardi
School of Electrical and Computer Engineering
Georgia Institute of Technology

Dr. Sam Brown
School of Biological Sciences
Georgia Institute of Technology

Dr. Kurt Wiesenfeld
School of Physics
Georgia Institute of Technology

Date approved: May 24, 2021

ACKNOWLEDGMENTS

To start, I would like to express my sincere gratitude to my advisor, Dr. Joshua S. Weitz, for his guidance and support. Joshua has consistently inspired and driven me to become an independent researcher and thinker. Joshua has been an exceptional mentor. He has not only guided me in research, but he has also been an inspiring leader who has taught me the importance of being a consistent, enthusiastic, energetic, and responsible scientist. If I could do it again, I would choose to join the Weitz group without hesitation. I am also grateful to my co-advisor, Dr. Yao Yao. In addition to guidance about careers in academia and industry, she provided exceptional and mathematically-rigorous feedback on projects, I consider her a friend and mentor.

There are a few more individuals I would like to thank who have been influential to me. I would like to thank Dr. Sebastien Motsch at Arizona State University, who helped me to implement efficient computer programs and write rigorous mathematical proof. He has helped me build a solid foundation for my research career. I am also grateful to Dr. Yingjie Liu, who sparked my passion for solving systems of partial differential equations with efficient numerical schemes. Without his help, I wouldn't have been able to generate such a satisfied outcome in my work on scientific computing.

In addition, I thank my former research supervisors: Dr. Hal L. Smith, Dr. Kuang Yang, Dr. Howie Weiss and Dr. Rachel Kuske. They have offered valuable guidance on numerous quantitative biology projects, from deterministic systems to stochastic systems; from ecological dynamics to chemical kinetics, I was indeed intrigued by the emergent behaviors from these complex biological systems. I appreciate Dr. Michael H. Cortez, Dr. Michael E. Hochberg and Dr. Laurent Debarbieux for providing feedback and fruitful advice on our collaborations. I would also like to thank Dr. Yorai Wardi who has given invaluable feedback, proving a control-theoretic grounding for problems. Last but not least, I would also like to thank the rest of my thesis committee: Dr. Sam Brown and Dr. Kurt

Weisenfeld.

Also, I am sincerely grateful to my colleagues and mentors in the Weitz group: Dr. Stephen Beckett, Dr. David Demory, Dr. Adriana Lucia-Sanz, Dr. Jessica Irons, Dr. Shengyun Peng, Dr. Yu-Hui Lin, Ashley Coenen, Daniel Muratore, Rogelio Rodriguez, Marian Dominguez Mirazo, Andreea Magalie, Quan (King) Nguyen, Audra Davidson, Qi An, and Rong Jin, and special thanks to Shashwat Shivam for productive collaborations and inspiring conversations. I have also greatly benefited from guidance from Dr. Jacopo Marchi, Dr. Joey Leung and Dr. Jeremy Harris.

I would also like to acknowledge the funding sources (my PI's grants) that supported me during my graduate studies. I would like to acknowledge the Army Research Office (W911NF-14-1-0402 and W911NF1910384), the National Institutes of Health (1R01AI146592-01) and the National Science Foundation (1806606 and 2032082).

Outside the labs, I am lucky to have met all my friends and I would like to thank them for the memorable moments that we shared together. Special thanks to Yingzheng Liu, Ningquan Wang, Shichao Zhang, Enpeng Yuan, Yan Li, Jianshu Zhao, Weihao Tang and Haochi Si for the inspiring discussions about science and life. Thank you all for always being there for me.

Lastly, I thank my parents Huijun Li and Haiyun Yang, as well as my significant other Dandi Zhang for their unconditional and unfailing love, encouragement, and support.

TABLE OF CONTENTS

LIST OF TABLES

LIST OF FIGURES

SUMMARY

Optimization and control are powerful tools to design a system that works as effectively as possible. Mathematical optimization and control methods are widely used in engineering and science. In this thesis, we focus on applications of model-based optimization and control in complex virus-host systems. The model-based optimization and control frameworks usually deal with modeling complex systems, and the model components are (partially) known or estimated from data. We combine dynamical models of virus-host systems with optimization- and control-theoretic principles to improve two specific decision-making processes: (1) devise and improve the timing and composition of therapeutic phage cocktails in phage therapy; (2) design non-pharmacological interventions to reduce fatalities arising from COVID-19 while also enabling economic engagement.

Viruses that infect bacteria, *i.e.,* bacteriophage or 'phage', are increasingly considered as treatment options for the control and clearance of bacterial infections, particularly as compassionate use therapy for multi-drug resistant infections. In practice, clinical use of phage often involves the application of multiple therapeutic phage, either together or sequentially. However, the selection and timing of therapeutic phage delivery remains largely ad hoc. Here, we evaluate principles underlying why careful application of multiple phage (*i.e.,* a 'cocktail') might lead to therapeutic success in contrast to the failure of single-strain phage therapy to control an infection. We combine dynamical modeling of phage, bacteria, and host immune cell populations with control-theoretic principles (via optimal control theory) to devise phage cocktails and delivery schedules to control the bacterial populations. The objective is to optimize the timing and composition of therapeutic phage cocktails that leads to therapeutic success. Although single-strain phage therapy in immunodeficient hosts can fail due to phage resistance, our optimal control analysis shows that a two-phage cocktail that includes a counter-resistant phage can restore therapeutic efficacy in immunodeficient hosts. Furthermore, we leverage optimal control theoretic findings as a guide for

practical use, and show that the practical schemes (discretized version) could also lead to the same benefit.

A risk in using cocktails of different phage is that bacteria could simultaneously develop resistance to all injected phage (*i.e.,* selecting for multi-phage resistant). The next step is to understand how to pre-select phage that have adapted via co-evolution with bacterial strains and then to efficiently use these 'future' phage (*i.e.,* identified from co-evolutionary training) to clear the infection early on, before new phage-resistant bacteria can arise. We develop the evolutionarily robust phage therapy in immunodeficient hosts given the infection networks that was identified in co-evolutionary training. Our computational results provide several important insights to guide the phage therapy in complex eco-evolutionary dynamics: (1) including a contingent specialist phage in multiphage cocktails may lead to the outcome of competitive release; (2) the prey-predator oscillatory dynamics may play a critical role for the cocktail treatment with a generalist phage.

Optimization and control not only can be applied to bacteria-phage-immune systems (*i.e.,* at the microbial level) to help design phage therapy, but also can be applied to epidemiological systems (*i.e.,* at the large-scale population level) to guide the development and deployment of efficient interventions. The COVID-19 pandemic has precipitated a global health crisis; multiple public health strategies are being deployed to slow the coronavirus pandemic. Lockdowns and stay-at-home orders have reduced the transmission of SARS-CoV-2, but have come with significant social and economic costs. The use of *en masse* interventions has stemmed, in part, from the absence of sufficient testing capacity to enable personalized changes to individualized behavior. In this section of the thesis, we describe a control theory framework combining population-scale viral and serological testing as part of an individualized approach to control COVID-19 spread. The aim is to develop policies for modulating individualize contact rates depending on both personalized disease status and the status of the epidemic at the population scale. In doing so, we provide evidence that lockdowns could be relaxed far more rapidly, and potentially avoided

altogether, in the event that infectious individuals are isolated efficiently given sufficiently widespread testing for SARS-CoV-2, and recovered individuals increase their interactions to dilute potentially risky interactions between susceptible and infectious individuals.

Altogether in this thesis, we apply control strategies to alleviate the burden or spread of disease at multiple scales. At microbial level, we advance efforts to guide future development and deployment of therapeutic phage cocktails for clinical translation. At the population level, we show how to move from *en masse* to individualized approaches to changing behavior during a pandemic. This work also illustrates the capabilities and benefits that mathematical optimization and control can bring to research at the intersection of biology, immunology and epidemiology.

CHAPTER 1

INTRODUCTION AND BACKGROUND

Some materials are adapted from:

Li, G., Leung, C.Y.*, Wardi, Y., Debarbieux, L. and Weitz, J.S., 2020. Optimizing the Timing and Composition of Therapeutic Phage Cocktails: A Control-theoretic Approach. Bulletin of Mathematical Biology, 82(6), pp.1-29.*

Li, G., Shivam, S.*, Hochberg, M.E., Wardi, Y. and Weitz, J.S., 2020. Disease-dependent interaction policies to support health and economic outcomes during the COVID-19 epidemic. Available at SSRN 3709833.*

Weitz, J.S., Beckett, S.J., Coenen, A.R., Demory, D., Dominguez-Mirazo, M., Dushoff, J., Leung, C.Y., Li, G., Măgălie, A., Park, S.W., Rodriguez-Gonzalez, R., Shivam, S. and Zhao, C.Y., 2020. Modeling shield immunity to reduce COVID-19 epidemic spread. Nature medicine, 26(6), pp.849-854.

1.1 Phage therapy for control of bacterial infections

The spread of multi-drug resistant (MDR) pathogens is a global public health crisis [1]. The emergence and spread of multi-antibiotic resistant pathogens has spurred research and development of alternative antimicrobials, including phage [2, 3, 4, 5, 6, 7, 8, 9, 10, 11]. Phage have been applied in compassionate use scenarios, for example, to successfully cure patients both in the USA and in Europe [12, 13, 8, 9, 14], catalyzing the 2018 launch of the first North American phage therapy center based at UCSD (IPATH). Yet, despite individual successes, phage therapy has a mixed record in controlled clinical trials. For instance, a large-scale trial involving more than 200 patients failed to demonstrate that phage treatment improved outcomes for children infected by *Escherichia coli* with symptoms of severe diarrhea in Bangladesh [15]. Similarly, the recent European phase II clinical trial to treat

burn wound patients failed to show superiority compared to a reference treatment [16].

Phage dose and the time interval between doses are critical to the effectiveness of phage therapy [17]. Control theory may be a useful approach to address the problem of optimizing the dosage, timing, and composition of therapeutic agents. For example, control theory has been applied to optimize antiretroviral drug therapy for HIV infections [18, 19, 20, 21], minimize resistance in antibiotic treatment [22], and determine the optimal dosing schedule of antimalarial medications [23] and cancer therapies [24, 25, 26]. These applications of control theory have focused on modeling the within-host disease dynamics using a set of coupled nonlinear differential equations describing the population dynamics of disease agents such as pathogens or tumor cells, as well as host cells that include immune cells and/or cells targeted by pathogens. The cost function to be minimized is then chosen to balance a number of treatment goals, including minimizing pathogen/tumor load, maximizing healthy cell populations, and limiting treatment costs and toxicity.

As examples beyond within-host treatments of diseases, control theory has also been applied to optimize strategies in controlling between-host transmission of infections. In these studies, the spread of the infectious disease is modeled by standard epidemiological models such as the Susceptible-Infected-Susceptible (SIS) model or the Susceptible-Infected-Recovered (SIR) model. The control strategies consist of epidemiological interventions such as vaccination, sanitation, and treatment of infected individuals. The cost function is determined based on minimization of the infected population or number of deaths subjected to costs of the control efforts. Such epidemiological applications of control theory have been used to optimize control strategies in vector-borne diseases [27], cholera epidemics [28], anthrax infection in animals [29], and infectious disease with two strains of pathogens [30].

In Chapter 2, we develop a control-theoretic framework to optimize monophage therapy and multiphage (cocktail) treatment of immunodeficient hosts and in other scenarios where standard phage therapy is likely to fail. We use a nonlinear dynamics model of within-host

interactions to show that a combination of fast intra-host phage decay, evolution of phage resistance amongst bacteria, and/or compromised immune response might limit the effectiveness of single-strain phage therapy. To resolve these problems, we combine dynamical modeling of phage, bacteria, and host immune cell populations with control-theoretic principles (via optimal control theory) to devise evolutionarily robust phage cocktails and delivery schedules to control the bacterial populations. Our numerical results suggest that optimal administration of single-strain phage therapy may be sufficient for curative outcomes in immunocompetent patients, but may fail in immunodeficient hosts due to phage resistance. We show that optimized treatment with a two-phage cocktail that includes a counter-resistant phage can restore therapeutic efficacy in immunodeficient hosts.

The above introduction materials (Chapter 1.1) and results presented for this work (Chapter 2) are published [31].

In prior work [32] and on-going research, our collaborators have found that strain *PAK* exposed to phage *PAK_P1* leads to the growth of phage-resistant strains, the *PAK_P1*-resistant bacterium is labeled as *PAK_rP1*. A novel phage named *PAK_P6* can infect *PAK_rP1*. However, the exposure of strain *PAK_rP1* to phage *PAK_P6* selected for a novel resistant bacterium named *PAK_rP6*. Then, the bacterium *PAK_rP6* was used to isolate another phage, named *PAK_P10*. Therefore, selection of phage-resistant mutants in a sequential therapeutic treatment could continue indefinitely (for instance the emergence of *PAK_P10* phage-resistant bacterium) if the bacteria pathogens are not eliminated. Furthermore, a risk in using cocktails of different phage is that bacteria could simultaneously develop resistance to all injected phage (multi-resistant bacteria, [33]).

A novel idea to combat the evolution of phage resistance is 'training' phage to evolve to counter resistance before using them in therapy. Recent *in vitro* experiments successfully showed that coevolutionary phage training could lead to greater bacterial suppression and delays the evolution of phage resistance [34]. In Chapter 3, we focus on the second half of this task. We propose a theoretical framework in order to identify a recipe for a phage

therapy treatment strategy in immunodeficient hosts, that may be more robust to evolution of phage-resistance against administered phage.

1.2 Non-pharmaceutical COVID-19 control

As of 7 March 2021, more than 116,166,652 cases of coronavirus disease 2019 (COVID-19) have been reported worldwide with more than 2,582,528 deaths globally [35]. Starting at the reported origin of the pandemic in Wuhan, China, control measures have been implemented in most countries where outbreaks have occurred [36, 37, 38, 39, 40, 41]. Multiple public health strategies are being deployed to slow outbreaks, and although recommendations always include social distancing and isolation of confirmed cases, the full spectrum of measures and levels of adherence differ from country to country, making assessments of strategy efficacy difficult (see [36], controversy surrounding [42]).

The non-pharmaceutical control strategies for COVID-19 largely follow those employed in previous viral epidemics, including SARS, Ebola and MERS. Initial strategies can be broadly grouped into mitigation and suppression, where the former attempts to preserve essential health care services and contain morbidity and mortality, whereas the latter imposes more severe, emergency restrictions to prevent health care system collapse and provide conditions for easing-off towards less intense mitigation strategies [43]. Both mitigation and suppression approaches carry considerable social and economic costs, meaning that policymakers and the public at large only adopt them for short time periods [44]. A problem is that control measures have often been applied irrespective of an individual's disease status (and/or likely infection risk severity) and are driven, in part, by the absence of information-driven alternatives.

Hence, distinct from lockdowns, there is an increasing interest in implementing population-wide prevention methods that decrease transmission risk while enabling economic re-engagement. Examples of such measures include mask-wearing [45, 46], contact-free interactions [47], and restructuring of physical spaces [48]. The use of masks, in particular, has been shown

to be effective at reducing respiratory transmission of SARS-CoV-2, particularly when individuals in a potentially infectious interaction routinely wear them [49, 50]. These population-wide measures still carry uncertainty since individuals are expected to behave uniformly irrespective of their disease status. COVID-19 screening provides a complementary route, and despite costs may confer both health and economic benefit [51] to overcome the negative impact on the economy due to pandemic-related shutdowns [52]. As the scale of COVID-19 testing has increased, jurisdictions may also have an opportunity to consider implementing tactical mitigation strategies informed by testing.

Non-pharmaceutical COVID-19 control until effective vaccines become widely available will necessarily involve periods of reduced social and economic activity; *i.e.,* 'business, but not as usual'. Control efforts are already generating hardship and could in the longer-term result in social unrest and increased mortality [53, 54, 55]. In Chapter 4, we confront a joint problem: how to identify policies that aim to reduce fatalities arising from COVID-19 while also enabling economic engagement. First, we use optimal control to assess both health and economic outcomes in an SEIR disease model framework. There is a substantial and growing literature on optimal control for COVID-19, the bulk of which focuses on non-personalized release policies or policies that target age- or risk-stratified groups [56, 36, 57, 43, 58, 59]. Here, we identify optimal control policies to modulate interaction rates based on disease - unifying prior efforts centered on isolation and *shield immunity*. We find that intermediate policy outcomes can do nearly as well as strict public health scenarios, without incurring the severe costs as suppression-centered policies. However, optimal controls can be fragile, when applied in practice given that they rely on time- rather than state-based interventions; the consequence of mistiming interventions can be severe [58]. Hence, guided by the optimal control analysis, we identify state-dependent policies similar to feedback control that provide actionable guidance for individual behavior. As we show, using population-wide PCR testing for infection alongside immune status can reduce COVID-19 transmission while enabling more individuals to return to work

sooner and with fewer restrictions than would otherwise be possible.

Furthermore, we show that targeted shield immunity could also enhance population outcomes by focusing the effort of recovered individuals in subsets of the population. By formulating an optimization problem for targeted (age-specific) shield immunity in an age-structured epidemiological intervention model, we find that, preferentially targeting older individuals by shielding those at highest risk, it is possible to further reduce cumulative deaths by 30%.

The above introduction materials (Chapter 1.2) and results presented for this work (Chapter 4) are accepted for iScience journal publication (a pre-print can be found at [60]) and published at [61].

CHAPTER 2

OPTIMIZING THE TIMING AND COMPOSITION OF THERAPEUTIC PHAGE COCKTAILS: A CONTROL-THEORETIC APPROACH

Adapted from Li, G., Leung, C.Y.*, Wardi, Y., Debarbieux, L. and Weitz, J.S., 2020. Optimizing the Timing and Composition of Therapeutic Phage Cocktails: A Control-theoretic Approach. Bulletin of Mathematical Biology, 82(6), pp.1-29.*

2.1 Introduction

A number of mathematical models for phage-bacteria population dynamics with focus on implications for phage therapy have been proposed [62, 63, 64]. These models account for the ecological interactions between phage and bacteria, but do not explicitly consider the effects of host immune response, which is an important driver of within-host infection dynamics. Other proposed models have incorporated the interactions between bacteria, phage and host immune cells [65, 66, 67], but do not include features of realistic immune responses, including a bounded immune activation rate as well as density-dependence clearance rates of pathogens by immune cells.

Building on earlier models [65, 66], a subset of us have developed phage therapy models in prior work that consider key immunological features including saturation of immune activation and immune evasion by bacteria at high pathogen density [68]. Combined with animal experiments, the results have shown that bacterial populations are not necessarily eliminated by either phage or the immune response alone. Instead, bacteria are eliminated when phage and the immune response work in synergy [69]. Importantly, curative success was not inevitable. For example, phage therapy was ineffective in innate immune activation deficient hosts and neutropenic hosts. Therapeutic failure was caused by the spread of phage-resistant bacteria as predicted by the mathematical models. Such failure raises a

new challenge: is it possible to rationally combine phage strains, dosage, and targeting to overcome therapeutic failure in immunodeficient hosts and in other scenarios such as rapid phage clearance from the host?

In this chapter, we introduce a mathematical model of phage therapy and define the control problem. Second, we analyze the optimal control problem, show that the optimal control solution exists, and derive the necessary conditions for the optimal control via Prontryagin's maximum principle [70]. Then, we implement a Hamiltonian-based algorithm [71, 72] to numerically compute the optimal control solutions for monophage therapy and a phage cocktail treatment consisting of two phage strains. The numerical results are presented and followed by a discussion.

2.2 Problem formulation

2.2.1 A mathematical model of phage therapy

We propose a phage therapy model that considers the nonlinear dynamics arising from interactions between sensitive bacteria S, phage-resistant bacteria R, phage P_S (i.e., only targeting sensitive bacteria), phage P_R (i.e., only targeting phage-resistant bacteria) and the host innate immune response I, see Fig. 2.1. Hence, this model intentionally makes the assumption that phage are specialized in their infection of bacteria; generalizations of this approach are considered in the Discussion. Two strains of bacteria (S and R) reproduce given the limited environmental capacity K_C. The phage-resistant bacteria emerge from sensitive bacteria through mutation with a fixed probability μ per cellular division. Both strains of bacteria are killed by the immune response and both stimulate immune activation. The immune response is stimulated by the presence of bacteria with a maximum activation rate α until it reaches the maximum capacity K_I. Phage populations P_S and P_R infect and lyse sensitive and phage-resistant bacterial populations at rates $F(P_S)$ and $F(P_R)$ respectively. In this study, we assume that the two phage types (P_S and P_R) have identical adsorption rate ϕ, burst size β and decay rate ω for simplicity. In general, these

three trait parameters can be strain-specific, and the optimal control analysis and simulation procedures will be the same. We consider the phage decay rate to be independent of the host immune response in accordance with prior experimental work in acute pneumonia that showed the phage introduction did not elicit a differential cytokine response when administered intranasally [69]. It is possible that other strains of phage or alternative administration routes could lead to an immunity-dependent phage clearance rate as considered in other models [67]. The treatments inject phage into the system, the injection rates of phage P_S and phage P_R at time t are $\rho_S(t)$ and $\rho_R(t)$ respectively. The dynamics of bacteria, phage and the innate immune system can be modeled using the following system of nonlinear differential equations,

$$
\begin{aligned}
\dot{S} &= \overbrace{rS\left(1-\frac{S+R}{K_C}\right)(1-\mu)}^{\text{logistic growth, mutation}} - \overbrace{SF(P_S)}^{\text{lysis}} - \overbrace{\frac{\epsilon IS}{1+(S+R)/K_D}}^{\text{immune killing}} \\
\dot{R} &= \overbrace{r'R\left(1-\frac{S+R}{K_C}\right)}^{\text{logistic growth}} + \overbrace{\mu rS\left(1-\frac{S+R}{K_C}\right)}^{\text{mutation from sensitive host}} - \overbrace{RF(P_R)}^{\text{lysis}} - \overbrace{\frac{\epsilon IR}{1+(S+R)/K_D}}^{\text{immune killing}} \\
\dot{P}_S &= \overbrace{\beta SF(P_S)}^{\text{release of viruses}} - \overbrace{\phi SP_S}^{\text{adsorption}} - \overbrace{\omega P_S}^{\text{decay}} + \overbrace{\rho_S(t)}^{\text{phage injection}} \\
\dot{I} &= \overbrace{\alpha I\left(1-\frac{I}{K_I}\right)\left(\frac{S+R}{S+R+K_N}\right)}^{\text{immune stimulation, activation and immune saturation}} \\
\dot{P}_R &= \overbrace{\beta RF(P_R)}^{\text{release of viruses}} - \overbrace{\phi RP_R}^{\text{adsorption}} - \overbrace{\omega P_R}^{\text{decay}} + \overbrace{\rho_R(t)}^{\text{phage injection}}
\end{aligned}
\tag{2.1}
$$

where $F(P_i) = \phi P_i / \left(1 + \frac{P_i}{P_C}\right)$ for $i \in \{S, R\}$ is the per-capita phage-induced bacterial lysis rate that characterizes the effect of phage saturation during the infection. Specifically, phage saturation occurs when multiple phage adsorb to the same target bacterial cell when at high phage population density. We constrain the injection rates of two phage doses as

following,

$$\rho_S(t) \geq 0,\ \rho_R(t) \geq 0,\ \rho_S + \rho_R(t) \leq \rho_{max},\ \forall t \tag{2.2}$$

where ρ_{max} is the fixed maximal injection rate. The goal is to control the phage injection rates $\rho_S(t)$ and $\rho_R(t)$ so as to minimize the bacterial population over the entire treatment and at the final time, while limiting the amount of phage injected into the body (*i.e.,* treatment costs). The specific cost functional associated with this goal will be introduced later in Sect. 2.2.2.

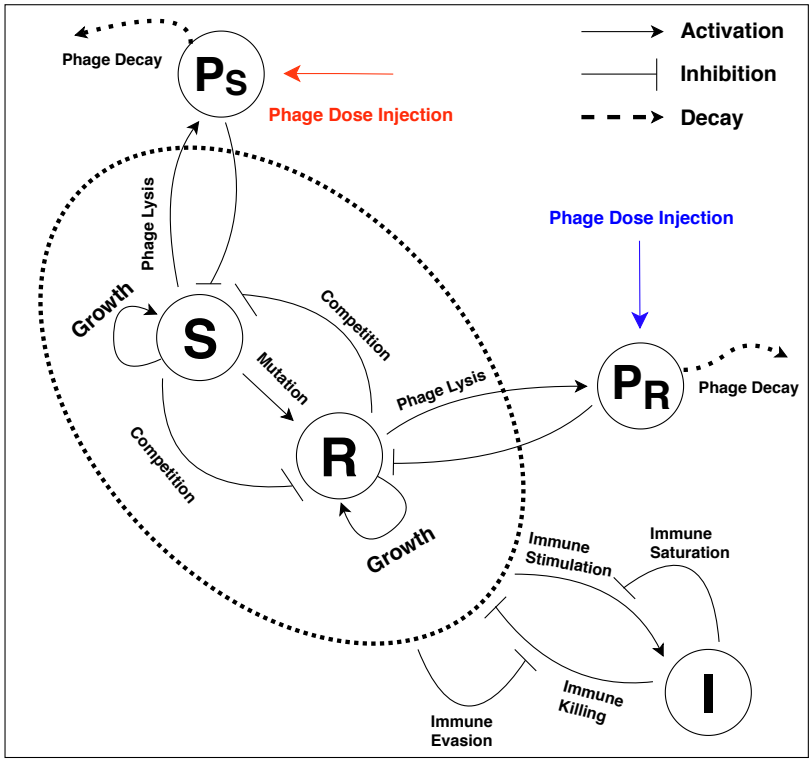

Figure 2.1: Schematic of phage therapy model in the system (2.1). Sensitive bacteria (S) and phage-resistant bacteria (R) are targeted by phage (P_S) and phage (P_R), respectively. Innate immunity (I) is activated by the presence of bacteria and attacks both bacterial strains.

Scaled model. To simplify system (2.1), we rescale state variables and parameters. As the state variables and parameters have different units, we transform them, by scaling, into

non-dimensional variables. Accordingly, the dimensionless state vector x is

$$x = [x_1, x_2, x_3, x_4, x_5]^T = \left[\frac{S}{K_D}, \frac{R}{K_D}, \frac{P_S}{P_C}, \frac{I}{K_I}, \frac{P_R}{P_C}\right]^T, \tag{2.3}$$

where $(\cdot)^T$ is the notation of matrix transpose. The scaled model parameters and control variables are:

$$\begin{gathered}\widetilde{\epsilon} = \epsilon K_I,\ q = \frac{\rho_{max}}{P_C},\ k_{CD} = \frac{K_C}{K_D},\ k_{ND} = \frac{K_N}{K_D},\ k_{PD} = \frac{P_C}{K_D},\ \psi = \phi K_D, \\ u_1(t) = \frac{\rho_S(t)}{\rho_{max}},\ u_2(t) = \frac{\rho_R(t)}{\rho_{max}}.\end{gathered} \tag{2.4}$$

In doing so, the resulting scaled system is

$$\begin{aligned}
\dot{x}_1 &= r x_1 \left(1 - \frac{x_1 + x_2}{k_{CD}}\right)(1-\mu) - k_{PD} x_1 \mathcal{I}(x_3) - \frac{\widetilde{\epsilon} x_4 x_1}{1 + x_1 + x_2} \\
\dot{x}_2 &= r' x_2 \left(1 - \frac{x_1 + x_2}{k_{CD}}\right) + r x_1 \left(1 - \frac{x_1 + x_2}{k_{CD}}\right)\mu - k_{PD} x_2 \mathcal{I}(x_5) - \frac{\widetilde{\epsilon} x_4 x_2}{1 + x_1 + x_2} \\
\dot{x}_3 &= \beta x_1 \mathcal{I}(x_3) - \psi x_1 x_3 - \omega x_3 + q u_1(t) \\
\dot{x}_4 &= \alpha x_4 (1 - x_4) \left(\frac{x_1 + x_2}{x_1 + x_2 + k_{ND}}\right) \\
\dot{x}_5 &= \beta x_2 \mathcal{I}(x_5) - \psi x_2 x_5 - \omega x_5 + q u_2(t),
\end{aligned} \tag{2.5}$$

where $\mathcal{I}(x_i) = \psi x_i / (1 + x_i)$ for $i \in \{3, 5\}$ is the scaled phage infection rate function. Note that the injection rates (ρ_S, ρ_R) are scaled by the maximal injection rate ρ_{max}, the scaled injection rates (u_1, u_2) are interpreted as the relative intensity (or strength) of the maximal injections, we have constrained: $u_1(t) \geq 0$, $u_2(t) \geq 0$ and $u_1(t) + u_2(t) \leq 1,\ \forall t$.

2.2.2 Objective functional

Define the set $U \subset \mathbb{R}^2$ as a convex and compact set, $U = \left\{u \in \mathbb{R}^2_+ \mid \|u\|_1 \leq 1\right\}$ where $\mathbb{R}^d_+$ is the d dimensional non-negative orthant. We define the space of *admissible controls*, denoted by $\mathcal{U}$, as the set of Lebesgue-measurable functions $u : [t_0, t_f] \longrightarrow U$. The cost

functional to be minimized over $\mathcal{U}$ is written in the following Bolza form,

$$\mathcal{J}(u) = \int_{t_0}^{t_f} \theta_B(x_1 + x_2) + \frac{\theta_u}{2} \|u\|_2^2 \; dt + \; \theta_f(x_1(t_f) + x_2(t_f)), \tag{2.6}$$

where θ_B, θ_u and θ_f are the regulator weights. We denote $\mathcal{L}(x, u) = \theta_B(x_1 + x_2) + (\theta_u/2) \|u\|_2^2$ as the *running cost*, which is the integrand of $\mathcal{J}(u)$. The *terminal cost* is denoted as $g(x(t_f)) = \theta_f(x_1(t_f) + x_2(t_f))$. The optimal control problem is

$$\min\{\mathcal{J}(u) | u \in \mathcal{U}\}. \tag{2.7}$$

Such optimal problems may not have solutions in the sense that the minimum in Eq. 2.7 does not exist. Generally the infimum exists, and we denote it by

$$\mathcal{J}^* := \inf\{\mathcal{J}(u) | u \in \mathcal{U}\}. \tag{2.8}$$

Later we prove that for this particular problem the minimum exists (see Sect. **??**), however, there is no guarantee that the minimal solution is piecewise continuous. In practice, the algorithm (see Sect. 2.4.1) computes piecewise-continuous functions, and we mention that the computed solution, defined as the last iteration after the algorithm has stopped, provides an adequate approximation to $\mathcal{J}^*$.

2.3 Analysis of optimal controls

2.3.1 Preliminaries

Positively invariant set. For many complex population dynamics models, the populations remain bounded forward in time, e.g., virus-host interactions [73], vector-borne diseases [27]. The following proposition guarantees the *boundedness* of system (2.5) for any controls $u(t) \in \mathcal{U}$.

Proposition 1. *Let Ω be the following subset of $\mathbb{R}^5_+$,*

$$\Omega = \{x \in \mathbb{R}^5_+ \mid x_1 + x_2 \leq k_{CD},\ x_3 \leq \frac{q + \beta\psi k_{CD}}{\omega},\ x_4 \leq 1,\ x_5 \leq \frac{q + \beta\psi k_{CD}}{\omega}\}.$$

Then, Ω is a positively invariant set under system (2.5).

Proof. It should be clear that the state solutions are bounded from below by zero such that $x(t) \in \mathbb{R}^5_+$ for all $t \geq 0$, *i.e.,* the densities of bacteria, phage and immune cells cannot be negative. The following discussion assumes that the initial condition is in the set Ω, *i.e.,* $x(0) \in \Omega$. Note that

$$\dot{x}_1 + \dot{x}_2 \leq rx_1\left(1 - \frac{x_1 + x_2}{k_{CD}}\right) + r'x_2\left(1 - \frac{x_1 + x_2}{k_{CD}}\right) = (rx_1 + r'x_2)\left(1 - \frac{x_1 + x_2}{k_{CD}}\right),$$

which implies that $x_1(t) + x_2(t) \leq k_{CD}$ for $t \geq 0$. Similarly, we must have $x_4(t) \leq 1$ for all $t \geq 0$. The control inputs $(u_1, u_2)^T \in U$ for all $t \geq 0$, hence, we have

$$\dot{x}_3 = \beta\psi x_1\left(\frac{x_3}{1 + x_3}\right) - \psi x_1 x_3 - \omega x_3 + qu_1 \leq (\beta\psi x_1 + q) - x_3(\psi x_1 + \omega).$$

Using the boundedness of x_1, *i.e.,* $0 \leq x_1 \leq k_{CD}$, we have

$$\dot{x}_3 \leq (\beta\psi k_{CD} + q) - x_3\omega.$$

Clearly, $x_3(t) \leq (q + \beta\psi k_{CD})/\omega$ for all $t \geq 0$. Similarly, using the boundedness of x_2, we have $x_5(t) \leq (q + \beta\psi k_{CD})/\omega$ for all $t \geq 0$. Altogether, we find that Ω is positively invariant under system (2.5) □

Existence of optimal control.

Remark 1. *Notably, the system (2.5) is control affine and the control set $\mathcal{U}$ is compact and convex, the integrand of the cost functional, $\mathcal{L}(x, u)$, is convex on U for each x, and the*

terminal cost function $g(x)$ is continuous. Thus, the sufficient conditions for the existence of optimal control are satisfied (see Theorem 4.1 in [74]). The similar exercises of proving the existence of optimal control based on Theorem 4.1 in [74] are referred to [25, 19, 75, 27].

2.3.2 The optimality system

Once the existence of optimal control has been established, we derive the optimality system by Pontryagin's Maximum Principle (PMP). Note that PMP gives the necessary conditions for the optimal control [70]. First, we formulate the optimal control problem as following

$$\min\{\mathcal{J}(u)|u \in \mathcal{U}\} \quad \text{subject to} \quad \dot{x} = f(t, x, u),\ x(0) = x_0, \tag{2.9}$$

where $\mathcal{J}(u)$ is the cost functional given in Eq. 2.6, $\mathcal{U}$ is the admissible control space, $f(t, x, u)$ is right hand side (RHS) of system (2.5) and x_0 is the initial condition. Applying PMP, we obtain the optimality conditions that must be met for an optimal control in problem (2.9).

Theorem 2.3.1. *If $u^*(t) = [u_1^*(t), u_2^*(t)]^T$ is an optimal control pair that solves problem (2.9), $x^*(t)$ is the corresponding state trajectory of the initial value system (2.5), and $\lambda^*(t)$ is the costate trajectory of the following terminal value system*

$$\dot{\lambda}^* = -\left(\frac{\partial f}{\partial x}(x^*)\right)^T \lambda^* - \left(\frac{\partial \mathcal{L}}{\partial x}(x^*, u^*)\right)^T, \quad \lambda^*(t_f) = [\theta_f, \theta_f, 0, 0, 0]^T \tag{2.10}$$

where $\frac{\partial f}{\partial x}$ is the Jacobian of state system (2.5) and $\frac{\partial \mathcal{L}}{\partial x} = [\theta_B, \theta_B, 0, 0, 0]$, then

$$u^*(t) = \mathcal{P}_U(\hat{u}(t)), \quad \hat{u}(t) = -\frac{q}{\theta_u}\begin{bmatrix}\lambda_3^*(t)\\ \lambda_5^*(t)\end{bmatrix}. \tag{2.11}$$

where $\mathcal{P}_U(\hat{u}(t))$ represents the projection of $\hat{u}(t)$ onto U in ℓ_2-norm. The detailed imple-

mentation of projection operator $\mathcal{P}_U$ is given in Appendix 2.6.1.

Proof. Given that $u^* = [u_1^*, u_2^*]^T$ is an optimal control pair that solves problem (2.9), and $x^*(t)$ and $\lambda^*(t)$ are the corresponding state trajectory and costate trajectory, then the following equations are satisfied by PMP:

$$\textit{State equation}: \ \dot{x}^* = f(x^*, u^*) \tag{2.12}$$

$$\textit{Costate equation}: \ \dot{\lambda}^* = -\left(\frac{\partial f}{\partial x}(x^*)\right)^T \lambda^* - \left(\frac{\partial \mathcal{L}}{\partial x}(x^*, u^*)\right)^T \tag{2.13}$$

$$\textit{Maximum principle}: \forall t \in [0, t_f], \ \mathcal{H}(x^*(t), \lambda^*(t), u^*(t)) = \min\left\{\mathcal{H}(x^*(t), \lambda^*(t), u) \mid u \in U\right\} \tag{2.14}$$

$$\textit{Terminal condition}: \ \lambda^*(t_f) = \left(\frac{\partial g}{\partial x}(x^*(t_f))\right)^T, \tag{2.15}$$

where $\mathcal{H}$ is the Hamiltonian with form of $\mathcal{H}(x, \lambda, u) = \lambda^T f(x, u) + \mathcal{L}(x, u)$. In our case, we have

$$\begin{aligned}
\mathcal{H}(x, \lambda, u) = {} & \lambda_1 \left[r x_1 \left(1 - \frac{x_1 + x_2}{k_{CD}}\right)(1 - \mu) - k_{PD} x_1 \mathcal{I}(x_3) - \frac{\widetilde{\epsilon} x_4 x_1}{1 + x_1 + x_2} \right] \\
& + \lambda_2 \left[r' x_2 \left(1 - \frac{x_1 + x_2}{k_{CD}}\right) + r x_1 \left(1 - \frac{x_1 + x_2}{k_{CD}}\right)\mu - k_{PD} x_2 \mathcal{I}(x_5) - \frac{\widetilde{\epsilon} x_4 x_2}{1 + x_1 + x_2} \right] \\
& + \lambda_3 \left[\beta x_1 \mathcal{I}(x_3) - \psi x_1 x_3 - \omega x_3 + q u_1\right] \\
& + \lambda_4 \left[\alpha x_4 (1 - x_4) \left(\frac{x_1 + x_2}{x_1 + x_2 + k_{ND}} \right) \right] \\
& + \lambda_5 \left[\beta x_2 \mathcal{I}(x_5) - \psi x_2 x_5 - \omega x_5 + q u_2\right] + \theta_B (x_1 + x_2) + \frac{\theta_u}{2} \|u\|_2^2 \\
= {} & \mathcal{Q} + q\lambda_3 u_1 + q\lambda_5 u_2 + \frac{\theta_u}{2} \|u\|_2^2,
\end{aligned}$$

where $\mathcal{Q}$ is the collection of terms that has no argument in u. The minimization of $\mathcal{H}$ over $u \in U$ is a linear constrained quadratic programming (QP) problem [76]. We write the

minimization problem in its equivalent form,

$$\min\left\{\mathcal{Q}+q\lambda_3u_1+q\lambda_5u_2+\frac{\theta_u}{2}\|u\|_2^2 \mid u\in U\right\} \quad \Leftrightarrow \quad \min_{u\in\mathbb{R}^2} b^Tu+u^TAu$$
$$\text{s.t} \quad \mathbb{1}^Tu\le 1,\ e_1^Tu\ge 0,\ e_2^Tu\ge 0$$

where $e_1=[1,0]^T$, $e_2=[0,1]^T$, $\mathbb{1}=[1,1]^T$, and

$$A=\frac{\theta_u}{2}\begin{bmatrix}1 & 0\\ 0 & 1\end{bmatrix},\ b=q\begin{bmatrix}\lambda_3\\ \lambda_5\end{bmatrix}.$$

Let u^* be minimizer of above constrained QP problem, we observe that u^* has following closed form

$$u^*=\mathcal{P}_U(\hat{u}),\quad \hat{u}=-\frac{q}{\theta_u}\begin{bmatrix}\lambda_3\\ \lambda_5\end{bmatrix}.$$

where $\mathcal{P}_U(\hat{u})$ represents the projection of $\hat{u}$ onto U. Next, we derive the system of costate in Eq. 2.13. Note that $\partial\mathcal{L}/\partial x=[\theta_B,\theta_B,0,0,0]$, the terminal condition of costate equation is $\lambda^*(t_f)=[\theta_f,\theta_f,0,0,0]^T$ by Eq. 2.15. The Jacobian of the RHS of state equation is

$$\frac{\partial f}{\partial x}=\begin{bmatrix}J_{11} & J_{12} & J_{13} & J_{14} & 0\\ J_{21} & J_{22} & 0 & J_{24} & J_{25}\\ J_{31} & 0 & J_{33} & 0 & 0\\ J_{41} & J_{42} & 0 & J_{44} & 0\\ 0 & J_{52} & 0 & 0 & J_{55}\end{bmatrix},$$

where

$$J_{11} = \frac{r(1-\mu)(k_{CD}-2x_1-x_2)}{k_{CD}} - k_{PD}\mathcal{I}(x_3) - \frac{\widetilde{\epsilon}(1+x_2)x_4}{(1+x_1+x_2)^2}\ ,$$
$$J_{12} = \frac{\widetilde{\epsilon}x_1x_4}{(1+x_1+x_2)^2} - \frac{r(1-\mu)x_1}{k_{CD}},$$
$$J_{13} = -k_{PD}\frac{\psi x_1}{(1+x_3)^2}\ ,\ J_{14} = -\frac{\widetilde{\epsilon}x_1}{1+x_1+x_2},$$
$$J_{21} = \frac{\mu r(k_{CD}-2x_1-x_2)}{k_{CD}} - \frac{r'x_2}{k_{CD}} + \frac{\widetilde{\epsilon}x_2x_4}{(1+x_1+x_2)^2},$$
$$J_{22} = \frac{r'(k_{CD}-x_1-2x_2)}{k_{CD}} - \frac{\mu r x_1}{k_{CD}} - k_{PD}\mathcal{I}(x_5) - \frac{\widetilde{\epsilon}(1+x_1)x_4}{(1+x_1+x_2)^2},$$
$$J_{24} = -\frac{\widetilde{\epsilon}x_2}{1+x_1+x_2}\ ,\ J_{25} = -k_{PD}\frac{\psi x_2}{(1+x_5)^2},$$
$$J_{31} = \beta\mathcal{I}(x_3) - \psi x_3\ ,\ J_{33} = \frac{\beta\psi x_1}{(1+x_3)^2} - \omega - \psi x_1,$$
$$J_{41} = \frac{\alpha k_{ND}x_4(1-x_4)}{(k_{ND}+x_1+x_2)^2}\ ,\ J_{42} = \frac{\alpha k_{ND}x_4(1-x_4)}{(k_{ND}+x_1+x_2)^2}\ ,\ J_{44} = \alpha(\frac{x_1+x_2}{x_1+x_2+k_{ND}})(1-2x_4),$$
$$J_{52} = \beta\mathcal{I}(x_5) - \psi x_5\ ,\ J_{55} = \frac{\beta\psi x_2}{(1+x_5)^2} - \omega - \psi x_2.$$

We have explained Eqs. 2.12 - 2.15. □

2.3.3 Analysis of optimal control in monophage therapy

The monophage therapy can be modeled by a reduced form of system (2.5). The state vector of population densities is $[S, R, P_S, I]^T$, the corresponding population dynamics is modeled analogously to system (2.1) by excluding any terms associated with phage P_R. Via the same scale transformations in Eq. 2.3 and Eq. 2.4, the scaled system of monophage

therapy model is

$$\begin{aligned}
\dot{x}_1 &= rx_1\left(1-\frac{x_1+x_2}{k_{CD}}\right)(1-\mu) - k_{PD}x_1\mathcal{I}(x_3) - \frac{\widetilde{\epsilon}x_4x_1}{1+x_1+x_2}\\
\dot{x}_2 &= r'x_2\left(1-\frac{x_1+x_2}{k_{CD}}\right) + rx_1\left(1-\frac{x_1+x_2}{k_{CD}}\right)\mu - \frac{\widetilde{\epsilon}x_4x_2}{1+x_1+x_2}\\
\dot{x}_3 &= \beta x_1\mathcal{I}(x_3) - \psi x_1x_3 - \omega x_3 + qu_1(t)\\
\dot{x}_4 &= \alpha x_4(1-x_4)\left(\frac{x_1+x_2}{x_1+x_2+k_{ND}}\right).
\end{aligned} \tag{2.16}$$

Note that the RHS of system (2.16) is the same as the RHS of system (2.5) by excluding all the terms associated with x_5. Here, the space of controls is denoted by $\mathcal{U}_1$, which is the set of Lebesgue-measurable functions $u_1 : [t_0, t_f] \longrightarrow U_1$, where $U_1 = [0, 1]$. The optimal control formulation is

$$\begin{aligned}
&\min\{\int_{t_0}^{t_f} \theta_B(x_1+x_2) + \frac{\theta_u}{2}u_1^2\, dt \;+\; \theta_f(x_1(t_f)+x_2(t_f)) \mid u_1 \in \mathcal{U}_1\}\\
&\text{subject to the system (2.16).}
\end{aligned} \tag{2.17}$$

The existence of optimal control is still guaranteed. The necessary conditions of optimal control in problem (2.17) are derived in appendix 2.6.2

2.4 Results

2.4.1 The Hamiltonian-based algorithm

We solve the optimal control problems by a Hamiltonian-based algorithm, this algorithm is presented with greater detail in [71, 72]. A salient feature is that the algorithm converges fast towards a near-optimal control (for a class of problems) if the Hamiltonian function is convex in u and can be minimized effectively and efficiently. Here, we briefly describe this algorithm. Two parameters are used to control the backtracking search, $\eta \in (0, 1)$ and $s \in (0, 1)$, and we used $\eta = s = 0.5$.

Algorithm $\star$ Fix a finite grid of equally-spaced points in the interval $[t_0, t_f]$, henceforth referred to as 'the grid'. At the k^{th} iteration of the algorithm, $k = 1, 2, \ldots$, it starts with the k^{th} control iteration u^k, and computes from it the next iteration, u^{k+1}, as follows.

1. Given a control input u^k, compute the state trajectory x forward using numerical integration.

2. Compute the costate trajectory λ backward in time.

3. For every t in the grid on the interval $[t_0, t_f]$, compute $v^*(t)$ that minimizes the Hamiltonian. Interpolate the results by a zero-order hold (piecewise-constant interpolation) to define the control $v^* := \{v^*(t) : t \in [t_0, t_f]\}$. It serves as the steepest-feasible descent direction from u^k.

4. Compute $\Theta(u^k) := \int_{t_0}^{t_f} \big(\mathcal{H}(x, v^*, \lambda) - \mathcal{H}(x, u^k, \lambda)\big) dt$.

5. Find $\ell(u^k) = \min\{\ell = 0, 1, 2, \ldots \mid \mathcal{J}(s^\ell v^* + (1 - s^\ell)u^k) - \mathcal{J}(u^k) \leq \eta s^\ell \Theta(u^k)\}$.

6. Set $u^{k+1} = (1 - s^{\ell(k)})u^k + s^{\ell(k)} v^*$.

The state trajectory $x(t)$ and the costate trajectory $\lambda(t)$ are numerically integrated by Euler's method [77], the time step is $\Delta t = 5 \times 10^{-4}$. The convergence indicator $|\Theta(u)|$ measures the extent to which u fails to satisfy the PMP. The algorithm will be terminated when either $|\Theta(u)| \leq 10^{-5}$ or the maximum number of allowed iterations is reached.

2.4.2 Preliminaries of simulations

The model parameters and initial conditions of system (2.1) are given in Table 3.1. The *in silico* experiments run for 3 days post infection and all the treatments start at 2 hours after initialization (consistent with *in vivo* treatments in [69]), we thus set $t_0 = 2$ hrs and $t_f = 72$ hrs. In addition, the optimal dose and timing of therapy are not sensitive to the final treatment time t_f, see appendix 2.6.4. We fix the regulator weights $\theta_B = \theta_f = 1$. We

will tune the value of θ_u to solve a practical variant of the original control problems (2.9) and (2.17).

Practical treatment objective. The goal of the optimal control framework described in Sect. 2.2.2 is to minimize the total bacterial population and penalizing the treatment costs by optimizing the scaled phage injection rates. However, from a practical therapeutic perspective, we may want to find the minimal phage dosage required to eliminate bacteria instead. Since the differential equation system (2.1) is continuous, we assume the bacterial population is eliminated if there exists a time $\tau \in [0, t_f]$ such that $S(\tau) + R(\tau) \leq n_{\text{ext}}$, where $n_{\text{ext}} = 1$ CFU/g is the hard threshold of bacteria elimination.

The objective of practical therapy can thus be formalized as a constrained optimal control problem that minimizes the integral of phage injection rates subject to the constraint of bacteria elimination in a *hybrid system* where the state equations are different before and after bacterial elimination. The discontinuous nature of bacterial elimination events poses considerable numerical challenge in explicitly solving the constrained hybrid optimal control problem. As a result, we utilize the ordinary control formulations (2.9) and (2.17) to achieve the goal of eliminating bacteria with minimum dosage via a heuristic approach. In this approach, we adjust the regulator weight θ_u and locate the highest value that results in bacterial elimination. The total phage dosage is then computed to find the minimum dosage corresponding to bacterial elimination.

Minimal phage dosage and regulator weight θ_u. Here, we detail the procedure of achieving the practical control objective by tuning regulator weight θ_u in a certain range. We search θ_u in the interval $[10^{-11}, 10^{11}]$, ranging from negligible treatment costs ($\theta_u = 10^{-11}$) to dominating treatment costs ($\theta_u = 10^{11}$) in the control objective. For any fixed $\theta_u \in [10^{-11}, 10^{11}]$, we can numerically solve the optimal control problems (2.9) and (2.17) via a Hamiltonian-based algorithm. It is also easy to check if the optimal control solution effectively eliminates bacterial populations based on the artificial threshold we introduced.

In order to find the treatment (*i.e.,* profiles of phage injection rate) that can eliminate bacteria with minimal dosage, we sweep over the range of θ_u and extract all the 'θ_u' values that lead to successful bacterial elimination. Assuming such 'θ_u' values exist, we then find the minimum effective phage dosage by computing the integral of phage injection rate that corresponds to the highest 'θ_u' value resulting in bacterial elimination, e.g., dosage of a treatment that has two types of phage is $\mathcal{D} = \int_{t_0}^{t_f} \rho_S(t) + \rho_R(t)\ dt$. In the case that no optimal control treatment can eliminate the bacteria with θ_u in the range of $[10^{-11}, 10^{11}]$, we assume phage therapy would fail under all reasonable phage dosages in such conditions.

However, the computational costs of finding the value of θ_u corresponding to the minimum effective dosage (θ_u^*) via brute-force searching are very high. Intuitively, we note that if bacteria is eliminated for a given $\theta_u' \in [10^{-11}, 10^{11}]$, then bacteria would also be eliminated for all $\theta_u \leq \theta_u'$, i.e., relaxing penalization on treatment costs would always eliminate bacteria. Likewise, if bacteria is not eliminated for θ_u', then bacteria is also not eliminated for all $\theta_u \geq \theta_u'$ as higher penalization on treatment costs would lead to a less effective treatment.

Building upon these intuitions, we implement a binary search algorithm to find θ_u^*. We first evaluate the two boundary cases ($\theta_u = 10^{-11}$ and $\theta_u = 10^{11}$) and assume that phage therapy would fail in general if the optimal treatment corresponding to $\theta_u = 10^{-11}$ fails. In addition, if the optimal treatment corresponding to $\theta_u = 10^{11}$ can successfully eliminate bacteria, its associated phage dosage is identified as the minimum effective dosage. If both of the aforementioned boundary conditions are not satisfied, we compute the optimal treatment corresponding to an intermediate weight $\theta_{ui} = 10^{(L+R)/2}$ where $L = -11$ and $R = 11$ for the two boundaries. If optimal treatment with θ_{ui} works, we update left searching boundary $L \leftarrow (L + R)/2$; otherwise, we update right searching boundary $R \leftarrow (L + R)/2$. We iterate this procedure for $n = 8$ times (corresponding to a precision of about $22/2^8 \approx 0.08$ at power scale, where 22 is the length of power scale range for $\theta_u \in [10^{-11}, 10^{11}]$) to estimate the value of θ_u^*.

Classification of injection strategies. In this study, we focus on three types of injection strategies: an optimal control strategy in monophage therapy, namely, one dimensional optimal control (*1D-OC*); an optimal control strategy using multiple types of phage, namely, two dimensional optimal control (*2D-OC*); and a *practical therapeutic treatment* using either single or multiple types of phage. The 1D-OC and 2D-OC are optimal controls solved numerically from problems (2.17) and (2.9) respectively. However, 1D-OC and 2D-OC are usually continuous signals, which cannot be directly implemented in (current) clinical treatment, we thus have to convert the continuous treatment to a (discrete) multi-dose treatment.

In this chapter, we only focus on developing multi-dose treatment guided by 2D-OC treatment in immunodeficient scenarios. There are two types of phage in 2D-OC and we allow one-time dose injection for each type of phage in the practical therapeutic treatment. The timings of injecting phage P_S and phage P_R (in practical therapeutic treatment guided by 2D-OC) are denoted by T_{P_S} and T_{P_R} respectively. We define $T_{P_S} = min\{\tau \in [t_0, t_f] \mid \rho_S(\tau) \geq \rho_S(t)\ \forall t \in [t_0, t_f]\}$, *i.e.,* the first time that injection rate of phage P_S arrives its maximal rate. T_{P_R} is defined in the same way as T_{P_S}. We define the integral of phage injection rate $\rho_S(t)$ over $[t_0, t_f]$ as $\mathcal{D}_S$, and the analogous integral of the second phage type as $\mathcal{D}_R$. In doing so, given a 2D-OC treatment $(\rho_S(t), \rho_R(t))$, the practical therapeutic treatment guided by this 2D-OC treatment is: injecting $\mathcal{D}_S$ amount of phage P_S at time T_{P_S} and injecting $\mathcal{D}_R$ amount of phage P_R at time T_{P_R}. The *in silico* experiments using practical therapeutic treatment assumes bacteria and phage are eliminated locally when their population densities drop below a threshold of 1 g^{-1}. As the practical therapeutic treatment guided by 2D-OC is only an approximation of the optimal treatment, it is possible for the practical strategy to fail to eliminate bacteria. In this situation, we iteratively amplify the dosages (ten percent higher for each step) of the two phage types used in practical therapeutic treatment while fixing the timings of phage injection until bacterial populations are eliminated.

2.4.3 Monophage therapy in immunocompetent hosts

For immunocompetent hosts with intact immune activation, monophage therapy can be highly effective in curing bacterial infections [69]. However, phage therapy can still fail when the phage decay rate is high, or when the phage infection rate is low due to inefficient phage strains or partial resistance [68, 69]. To explore these potential modes of failure, we set the phage infection rate to be $\phi = 3.38 \times 10^{-8}$ g/(h PFU), slightly lower than the estimated value $\phi = 5.4 \times 10^{-8}$ g/(h PFU) in [69]. We then plot the performances of 1D-OC strategy by their minimal phage dosages for eliminating the bacterial population given a range of phage decay rate $\omega \in [10^{-2}, 10^{2}](h^{-1})$.

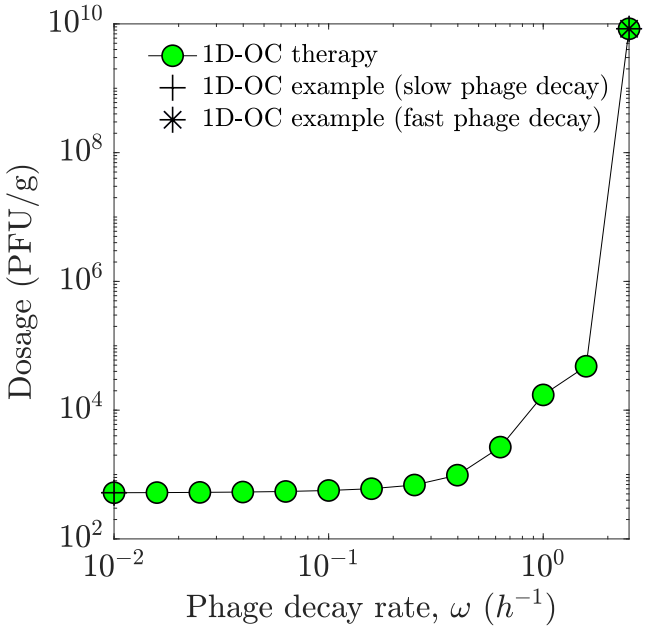

Figure 2.2: Minimal phage amount for eliminating bacterial cells using 1D-OC strategy (green dots). There is no 1D-OC treatment that can eliminate bacteria in the regime of high phage decay rate ($\omega \geq 2.5h^{-1}$). Two 1D-OC examples are provided in Fig. 2.3: the corresponding time series of population densities and injection rate trajectories. See model parameters and simulation details in Sect. 2.4.2.

In Fig. 2.2, we find that the minimum phage dosage needed by 1D-OC strategies to eliminate the bacteria increases monotonically with the phage decay rate. In addition, the

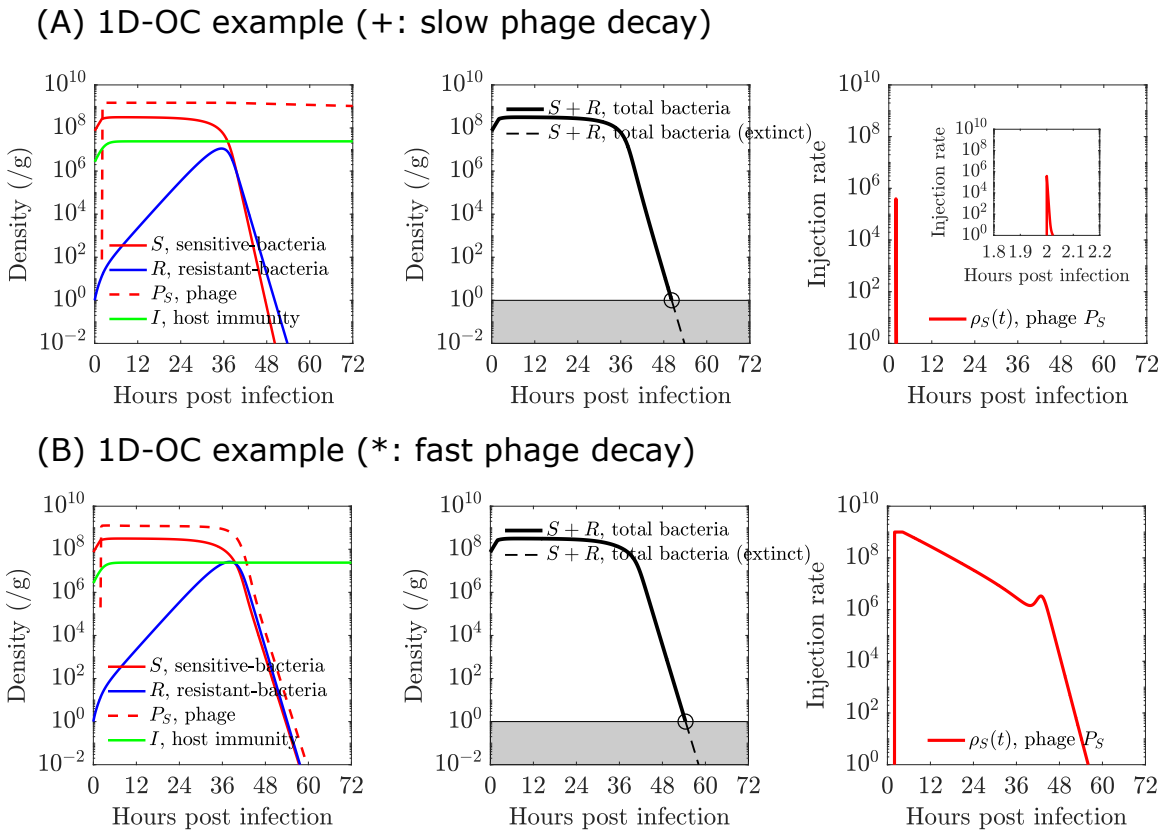

Figure 2.3: Time series of population densities and optimal injection rates of two 1D-OC examples (labeled in Fig. 2.2): slow phage decay ($\omega = 0.01h^{-1}$) and fast phage decay ($\omega = 2.5h^{-1}$). (A) Optimal injection rate, $\rho_S(t)$, is obtained by solving control problem (2.17) with tuned regulator weight $\theta_u = 10^{11}$. The Hamiltonian-based algorithm is terminated after k iterations and output control u_1^k, where $k = 11$. The numerical value of objective cost in problem (2.17) with control u_1^k is 228.47, and the convergence indicator $|\Theta(u_1^k)| \approx 2.11 \times 10^{-6}$. Bacteria is eliminated around 50 hrs post infection. (B) Optimal injection rate, $\rho_S(t)$, is obtained by solving control problem (2.17) with tuned regulator weight $\theta_u = 10$. The Hamiltonian-based algorithm is terminated after k iterations and output control u_1^k, where $k = 9$. The numerical value of objective cost in problem (2.17) with control u_1^k is 264.73, and the convergence indicator $|\Theta(u_1^k)| \approx 5.20 \times 10^{-6}$. Bacteria is eliminated around 50 hrs post infection. See model parameters and simulation details in Sect. 2.3.3.

dosage increase becomes extremely rapid at decay rate $\omega \sim 1$ h^{-1} and 1D-OC therapy fails for all practical dosages when $\omega > 2.5$ h^{-1}. The time series of population dynamics at slow phage decay rate are plotted in Fig. 2.3A. The single-impulse like optimal injection rate shows that the 1D-OC treatment (in this case) is approximately a single-dose treatment: injecting a small amount of phage (about 5×10^2 PFU) at the very beginning of treatment

2 hours post infection. In doing so, the optimized treatment reduces the phage-sensitive bacterial population quickly and controls the emergence of resistant bacteria in an early stage. On the other hand, when phage decay at a fast rate, the 1D-OC strategy maintains the phage concentration and treatment efficacy by continuously injecting phage into the system over a longer period of time (see Fig. 2.3B).

2.4.4 Phage therapy in immunodeficient hosts

Previous work has shown that a deficient immune response may lead to failure of phage therapy in an acute pneumonia system [69]. Here, we explore whether phage combination therapy (phage cocktails) that includes a host-range mutant phage targeting resistant bacteria can restore therapeutic effectiveness in immunodeficient hosts, and identify optimal ways to achieve that. In the immunodeficient model, immune signaling is assumed to be absent such that the immune response intensity is maintained at a basal level, $I = I_0$. In addition, the initial bacterial inoculum is lowered by two orders of magnitude in the immunodeficient model compared to the immunocompetent case [69]. We further assume that the wild-type and host-range mutant phage target the phage-sensitive and phage-resistant bacteria respectively with no cross infectivity. First, we compute 2D-OC treatments corresponding to minimal phage dosages given a range of basal-level immune density. Then, we test a practical approximation of the 2D-OC treatment by converting the 2D-OC phage injection profile into discrete doses of each phage strain (see Sect. 2.4.2 for details). For each basal-level immune density, we evaluate the performance of the practical therapeutic treatment guided by the 2D-OC treatment at the same basal-level immune density.

The numerical results show that the minimal phage amount of both 2D-OC and practical therapies for eliminating bacterial cells decreases with increasing basal-level immune density (see Fig. 2.4A). Moreover, for practical therapeutic treatments in the entire range of the basal-level immune density, the optimal timings of injecting the two types of phage are both at the very beginning of treatment (*i.e.,* $T_{P_S} = T_{P_R} \approx 2$ hrs). Furthermore, given our

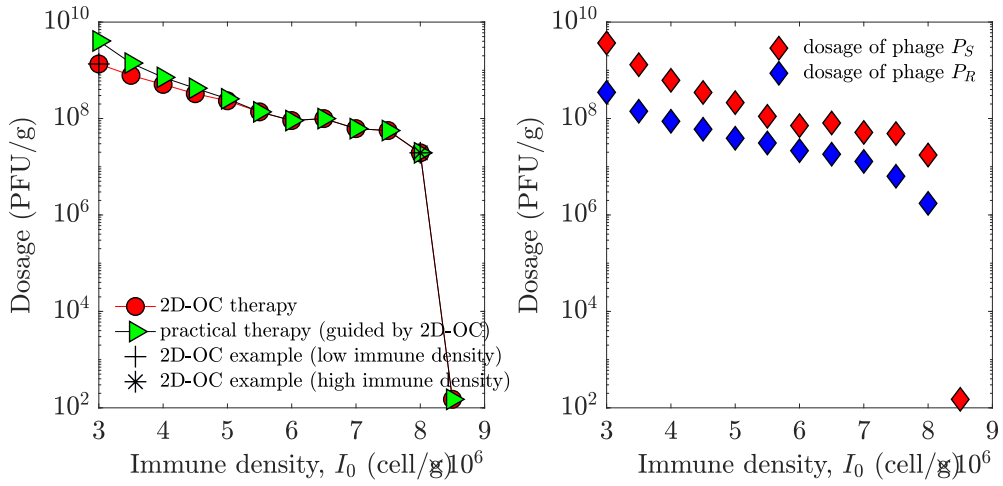

Figure 2.4: Minimal phage amount for eliminating bacterial cells using 2D-OC strategy (left) and the practical therapeutic treatment (right). (Left) Minimal phage amount for eliminating bacterial cells using 2D-OC strategy (red) and practical therapeutic treatment guided by 2D-OC strategy (green). Two *in silico* experiments (high immune density $I_0 = 8 \times 10^6$ cell/g and low immune density $I_0 = 3 \times 10^6$ cell/g) are provided in Figs. 2.5 and 2.6 respectively. (Right) Dosage of phage P_S (red) and dosage of phage P_R (blue) used in practical therapeutic treatment. The timings of injecting two types of phage dose are both about two hours post infection (*i.e.,* $T_{P_S} = T_{P_R} \approx 2$ hrs). Note that the total dosage of two types of phage (add up of P_S phage dosage and P_R phage dosage) is the green curve in the left panel. See model parameters and simulation details in Sect. 2.4.2.

model and parameter assumptions the optimal control algorithm always result in a dosage of phage P_S about ten times higher than the dosage of phage P_R (*i.e.,* $\mathcal{D}_S/\mathcal{D}_R \approx 10$), see Fig. 2.4B. When the basal-level immune density is very high, $I_0 \approx 8.5 \times 10^6$ (cell/g), the practical treatment only needs a small amount of phage P_S (about 10^2 PFU) to eliminate bacteria (see Fig. 2.4B and Fig. 2.7 in appendix 2.6.3). To investigate the phage delivery schedules identified by the optimal control strategies and understand the advantages of phage combination therapy, we compare the injection rate and population dynamics of 1D-OC, 2D-OC and practical therapeutic strategies in Figs. 2.5 and 2.6.

For the 1D-OC case at high level of immune response (see Fig. 2.5A), the optimal phage dosing occurs over a time period of nearly 60 hours with injection rate starting at around the maximal value of 10^9 PFU/(h g) and decreasing after 24 hours. The immunodeficiency

necessitated a much higher dosage of phage sustained over a long period of time even for a low initial bacterial inoculum. The aggressive phage dosing results in a roughly exponential decrease in phage-sensitive bacteria, but the phage-resistant bacteria is not effectively controlled and increases slightly in population. Phage-resistant bacteria is even more problematic at low baseline immune level (see Fig. 2.6A), where the resistant mutants grow exponentially until they reach the carrying capacity despite a more aggressive phage dosing that maintains a maximum injection rate until 48 hours post infection. The failure of phage therapy in these cases is a result of the deficient immune response not being able to control phage-resistant bacteria, as confirmed by the population dynamics at sufficiently high baseline immune response (see Fig. 2.7 in appendix 2.6.3) which shows effective control of both phage-sensitive and phage-resistant bacterial populations at much lower phage dose.

Figs. 2.5B-C and 2.6B-C show how judicious use of a phage cocktail in the 2D-OC strategy can improve the robustness of therapeutic success. In Fig. 2.5B, the host-range mutant phage is injected for the entire dosing schedule to preemptively inhibit the phage-resistant bacteria. Initially, wild-type phage targeting the phage-sensitive bacteria is injected at a higher dose than the host-range mutant phage as the initial inoculum consists mostly of sensitive bacteria. That balance is shifted as the relative proportion of resistant bacteria increases and the host-range mutant phage becomes the major component of the cocktail at around 12 hrs post infection. Thus, the optimal injection rates (in 2D-OC treatment) exhibit interesting and complex temporal patterns. However, in real clinical treatments, it is not (yet) feasible to implement such a complicated phage delivery schedules. In Fig. 2.5C, the practical therapeutic treatment, i.e., a discretized form of the continuous 2D-OC treatment, also shows efficacy in eliminating the bacteria. In the case of low baseline immune response, the temporal patterns in treatment strategies (2D-OC and practical treatments) are similar to the case of high baseline immune response (see Figs. 2.6B-C and compare to Figs. 2.5B-C), but the dosage of two types of phage used in treatments

are much higher. This is consistent with our previous work showing that the host immune status may be a critical factor determining phage therapy efficacy [69]. In addition, for low immune level the time of switching over to a strategy dominated by the counter-resistant phage is delayed to about 36 hours after infection as opposed to around 12 hours in the high immune baseline case.

2.5 Discussion

In this chapter, we developed a control-theoretic framework to optimize the use of monophage treatment and phage cocktails for treating bacterial infections in immunodeficient hosts or in other scenarios such as high phage decay rate where standard phage therapy is likely to fail. By incorporating phage administration as the control in a mathematical model describing the nonlinear interactions between phage, pathogenic bacteria and host immunity, we derive a Hamiltonian-based algorithm to numerically minimize bacterial burden while limiting the phage dose. Our results indicate that optimal control may provide important insights to guide clinical use of phage therapy. In particular, a single dose of phage may be sufficient to treat immunocompetent patients when the phage clearance rate is low, whereas phage administration may need to be sustained over a longer period when phage clearance is fast. In immunodeficient hosts, our results suggest that the success of optimal administration of phage cocktails can largely be reproduced in a simplified, discretized version of the optimal therapy that would be easier to implement practically. The only trade-off observed for the simplified practical therapy is a slight increase of the minimum effective dose in cases of severe immunodeficiency. Our optimal control framework indicates that a single phage strain may be effective for therapy at relatively high immunity levels, but the use of multiple therapeutic phage is required for low immune intensities.

To ensure that the optimal control problem remains mathematically tractable, a number of simplifying assumptions have been made. For example, within-host dynamics is assumed to be deterministic, whereas biological processes such as mutations are inherently

stochastic. The gap between mathematical models and complex clinical trials can be even wider due to various confounding factors. In addition, the optimal control solutions are solved based on specific objective functional and model parameters. Hence, different sets of parameters, models, and the objective costs could yield different suggested treatments such that the robustness of our optimal treatments may not be guaranteed. Our model also focuses on acute infections, and did not consider spatial heterogeneity or cocktails consisting of more than two phage strains. These issues could be addressed in future work by extending our modeling framework to incorporate stochastic control [78, 74] in spatial models with multiple strains of phage. In doing so, it will be important to consider host adaptive immunity, which is important in chronic infections and can generate specific responses against phage [79, 80]. Finally, we note that host-range phage mutants may be able to infect multiple strain types [81]; hence future work should also address how to optimally combine phage with overlapping host ranges.

2.6 Appendix

2.6.1 Implementation of projection operator $\mathcal{P}_U$

Here we present a closed form of projection operator $\mathcal{P}_U$ via a geometric approach [76], recall that $u^* = \mathcal{P}_U(\hat{u})$ in Theorem 2.3.1, then we have following:

$$
\begin{aligned}
&u^* = \hat{u}, \text{ if } \hat{u} \in \{u \mid e_1^T u \geq 0,\ e_2^T u \geq 0,\ \mathbb{1}^T u - 1 \leq 0\},\\
&u^* = \mathcal{P}_{\mathcal{A}}(\hat{u}), \text{ if } \hat{u} \in \{u \mid \mathbb{1}^T u - 1 \geq 0,\ \widetilde{\mathbb{1}}^T u + 1 \geq 0,\ \widetilde{\mathbb{1}}^T u - 1 \leq 0\},\\
&u^* = [0,1]^T, \text{ if } \hat{u} \in \{u \mid e_2^T u - 1 \geq 0,\ \widetilde{\mathbb{1}}^T u - 1 \geq 0\},\\
&u^* = [0,\hat{u}_2]^T, \text{ if } \hat{u} \in \{u \mid e_1^T u \leq 0,\ e_2^T u \geq 0,\ e_2^T u - 1 \leq 0\},\\
&u^* = [0,0]^T, \text{ if } \hat{u} \in \{u \mid e_1^T u \leq 0,\ e_2^T u \leq 0\},\\
&u^* = [\hat{u}_1,0]^T, \text{ if } \hat{u} \in \{u \mid e_1^T u \geq 0,\ e_1^T u - 1 \leq 0,\ e_2^T u \leq 0\},\\
&u^* = [1,0]^T, \text{ if } \hat{u} \in \{u \mid \widetilde{\mathbb{1}}^T u + 1 \leq 0,\ e_1^T u \geq 1\},
\end{aligned}
$$

where $\widetilde{\mathbb{1}} = [-1, 1]^T$ and $\mathcal{A} = \{u \mid \mathbb{1}^T u - 1 = 0\}$. Computing the projection of $\hat{u}$ on to $\mathcal{A}$ is straightforward. The orthogonality principle yields $\hat{u} - \mathcal{P}_{\mathcal{A}}(\hat{u})$ must be colinear with $\mathbb{1}$, also $\mathcal{P}_{\mathcal{A}}(\hat{u}) \in \mathcal{A}$, *i.e.,* $\hat{u} - \mathcal{P}_{\mathcal{A}}(\hat{u}) = z\mathbb{1}$ and $\mathbb{1}^T \mathcal{P}_{\mathcal{A}}(\hat{u}) - 1 = 0$. This yields $z = (\mathbb{1}^T \hat{u} - 1)/(\mathbb{1}^T \mathbb{1})$ and thus $\mathcal{P}_{\mathcal{A}}(\hat{u}) = \hat{u} - z\mathbb{1}$.

2.6.2 The optimality system of optimal control in monophage therapy

Here, we derive the necessary conditions for the optimal control problem (2.17) via Pontryagin's Maximum Principle (PMP) [70].

Theorem 2.6.1. *If u_1^* is an optimal control that solves problem (2.17), and $x^*(t)$ is the corresponding state trajectory of the initial value problem (2.16), and $\lambda^*(t)$ is the costate trajectory of the following terminal value problem*

$$\dot{\lambda}^* = -\left(\frac{\partial f}{\partial x}(x^*)\right)^T \lambda^* - \left(\frac{\partial \mathcal{L}}{\partial x}(x^*, u^*)\right)^T, \quad \lambda^*(t_f) = [\theta_f, \theta_f, 0, 0]^T \tag{2.18}$$

where $\frac{\partial f}{\partial x}$ is the Jacobian of state equations (2.16) and $\frac{\partial \mathcal{L}}{\partial x} = [\theta_B, \theta_B, 0, 0]$, then

$$u_1^*(t) = \begin{cases} 0, & \text{if} \quad \lambda_3^*(t) \geq 0 \\ -\frac{q\lambda_3^*(t)}{\theta_u}, & \text{if} \quad -\frac{\theta_u}{q} \leq \lambda_3^*(t) < 0 \\ 1, & \text{if} \quad \lambda_3^*(t) < -\frac{\theta_u}{q}. \end{cases} \tag{2.19}$$

Proof. According to PMP, if u_1^* is an optimal control that solves problem (2.17), and if $x^*(t)$ and $\lambda^*(t)$ are the corresponding state trajectory and costate trajectory, then the fol-

lowing equations are satisfied,

$$\textit{State equation}: \ \dot{x}^* = f(x^*, u_1^*) \tag{2.20}$$

$$\textit{Costate equation}: \ \dot{\lambda}^* = -\left(\frac{\partial f}{\partial x}(x^*)\right)^T \lambda^* - \left(\frac{\partial \mathcal{L}}{\partial x}(x^*, u_1^*)\right)^T \tag{2.21}$$

$$\textit{Maximum principle}: \forall t \in [0, t_f], \ \mathcal{H}(x^*(t), \lambda^*(t), u_1^*(t)) = \min\{\mathcal{H}(x^*(t), \lambda^*(t), u_1) \mid u_1 \in U_1\} \tag{2.22}$$

$$\textit{Terminal condition}: \ \lambda^*(t_f) = \left(\frac{\partial g(x^*(t_f))}{\partial x}\right)^T, \tag{2.23}$$

where $\mathcal{H}$ is the Hamiltonian with form of $\mathcal{H}(x, \lambda, u_1) = \lambda^T f(x, u_1) + \mathcal{L}(x, u_1)$. We find that $\mathcal{H}(x, \lambda, u_1) = \widetilde{Q} + q\lambda_3 u_1 + (\theta_u/2)u_1^2$, where $\widetilde{Q}$ is the collection of terms that has no argument in u_1. Minimizing $\mathcal{H}(x, \lambda, u_1)$ over $u_1 \in U_1$ yields Eq. 2.19. The costate equation with terminal condition is

$$\dot{\lambda}^* = -\left(\frac{\partial f}{\partial x}(x^*)\right)^T \lambda^* - \left(\frac{\partial \mathcal{L}}{\partial x}(x^*, u_1^*)\right)^T, \ \lambda^*(t_f) = \left(\frac{\partial g(x^*(t_f))}{\partial x}\right)^T,$$

where $\partial\mathcal{L}/\partial x = [\theta_B, \theta_B, 0, 0]$, $\lambda^*(t_f) = [\theta_f, \theta_f, 0, 0]^T$. The Jacobian is

$$\frac{\partial f}{\partial x} = \begin{bmatrix} J_{11} & J_{12} & J_{13} & J_{14} \\ J_{21} & J_{22} & 0 & J_{24} \\ J_{31} & 0 & J_{33} & 0 \\ J_{41} & J_{42} & 0 & J_{44} \end{bmatrix},$$

where

$$J_{11} = \frac{r(1-\mu)(k_{CD}-2x_1-x_2)}{k_{CD}} - k_{PD}\mathcal{I}(x_3) - \frac{\widetilde{\epsilon}(1+x_2)x_4}{(1+x_1+x_2)^2}$$
$$J_{12} = \frac{\widetilde{\epsilon}x_1x_4}{(1+x_1+x_2)^2} - \frac{r(1-\mu)x_1}{k_{CD}}$$
$$J_{13} = -k_{PD}\frac{\psi x_1}{(1+x_3)^2}\ ,\ J_{14} = -\frac{\widetilde{\epsilon}x_1}{1+x_1+x_2}$$
$$J_{21} = \frac{\mu r(k_{CD}-2x_1-x_2)}{k_{CD}} - \frac{r'x_2}{k_{CD}} + \frac{\widetilde{\epsilon}x_2x_4}{(1+x_1+x_2)^2},$$
$$J_{22} = \frac{r'(k_{CD}-x_1-2x_2)}{k_{CD}} - \frac{\mu r x_1}{k_{CD}} - \frac{\widetilde{\epsilon}(1+x_1)x_4}{(1+x_1+x_2)^2}$$
$$J_{24} = -\frac{\widetilde{\epsilon}x_2}{1+x_1+x_2}\ ,\ J_{25} = -k_{PD}\frac{\psi x_2}{(1+x_5)^2}$$
$$J_{31} = \beta\mathcal{I}(x_3) - \psi x_3\ ,\ J_{33} = \frac{\beta\psi x_1}{(1+x_3)^2} - \omega - \psi x_1$$
$$J_{41} = \frac{\alpha k_{ND}x_4(1-x_4)}{(k_{ND}+x_1+x_2)^2}\ ,\ J_{42} = \frac{\alpha k_{ND}x_4(1-x_4)}{(k_{ND}+x_1+x_2)^2}\ ,\ J_{44} = \alpha(\frac{x_1+x_2}{x_1+x_2+k_{ND}})(1-2x_4).$$

We have explained Eqs. 2.20 - 2.23. □

2.6.3 Effective single-dose treatment in immunodeficient hosts

When the baseline immune response is sufficiently high in immunodeficient hosts, all the treatment strategies (1D-OC, 2D-OC and practical treatments) can eliminate bacteria with a low dose of phage P_S injected at very beginning of treatment (see Fig. 2.7 in Appendix 2.6.3).

2.6.4 Robustness analysis of optimal timing and dose to variations in therapy duration

From our numerical simulations, e.g. Figs 2.3, 2.5, 2.6 and 2.7, we observe that successful phage therapy relies on early injection (for both single-dose and multi-dose cases). Here, we show that early 'hit-hard' approaches remain robust to variations in treatment duration when the final treatment time t_f is changed. Please refer to Fig. 2.8 for the optimal dose and timing of the practical therapy for different final treatment time.

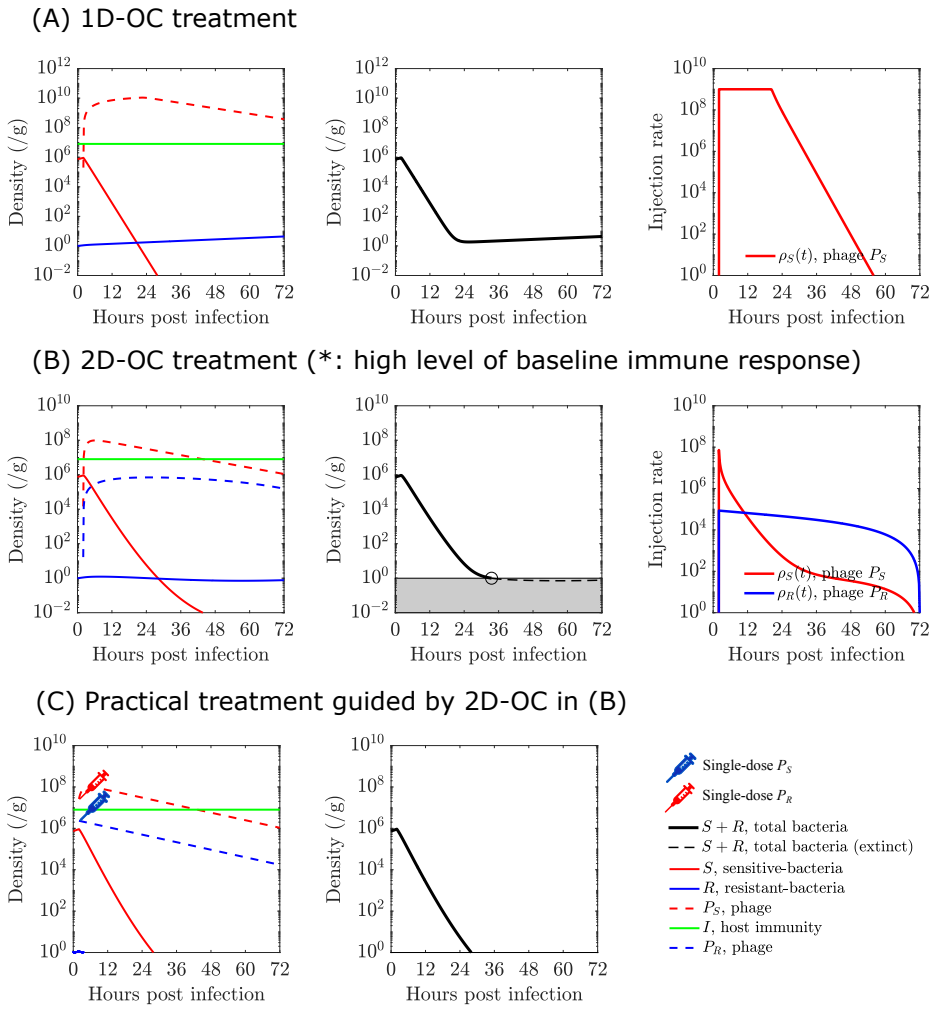

Figure 2.5: Comparison of time series of population densities with different treatments in the high level of baseline immune response, $I_0 = 8 \times 10^6$ cell/g. (A) Optimal injection rate, $\rho_S(t)$, is obtained by solving control problem (2.17) with tuned regulator weight $\theta_u = 10^{-11}$ (the smallest regulator weight on treatment costs). The Hamiltonian-based algorithm is terminated after k iterations and output control u_1^k, where $k = 2$. The numerical value of objective cost in problem (2.17) with control u_1^k is 0.03311, and the convergence indicator $|\Theta(u_1^k)| \approx 4.08 \times 10^{-12}$. There does not exist curative 1D-OC treatment due to the outgrowth of phage-resistant bacteria R. (B) Optimal injection rate, $\rho_S(t)$ and $\rho_R(t)$, is obtained by solving control problem (2.9) with tuned regulator weight $\theta_u = 10$. The Hamiltonian-based algorithm is terminated after k iterations and output control u^k, where $k = 5$. The numerical value of objective cost in problem (2.9) with control u^k is 0.048675, and the convergence indicator $|\Theta(u^k)| \approx 3.55 \times 10^{-6}$. Bacteria is eliminated around 30 hrs post infection. (C) The practical therapeutic treatment is obtained from optimal injection rate in (B): two doses, P_S phage dose and P_R phage dose, both are injected at two hours post infection with amount of 2.6×10^7 PFU and 2.3×10^6 PFU respectively. Bacteria is eliminated around 30 hrs post infection. See model parameters and simulation details in Sect. 2.4.2.

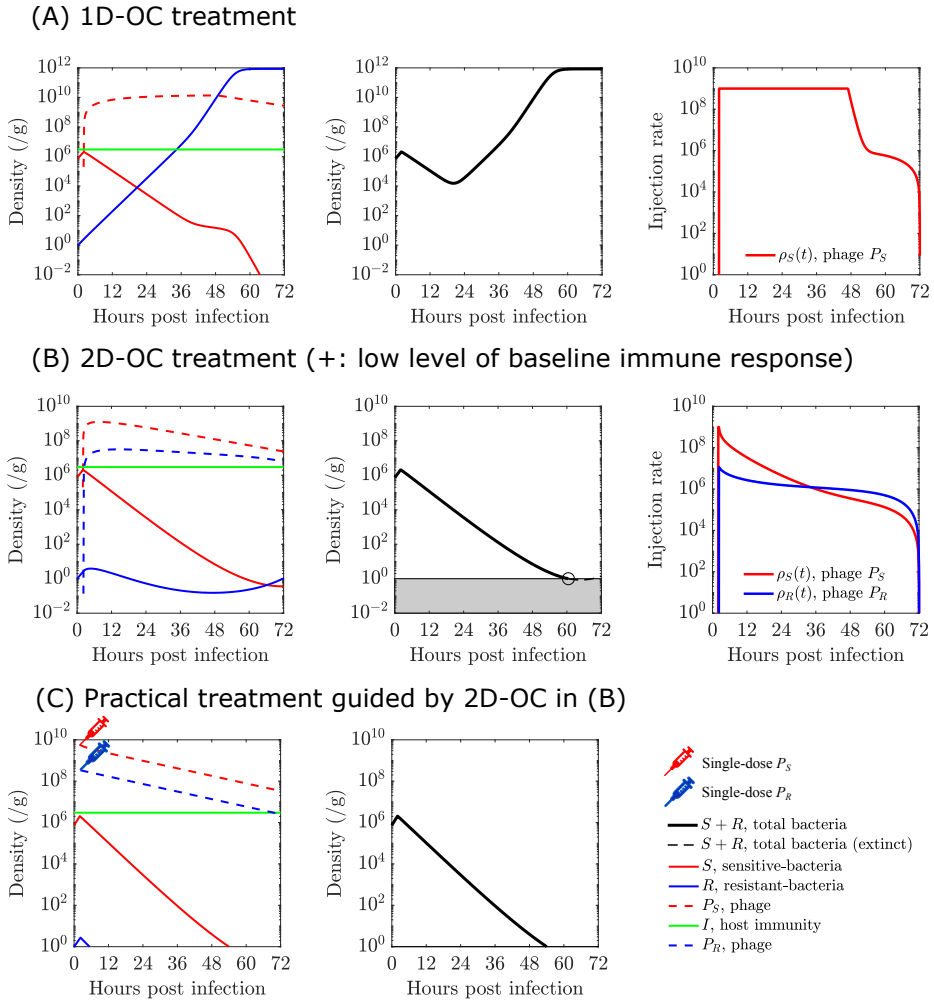

Figure 2.6: Comparison of time series of population densities with different treatments in the low level of baseline immune response, $I_0 = 3 \times 10^6$ cell/g. (A) Optimal injection rate, $\rho_S(t)$, is obtained by solving control problem (2.17) with tuned regulator weight $\theta_u = 10^{-11}$ (the smallest regulator weight on treatment costs). The Hamiltonian-based algorithm is terminated after k iterations and output control u_1^k, where $k = 2$. The numerical value of objective cost in problem (2.17) with control u_1^k is 3.75×10^5, and the convergence indicator $|\Theta(u_1^k)| \approx 1.15 \times 10^{-12}$. There does not exist curative 1D-OC treatment due to the outgrowth of phage-resistant bacteria R. (B) Optimal injection rate, $\rho_S(t)$ and $\rho_R(t)$, is obtained by solving control problem (2.9) with tuned regulator weight $\theta_u = 10^{-2}$. The Hamiltonian-based algorithm is terminated after k iterations and output control u^k, where $k = 12$. The numerical value of objective cost in problem (2.9) with control u^k is 0.184, and the convergence indicator $|\Theta(u^k)| \approx 1.13 \times 10^{-6}$. Bacteria is eliminated around 60 hrs post infection. (C) The practical therapeutic treatment is obtained from optimal injection rate in (B): two doses, P_S phage dose and P_R phage dose, both are injected at two hours post infection with amount of 3×10^9 PFU and 3×10^8 PFU respectively. Bacteria is eliminated around 60 hrs post infection. See model parameters and simulation details in Sect. 2.4.2.

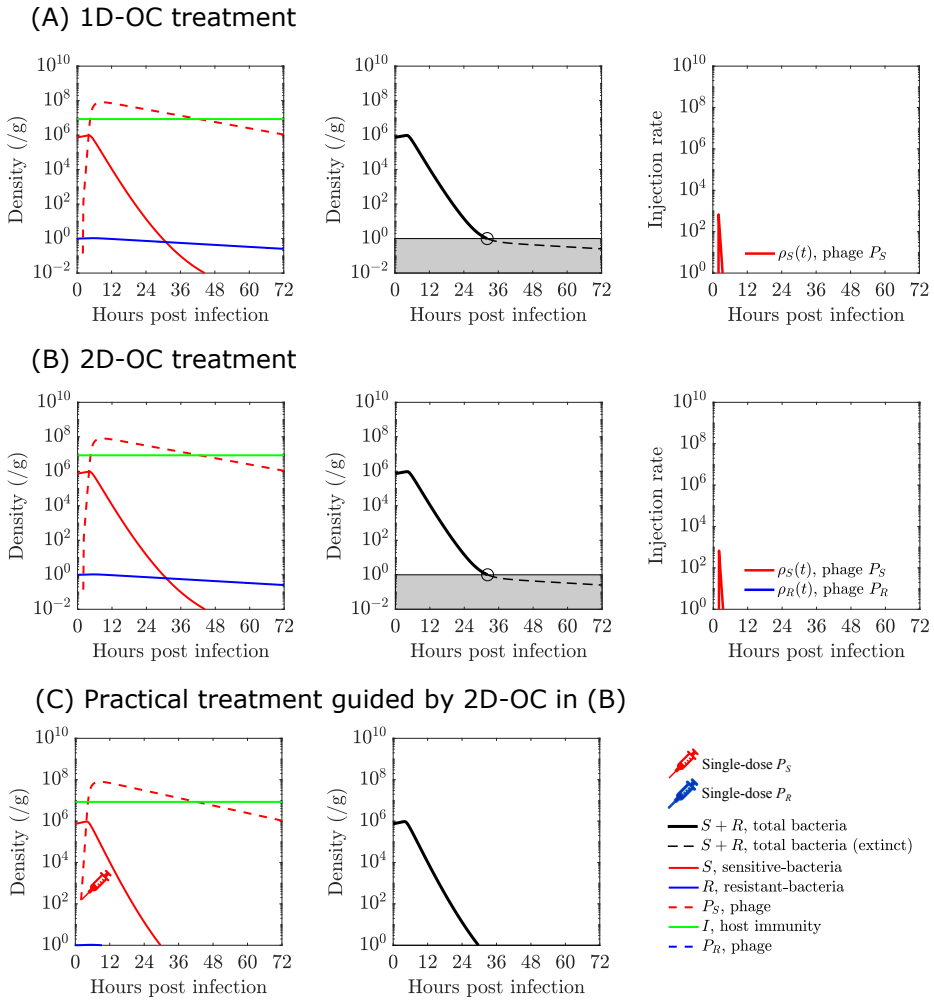

Figure 2.7: Comparison of time series of population densities with different treatments in the high level of baseline immune response, $I_0 = 8.5 \times 10^6$ cell/g. (A) Optimal injection rate, $\rho_S(t)$, is obtained by solving control problem (2.17) with tuned regulator weight $\theta_u = 10^{11}$ (the largest regulator weight on treatment costs). The Hamiltonian-based algorithm is terminated after $k = 11$ iterations and output control u_1^k. The numerical value of objective cost in problem (2.17) with control u_1^k is 0.1024, and the convergence indicator $|\Theta(u_1^k)| \approx 1.68 \times 10^{-8}$. Bacteria is eliminated around 30 hrs post infection. (B) Optimal injection rate, $\rho_S(t)$ and $\rho_R(t)$, is obtained by solving control problem (2.9) with tuned regulator weight $\theta_u = 10^{11}$. The Hamiltonian-based algorithm is terminated after k iterations and output control u^k, where $k = 10$. The numerical value of objective cost in problem (2.9) with control u^k is 0.1024, and the convergence indicator $|\Theta(u^k)| \approx 9.34 \times 10^{-7}$. Note that the optimal injection rate of phage P_R is nearly zero, *i.e.*, $\rho_R(t) \approx 0\ \forall t \in [t_0, t_f]$. Thus, the optimal injection rates solved from 2D-OC and 1D-OC are nearly identical, *i.e.*, $\rho_S(t)$ is a single-pulse signal centered at $t = 2$ hrs. Bacteria is eliminated around 30 hrs post infection. (C) The practical therapeutic treatment is obtained from optimal injection rate in (B): single-dose, P_S phage dose, is injected at two hours post infection with amount of 5×10^2PFU. Bacteria is eliminated around 30 hrs post infection. See model parameters and simulation details in Sect. 2.4.2.

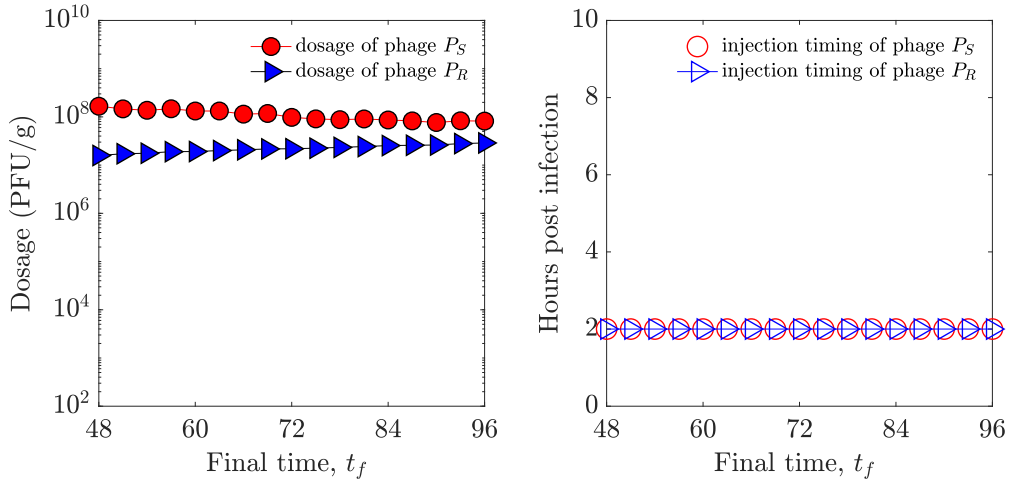

Figure 2.8: The optimal timing and dose in practical therapeutic treatment with variation of final time from 2 to 4 days (*i.e.*, $t_f \in [48, 96]$ hrs). The baseline immune response is fixed at $I_0 = 6 \times 10^6$ cell/g. (Left) Minimal phage amount for eliminating bacterial cells with variation in final time t_f. Optimal dosages of phage P_S (red) and phage P_R (blue) are maintained at approximately 10^8 (PFU/g) and 10^7 (PFU/g) respectively. (Right) Optimal timing (defined by the peak of the optimal phage injection profile) of two types of phage injection with variation in final time t_f. The timings of injecting two types of phage dose are both about two hours post infection (*i.e.*, $T_{P_S} = T_{P_R} \approx 2$ hrs). See model parameters and simulation details in Sect. 2.4.2

Table 2.1: Parameters and initial conditions in the system (2.1) from source [69]

Parameters	**Value**
r, maximum growth rate of bacteria	0.75 h^{-1}
r', maximum growth rate of phage-resistant bacteria	0.675 h^{-1}
μ, probability of emergence of phage-resistant mutant per cellular division	2.85×10^{-8}
K_C, carrying capacity of bacteria (wild-type)	1.0×10^{10} CFU/g
K_C, carrying capacity of bacteria (immunodeficient hosts)	8.5×10^{11} CFU/g
β, burst size of phage	100
w, decay rate of phage	0.07 h^{-1}
ϵ, killing rate parameter of immune response	8.2×10^{-8} g/(h cell)
α, maximum growth rate of immune response	0.97 h^{-1}
K_I, maximum capacity of immune response	2.4×10^{7} cell/g
K_I, maximum capacity of immune response (no innate immune activation)	same as I_0
K_D, bacterial concentration at which immune response is half as effective	4.1×10^{7} CFU/g
K_N, bacterial concentration when immune response growth rate is half its maximum	1.0×10^{7} CFU/g
ϕ, adsorption rate of phage	5.4×10^{-8} g/(h PFU)
P_C, phage density at half saturation	1.5×10^{7} PFU/g
S_0, initial bacterial density	7.4×10^{7} CFU/g
S_0, initial bacterial density (immunodeficient hosts)	7.4×10^{5} CFU/g
R_0, initial phage-resistant bacterial density	1 CFU/g
I_0, initial immune response	2.7×10^{6} cell/g
I_0, initial immune response (immunodeficient hosts)	$3 \times 10^{6} \sim 8.5 \times 10^{6}$, cell/g
$P_S(0)$, initial WT phage density	0 PFU/g
$P_R(0)$, initial host-range mutant phage density	0 PFU/g
ρ_{max}, maximal phage dose injection rate	10^{9} PFU/(h g)

CHAPTER 3

OPTIMIZING THE USE OF MULTIPHAGE COCKTAILS FOR TREATMENT OF IMMUNODEFICIENT HOSTS IN ECO-EVOLUTIONARY DYNAMICS

3.1 Introduction

The addition of therapeutic phage to treat multi-drug resistant (MDR) pathogens imposes a strong selective pressure for the emergence of phage-resistant bacteria. We have already established through modeling and in *vivo* experiments that resistant bacteria proliferate in Myd88$^{-/-}$ mice, corresponding to the failure of phage therapy [69]. In Chapter 2, we presented how a phage cocktail can be used to clear an infection in immunodeficient hosts from a bacterium that can develop resistance to one of the two injected phage [31] but the problem of how to treat an infection where bacteria can develop resistance to both phage is still poorly understood.

One idea proposed to combat resistance is 'training' phage by using their natural capacity to evolve to counter resistance before applying them in phage therapy [34]. For example, consider an environment inoculated with a target bacteria and potential therapeutic phage. Over time, the selective pressure induced by phage infection and lysis can lead to the emergence of phage-resistant bacteria. This emergence may itself drive the selection of host-range mutant phage [82, 83, 84, 85, 86, 87, 88, 89]. Although coevolutionary dynamics between phage and bacteria can be subject of inquiry in their own right, here we are interested in the extent to which such dynamics may improve control at the outset, if appropriately leveraged.

In this chapter, we limit our study to to a post-hoc analysis. That is, we assume that we have already established a phage-bacteria infection network that arose as a result of coevolutionary training, exploiting the pre-identified evolved phage able to infect partial

and complete resistant bacteria. We select those 'trained' phage from coevolution. We consider every selected phage can infect bacteria via binding to a specific receptor on the cell surface. Then, the generic bacteria-phage infection networks consists multiple pre-selected trained phage and a set of bacteria strains that are characterized by a sequence of binary sites, each site denotes that bacteria can be either resistant or sensitive to a given trained phage. As discussed in Sect. 3.4.1, the treatment with generic infection networks is not curative when phage are less efficient (e.g., low adsorption rate and high decay rate). Then, we focus on two classes of networks. First, we add a contingent specialist phage into networks. The added contingent specialist phage only targets WT bacteria (*i.e.,* sensitive to all trained phage) with high specificity. Second, we add a generalist phage into networks. The added generalist phage can infect all bacteria strains except a fully resistant one (*i.e.,* resistant to all trained phage), with associated costs of generalism [90]. In Sects. 3.4.2 and 3.4.3, we address how adding *contingent specialist* phage or *generalist* phage can improve therapy in certain conditions.

3.2 Eco-evolutionary synergy model

We consider a model where bacteria evolve in a discrete phenotypic space, against a fixed set of different types of phage present in the therapeutic phage library. If there are N phage types, a bacterium phenotype is characterized by a binary sequence of length N: $\sigma = \{\sigma[1], ..., \sigma[N]\}$. The k^{th} binary variable ($\sigma[k]$) represents the absence or presence of resistance to phage type k: $\sigma[k] = 0$ means that the host is resistant to type k phage and $\sigma[k] = 1$ means that the host is sensitive to type k phage. Overall, the state space of host (bacterial) phenotypes is denoted by $\mathcal{S}_N = \{0, 1\}^N$. For example, when $N = 3$, the state space of host traits is $\mathcal{S}_N = \{111, 011, 101, 110, 001, 010, 100, 000\}$. In general, there are 2^N host phenotypes.

We assume that mutations are restricted to occur between *adjacent* types (differing by a single resistance trait) in state space $\mathcal{S}_N$. That is host types with binary sequence σ can

mutate to another host types with binary sequence σ' if $\|\sigma - \sigma'\|_1 = \sum_{j=1}^{N} |\sigma[j] - \sigma'[j]| = 1$, note that using 1-norm $\|.\|_1$ to measure the distance between two binary sequences is equivalent to the *Hamming distance*. Here, we assume that the mutation probability μ (*i.e.,* probability of emergence of phage-resistant mutant per cellular division) is universal for all types of hosts. Mutations are random, given a mutation event, the probability of mutating to any adjacent type is the same, $\mathbb{P}(\sigma \to \sigma';\ \|\sigma - \sigma'\|_1 = 1) = 1/N$, where N is the length of phenotype binary sequence.

In our model we couple basal growth rate to resistance traits in order to mimic a growth-rate-resistance trade-off [91, 82]. Denote the growth rate of a host type with phenotype $\sigma \in \mathcal{S}_N$ as r, the growth rate is a increasing function of $\|\sigma\|_1 = \sum_j \sigma[j]$. The simplest way of modeling growth-rate-resistant trade-off is using linear function,

$$r(\sigma) = r_{min} + \left(\frac{r_{max} - r_{min}}{N}\right) \|\sigma\|_1 , \tag{3.1}$$

so that the basal growth rate of wild type (sensitive to all types of phage) is r_{max} and the growth rate of the complete-phage-resistant type is r_{min}. The trade-off linearity assumption is not universal, this relationship could be nonlinear, $r(.)$ can be either convex (rate at which costs in growth rate is decelerating) or concave (rate at which costs in growth rate is accelerating), which depends on the specific biological systems.

Here we extend a nonlinear dynamics model of bacteria, phage and the innate immune system [69, 68] by incorporating changes in population dynamics with interaction networks and life history traits via a eco-evolutionary multi-strain framework [82, 92, 83, 93]. In our model the infection of a bacterium triggers a sequence of infection stages after which lysis takes place. We denote the density of bacteria σ by S_σ, the density of virus j by P_j, the infected bacteria σ that are infected by virus j at stage ℓ as $E^{(\ell)}_{\sigma,j}$, and the density of host

immunity by I. Our model of the eco-evolutionary synergy dynamics is,

$$
\begin{aligned}
\dot{S}_\sigma &= \overbrace{r(\sigma)S_\sigma\left(1-\frac{B}{K_C}\right)(1-\mu)}^{\text{growth}} + \overbrace{\frac{\mu}{N}\sum_{\{\sigma':\ \|\sigma'-\sigma\|=1\}} r(\sigma')S_{\sigma'}\left(1-\frac{B}{K_C}\right)}^{\text{mutations}} \\
&\quad - \overbrace{S_\sigma\sum_{j'}F_\sigma(P_{j'})}^{\text{infection}} - \overbrace{\frac{\epsilon I S_\sigma}{1+(B/K_D)}}^{\text{immune killing}}, \\
\dot{E}^{(1)}_{\sigma,j} &= \overbrace{S_\sigma F_\sigma(P_j)}^{\text{infection}} - \overbrace{\frac{\epsilon I E^{(1)}_{\sigma,j}}{1+(B/K_D)}}^{\text{immune killing}} - \overbrace{\eta_1 E^{(1)}_{\sigma,j}}^{\text{transition}}, \\
\dot{E}^{(\ell)}_{\sigma,j} &= \overbrace{\eta_{\ell-1}E^{(\ell-1)}_{\sigma,j}}^{\text{transition}} - \overbrace{\frac{\epsilon I E^{(\ell)}_{\sigma,j}}{1+(B/K_D)}}^{\text{immune killing}} - \overbrace{\eta_\ell E^{(\ell)}_{\sigma,j}}^{\text{transition}},\ \ell=2,...,L, \\
\dot{P}_j &= \overbrace{\beta_j\eta_L\sum_\sigma E^{(L)}_{\sigma,j}}^{\text{viral lysis}} - \overbrace{\phi_j P_j\sum_\sigma M_{\sigma,j}S_\sigma}^{\text{adsorption}} - \overbrace{w_j P_j}^{\text{decay}} \\
\dot{I} &= \overbrace{\alpha I\left(1-\frac{I}{K_I}\right)\left(\frac{B}{K_N+B}\right)}^{\text{immune stimulation, activation and immune saturation}},
\end{aligned}
\tag{3.2}
$$

where $B = \sum_{\sigma'} S_{\sigma'} + \sum_{\sigma,j,\ell} E^{(\ell)}_{\sigma,j}$ denotes the total bacteria density, $F_\sigma(P_j)$ denotes the infection rate of viruses of type j on hosts of type σ, e.g. $F_\sigma(P_j) = M_{\sigma,j}\phi_j P_j / \left(1+\frac{P_j}{P_C}\right)$ is the per-capita phage-induced bacterial lysis rate that characterizes the effect of phage saturation during the infection. The parameters ϕ_j and β_j are the adsorption rate and burst size of virus j (which we assume is independent of bacteria type σ). To simplify the model we assume that $\beta_j = \beta$ and $\phi_j = \phi$ for all j's. Here, $\mathcal{M}$ denotes the infection matrix, where $M_{\sigma,j} = 1$ if virus j can infect bacteria σ and $M_{\sigma,j} = 0$ if virus j cannot infect bacteria σ. In this chapter, we consider a small system with $N = 3$. First, we consider the *generic* virus-host interactions, which are encoded by a $2^3\ (=8)$ by 3 infection matrix, denoted by

$\mathcal{M}^0$,

$$\mathcal{M}^0 = \begin{array}{c} \begin{matrix} P_1 & P_2 & P_3 \end{matrix} \\ \begin{bmatrix} 1 & 1 & 1 \\ 0 & 1 & 1 \\ 1 & 0 & 1 \\ 1 & 1 & 0 \\ 0 & 0 & 1 \\ 0 & 1 & 0 \\ 1 & 0 & 0 \\ 0 & 0 & 0 \end{bmatrix} \end{array} \begin{matrix} S_{111} \\ S_{011} \\ S_{101} \\ S_{110} \\ S_{001} \\ S_{010} \\ S_{100} \\ S_{000}. \end{matrix} \tag{3.3}$$

In Sect. 3.4, we show that bacterial cells cannot be eliminated given infection networks $\mathcal{M}^0$ (with present model parameters) due to the chosen low density of host immunity I and low adsorption rate ϕ. In our system, a given phage P_j is determined by an optimization problem (3.11) only after it was injected following the therapy strategy (2 hrs post-infection), before which P_j is set to 0.

In this chapter, we consider two modified infection networks. We define a 8 by 4 infection matrix $\mathcal{M}^c$ by adding a *contingent specialist phage* (P_c), that only targets for WT bacteria (fully sensitive type, $\|\sigma\|_1 = 3$). To account the host range trade-off, *i.e.,* a phage with a broader host range has less advantageous life-history traits compared to viruses with a narrower host range [94], we use a parameter $\alpha_\phi > 1$ to control the benefit of contingent specialist phage, the adsorption rate of P_c can be written as $\phi_c = \alpha_\phi \phi$. Such a scenario could be relevant for real biological systems. Imagine that the probability of infection is driven by the binding affinity between a receptor on the bacterial membrane and a ligand on the phage tail. Let's assume that there are three binding sites on the two proteins, and that the binding affinity is determined by the number of sites that are able to bind (match) given their biochemical properties. The *contingent specialist phage* ligand perfectly matches the WT bacterium receptor, but the binding affinity depends on the binding sites in a coopera-

tive way so that any (phenotypic) mutation in the receptor sites will hinder P_c ability's to infect. The other 3 phage will be able to infect if a specific ligand site can bind to just one specific WT receptor site, and each of them target a different receptor site. So a single site mutation will make the WT bacterium resistant to only one of the standard phage. But the lower cooperativity in the binding interaction would result in a lower adsorption rate for these phage compared to P_c. $\mathcal{M}^c$ can be written as

$$\mathcal{M}^c = \begin{array}{c} \begin{matrix} P_c & P_1 & P_2 & P_3 \end{matrix} \\ \begin{bmatrix} 1 & 1 & 1 & 1 \\ 0 & 0 & 1 & 1 \\ 0 & 1 & 0 & 1 \\ 0 & 1 & 1 & 0 \\ 0 & 0 & 0 & 1 \\ 0 & 0 & 1 & 0 \\ 0 & 1 & 0 & 0 \\ 0 & 0 & 0 & 0 \end{bmatrix} \end{array} \begin{matrix} S_{111} \\ S_{011} \\ S_{101} \\ S_{110} \\ S_{001} \\ S_{010} \\ S_{100} \\ S_{000}. \end{matrix} \tag{3.4}$$

Including this contingent specialist phage may lead to the emergence of *competitive release*, so the corresponding treatments must be designed carefully, see Sect. 3.4.

As an alternative, instead of using a contingent specialist phage, we add a *generalist phage* (P_g), that can infect all bacteria cells except the fully resistant one ($\|\sigma\|_1 = 0$). In addition, we use a parameter ϵ_ϕ to model the cost of this generalist phage [95, 94]. The adsorption rate of P_g depends on bacterium phenotype σ, *i.e.,* $\phi_g(\sigma)$. Following our previous reasoning on ligand-receptor binding, P_g ligand would also perfectly match the WT receptor. The generalist phage could infect the bacteria when *any* of the three binding sites match the corresponding receptor site. An attempt to bind an incompatible site would result in infection failure, resulting in an adsorption cost that increases with the number of

mutated sites from the WT bacterium (in our case, $\left(1 - \frac{\|\sigma\|_1}{N}\right)$). For simplicity, we use a linear function,

$$\phi_g(\sigma) = \left[(1 - \epsilon_\phi)\frac{\|\sigma\|_1}{N}\right]\phi, \tag{3.5}$$

where $N = 3$. $\mathcal{M}^g$ can be written as

$$\mathcal{M}^g = \begin{array}{c} \begin{matrix} P_g & P_1 & P_2 & P_3 \end{matrix} \\ \begin{bmatrix} 1 & 1 & 1 & 1 \\ 1 & 0 & 1 & 1 \\ 1 & 1 & 0 & 1 \\ 1 & 1 & 1 & 0 \\ 1 & 0 & 0 & 1 \\ 1 & 0 & 1 & 0 \\ 1 & 1 & 0 & 0 \\ 0 & 0 & 0 & 0 \end{bmatrix} \end{array} \begin{matrix} S_{111} \\ S_{011} \\ S_{101} \\ S_{110} \\ S_{001} \\ S_{010} \\ S_{100} \\ S_{000}. \end{matrix} \tag{3.6}$$

Our deterministic model assumes that the infected individuals are lysed with a mean infection period τ_{inf} after all L stages are complete. The length of each stage has a transition rate η_ℓ (corresponds to a mean transition period $1/\eta_\ell$), here we assume all the transition rates are same, *i.e.,* $\eta_\ell = \eta$ for all ℓ's. The advantage of adding the intermediate latent stages is to ensure viral reproduction does not occur immediately after a virus enters a host. This deterministic model is the average of a stochastic model where the length of an infection is modeled as the sum of L independent exponential random variables (each with mean period $1/\eta$), yielding an Erlang distributed infection time. Note that

$$\tau_{\text{inf}} = \sum_{\ell=1}^{L} 1/\eta_\ell = L/\eta, \tag{3.7}$$

so, the mean transition period $(1/\eta)$ for each stage is equal to τ_{inf}/L. In a special case of $L = 1$, the infectious period is exponentially distributed with a mean period τ_{inf}. In our model, we choose $L = 2$ which is the lowest L yielding an unimodal distribution of infectious period in the stochastic extension of the model.

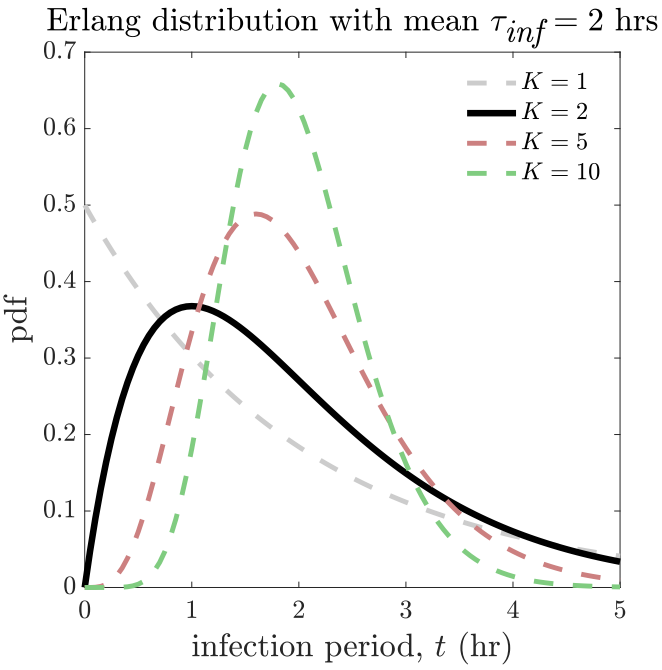

Figure 3.1: The probability density function (pdf) of Erlang distributions with variations in L, scale parameter is τ_{inf}/L (mean transition period during each stage) and shape parameter is L (number of stages). The mean infectious period τ_{inf} is fixed as 2 hrs. We choose $L = 2$ in this study.

In this model we assume that phage types challenging the bacterial population are fixed and don't evolve. This mimics a situation where phage categories have been pre-selected or trained for therapy separately. These in principle are not related phylogenetically as evolving one from the other would take times much longer than the infection timescales, when at all possible. In this model we neglect the evolution of new phage mutants that evolve from the injected therapeutic phage, which could generate the emergence of counter-resistance to bacteria as well as complex co-evolutionary patterns. This is the same as assuming that the emergence of counter-resistance would be rare on typical infection timescales.

3.3 Initial condition optimization

The general goal is to optimize the phage therapy administrations so to minimize the total bacterial population while penalizing the treatment costs. From a practical therapeutic perspective, in this chapter we want to find the minimal phage dosage required to eliminate bacteria. We assume the bacterial population is eliminated if there exists a time $\tau \in [t_0, t_f]$ such that $(\sum_\sigma S_\sigma) < n_{ext}$, where $\sum_\sigma S_\sigma$ is the total uninfected bacterial population density and $n_{ext} = 1$ CFU/g is the hard threshold of bacteria elimination. In [31, 69] we found that injecting all phage as soon as possible ('early hit') is a plausible treatment strategy. Hence, we consider an initial condition optimization problem. The initial condition $x(t_0) = [S(t_0), E^{(1)}(t_0), ..., E^{(L)}(t_0), P(t_0), I(t_0)]^T$, where t_0 is the start of treatment.

To achieve the practical goal of eliminating bacteria with minimum dosage, we propose the following optimization problem. Define the feasible domain $\mathcal{D}$ as

$$\mathcal{D} = \overbrace{\{P(t_0)| \text{ exists } \tau \in [t_0, t_f] \text{ such that } \sum_\sigma S_\sigma(\tau) < n_{ext}\}}^{\text{bacteria elimination}} \bigcap \overbrace{\{P(t_0)| \ \|P(t_0)\|_1 \leq P_{max}\}}^{\text{max dosage constrain}}, \tag{3.8}$$

where P_{max} is the fixed max dosage. The cost is the total dosage, $\mathcal{J}(P(t_0)) = \|P(t_0)\|_1$. There are N virus types in $\mathcal{M}^0$ networks and $N+1$ virus types in $\mathcal{M}^c$ and $\mathcal{M}^g$ networks. The optimization problem can be written as (subject to system (3.2))

$$\min_{P(t_0)\in\mathcal{D}} \mathcal{J}(P(t_0)) \,, \tag{3.9}$$

which is equivalent to

$$\mathcal{J}(P(0)) = \begin{cases} \|P(t_0)\|_1 & \text{if } P(t_0) \in \mathcal{D} \\ \infty & \text{otherwise} \end{cases}. \tag{3.10}$$

An assumption for optimization variables. We assume the initial phage dosages are all equal in the optimal treatment an account of symmetry, *i.e.,* $P_1(t_0),\ P_2(t_0), ...,\ P_N(t_0)$ with one exception: either the contingent specialist or generalist phage. Note that system (3.2) is 'symmetric' in virus types $1, ..., N$ (i.e., reordering makes no difference in the system dynamics and output). Suppose the initial dosages are different, the first effect of different dosages would be to favour the growth of the bacteria resistant to the max dosage phage due to reduced competition of the other strains. This may give more time for multi-resistance to arise, especially in an high asymmetrical dosage where phage with the maximum dosage would wipe out corresponding susceptible bacteria population (also depleting part of the population susceptible to the other phage) and then decay. This implies that we may need to inject more corresponding phage into the system to control the bacteria that are resistant to the maximal dosed phage. On the other hand, if we neglect the complex host-host interactions (or view it as a second order effect) and consider the virus-host interactions in a one-to-one structure, *i.e.,* assuming 'weak coupling', then minimizing the total dosage is equivalent to minimize dosage component-wise, which supports the equal dosage assumption. Hence, difference dosages may not be a feasible solution. The above argument motivates us to posit that optimal dosages $P_1(t_0),\ P_2(t_0), ...,\ P_N(t_0)$ should be equal. This assumption may not be true in general, system (3.2) is a complex nonlinear system with multiple latent stages (a de facto delayed effect). Nevertheless, using this assumption, there are only two optimization variables, $P_i(t_0)$ ($i \in \{c, g\}$) and $P_1(t_0)$ (dosage of symmetric phage types $1, 2, ..., N$) and we can solve the optimization problem (3.9) at a greatly reduced computational cost. We test this assumption in Appendix 3.6.3 by perturbing the injection strategy around the equal dosages situation checking that this is indeed a local optimum (non-equal dosages with the same or lower $\|P(t_0)\|_1$ would fail). In addition, we will propose a numerical algorithm to solve the optimization problem (3.9) without equal dosage assumption in Sect. 3.5.

With the above assumption, the reduced optimization problem is

$$\min_{\mathcal{D}} \mathcal{J}(P_i(t_0), P_1(t_0)) \,, \tag{3.11}$$

where $\mathcal{J} = \|P(t_0)\|_1 = P_i(t_0) + NP_1(t_0)$ and $i \in \{c, g\}$. Here we adopt an adaptive (refined) grid search method to solve the problem (3.11), see Algorithm 1 in Sect. 3.6.1 for details.

3.4 Results

Parameters and initial condition. The model parameters and initial conditions of system (3.2) are given in Table 3.1. In this chapter, we only focus on developing treatment in immunodeficient scenarios, where the innate immune response is treated as a constant. Throughout this chapter, the density of immune response is fixed at a low level, $I_0 = 5 \times 10^6$ cell/g. We choose $N = 3$ (for convenience and low computational costs). The *in silico* experiments run for 3 days post infection and all the treatments start at 2 hours after initialization (consistent with *in vivo* treatments in [69]), we thus set $t_0 = 2$ hrs and t_f = 72 hrs. Before treatment, we run system (3.2) from 0 to t_0 with the initial condition $x(0) = [S(0), E^{(1)}(0), ..., E^{(L)}(0), P(0), I(0)]^T$, where $S(0) = [-S_\sigma(0)-]^T$ is fixed with high abundance dominate WT bacteria and low abundance one-step resistant ($\|\sigma\| = 1$) bacteria resistant bacteria (other bacteria types have zero initial density), $E^{(\ell)}(0) = [-E^{(\ell)}_{\sigma,j}(0)-]^T$ and $P(0) = [-P_j(0)-]^T$ are zero vectors.

3.4.1 8 by 3 generic infection matrix, $\mathcal{M}^0$

When infection matrix is $\mathcal{M}^0$, we find that bacterial cells cannot be eliminated for any initial treatment dosage given constraints that dosage must be less than $P_{max} = 10^9$ PFU/g. The treatment failure is not due to the outgrowth of fully resistant bacteria. As discussed in [68], synergistic elimination (*i.e.,* phage and immune response) occurs when the phage

drive the bacterial population below some 'certain level' (depends on phage life-history traits, $\omega,\ \beta,\ \phi$) where the constant (or static) innate immune response alone can eliminate the bacteria. Since the adsorption rate is relatively low ($\phi = 1.5 \times 10^{-8}$ g/(h PFU)) and phage decay rate is relatively high ($\omega = 0.1$/h) comparing to the parameter values used in [69], the bacterial population cannot be driven below the level that innate immune response can clear, see Fig. 3.2.

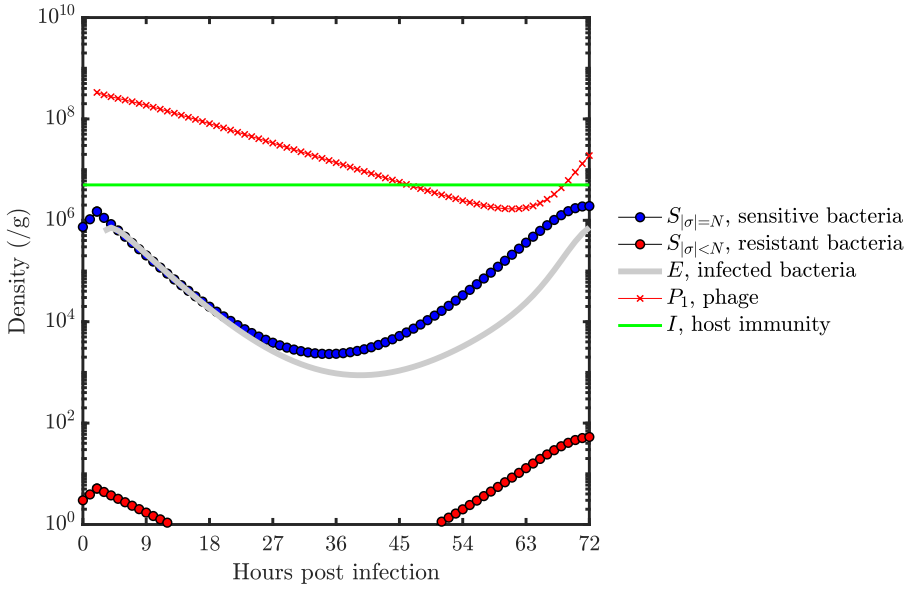

Figure 3.2: Time series of population densities with low mutation probability ($\mu = 10^{-9}$) and high initial dosage treatment ($P_1(t_0) = P_{max}/3$). See model parameters in Table 3.1.

3.4.2 8 by 4 infection matrix with a contingent specialist phage, $\mathcal{M}^c$

In this section, we consider a 8 by 4 infection matrix with a contingent specialist phage, $\mathcal{M}^c$. Given our model and parameter assumptions the adaptive grid search algorithm results in a small amount of contingent specialist phage and a small amount of symmetric specialist phage when the benefit of contingent specialist phage is low ($\alpha_\phi = 2$) to eliminate bacteria, but a much higher symmetric specialist phage dosage is required when benefit is high ($\alpha_\phi = 10, 50, 100$), see Fig. 3.3. We might wonder why do we need more dosage (in total) when contingent specialist phage are associated with more benefits? This 'counterintuitive' result

can be explained by the so-called *competitive release* [96, 97].

Competitive release is the result of an 'ecological balance': when two (or more) subspecies compete for the same resources with one species dominating the other, if the dominant species is removed, this can provide the needed release from competition that can allow the less dominant species to flourish [98]. For a 8 by 4 infection networks with a contingent specialist phage, there are 8 types of bacteria competing for resources and the sensitive bacteria is the dominant species without therapy. Hence, the rapid decline of sensitive bacterial population could lead to the outgrowth of partially or fully resistant bacterial population. To control the outgrowth of partially or fully resistant bacteria populations, we have to add a significant amount of symmetric specialist phage.

A contingent specialist phage can rapidly drive down niche competition amongst bacterial cells, facilitating the rapid outgrowth of other bacteria populations. Therefore competitive release is reinforced by higher α_ϕ, and more corresponding phage dosages are needed to eliminate resistant bacterial cells. To demonstrate this complex dynamics, we show the population densities given high α_ϕ but low dosages (in contrast to optimal treatment where symmetric specialist dosage is high), see Fig. 3.4. Sensitive cells are wiped out in 5 hours post infection, which leads to the fast growth of other type bacterial cells, low dosage treatment fails in this scenario while it would succeed with lower α_ϕ. Note that system (3.2) is a mean-field model, which is justified by the large sizes of bacterial and phage populations. We test the deterministic optimum (*i.e.,* optimal treatment in deterministic model) using stochastic simulations, the results are consistent, see Appendix 3.6.2 for more details.

In Figure 3.3, we observe that no treatment can eliminate the bacterial cells when mutation probability is high due to the outgrowth of resistance bacteria population. Albeit the risk of competitive release, the treatment range in mutation probability becomes wider when contingent specialist phage is associated with higher benefit (*i.e.,* higher α_ϕ yields wider range of mutation probability that bacteria can be eliminated). The contingent specialist phage with high benefit can eliminate WT bacteria less than 5 hours, there is no time

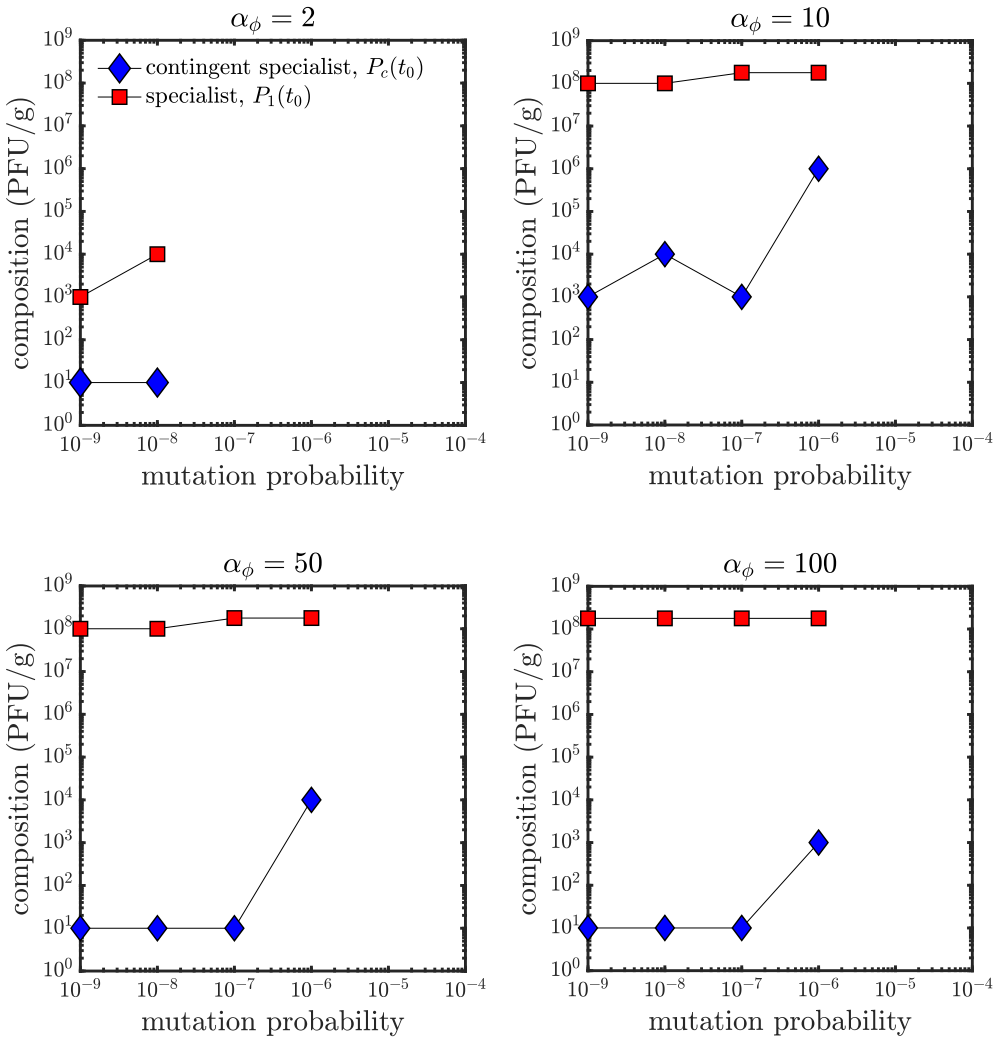

Figure 3.3: Minimal initial dosages for eliminating bacterial cells using optimized treatments as a function of mutation probability μ and contingent phage benefit α_ϕ. Four *in silico* experiments example dynamics (high and low mutation probabilities with high and low contingent phage benefits) are provided in Fig. 3.5. The timings of injecting two types of phage dose (blue for contingent phage dosage and red for symmetric specialist dosage) are fixed at two hours post infection. See model parameters in Table 3.1.

for multi-resistant bacteria to raise though the mutation probability is high, see Fig. 3.5(Bottom right). On the other hand, a longer time is needed for contingent specialist phage with lower benefit to eliminate WT bacteria, which gives more time for multi-resistant bacteria to raise and grow, see Fig. 3.5(Bottom left). This also explains why increasing the mutation

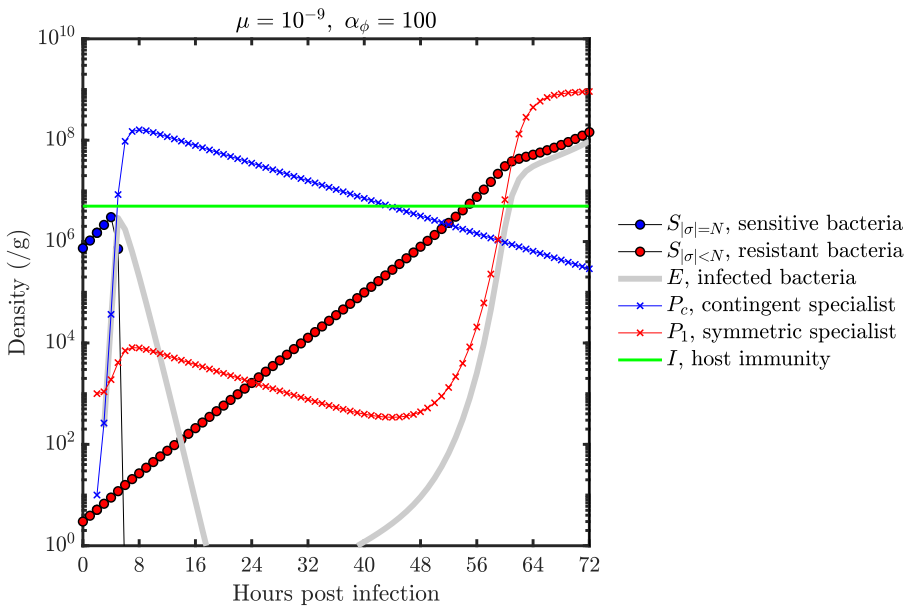

Figure 3.4: Population densities with low mutation probability and high contingent specialist phage benefit provided low initial dosages of both phage types (10 PFU/g). The present treatment is not curative (bacteria cells are not eliminated). See model parameters in Table 3.1.

probability, higher dosages of contingent specialist phage are necessary for therapy to be successful.

In summary, we found that the 8 by 4 infection networks with a contingent specialist phage can avert the failure in generic 8 by 3 infection networks. The benefits of contingent specialist phage are a 'double-edged sword', we must be careful to design treatment (dosages as a function of α_ϕ and μ) due to the interplay between competitive release and multi-resistance emergence.

3.4.3 8 by 4 infection matrix with a generalist phage, $\mathcal{M}^g$

Instead of using a contingent specialist phage, we add a generalist phage (P_g) to system. The infection matrix $\mathcal{M}^g$ is given by Eq. 3.6. Given our model and parameter assumptions the adaptive grid search algorithm result in a small amount of generalist phage and a small amount of symmetric specialist phage when the cost of generalist phage is relatively low (e.g., $\epsilon_\phi = 0.1, 0.2$) to eliminate bacteria, see Fig. 3.6. As shown in Fig. 3.7, the density of

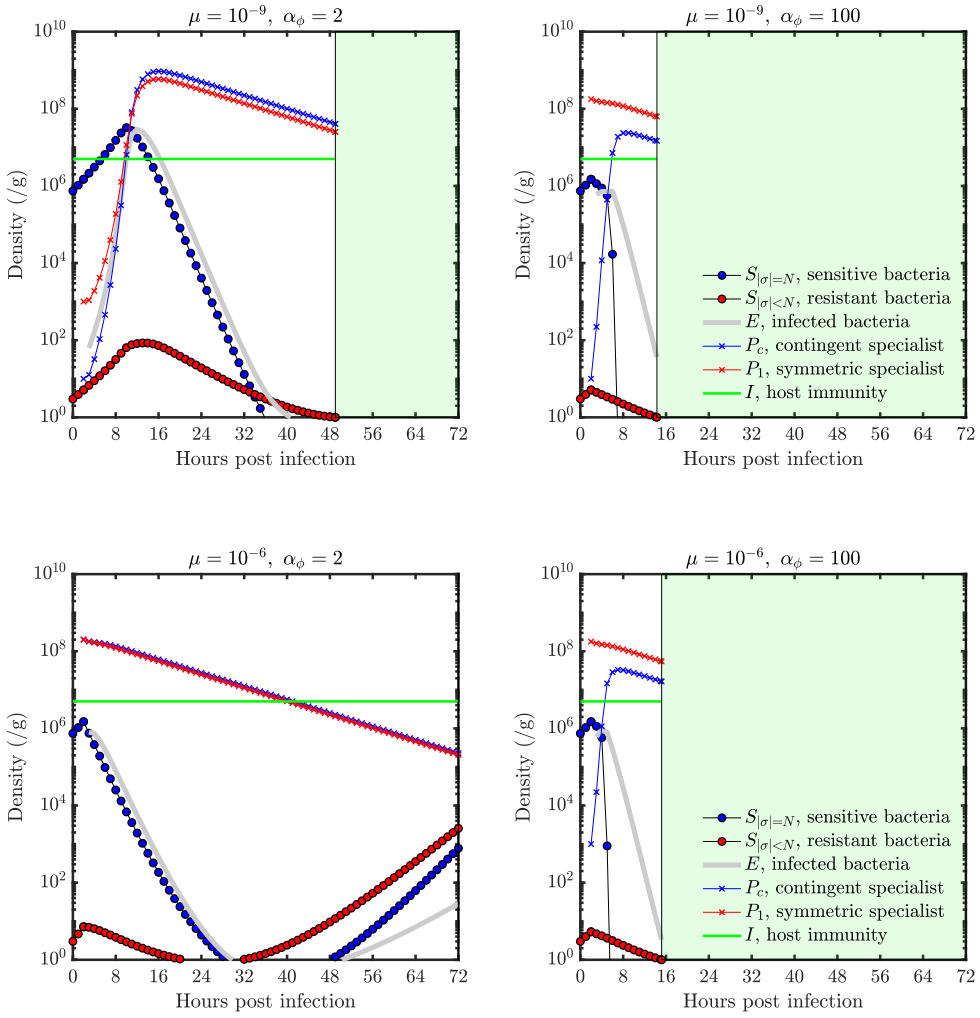

Figure 3.5: Comparison of time series of population densities with different mutation probabilities and contingent phage benefits. (Top left) Bacteria is eliminated around 50 hrs post infection in the case of low mutation probability and low benefit. (Top right) Bacteria is eliminated around 15 hrs post infection in the case of low mutation probability and high benefit. (Bottom left) Bacterial cells are not eliminated due to the outgrowth of resistant bacteria, in the case of high mutation probability and low benefit scenario. (Bottom right) Bacteria is eliminated around 16 hrs post infection in the case of high mutation probability and high benefit. See model parameters in Table 3.1.

specialist phage is uniformly (slightly) higher than the density of generalist phage (given the same initial condition) due to the costs for generalist phage. When the cost of generalist phage is relatively high (e.g., $\epsilon_\phi = 0.5, 0.9$), adding generalist phage cannot significantly improve treatment so that the present 8 by 4 system behaves similar to generic 8 by 3

system, and bacterial cells cannot be eliminated. Next, we investigate the dynamics of bacteria, phage, and the innate immune response and explain why only a small amount of phage is required to eliminate bacteria.

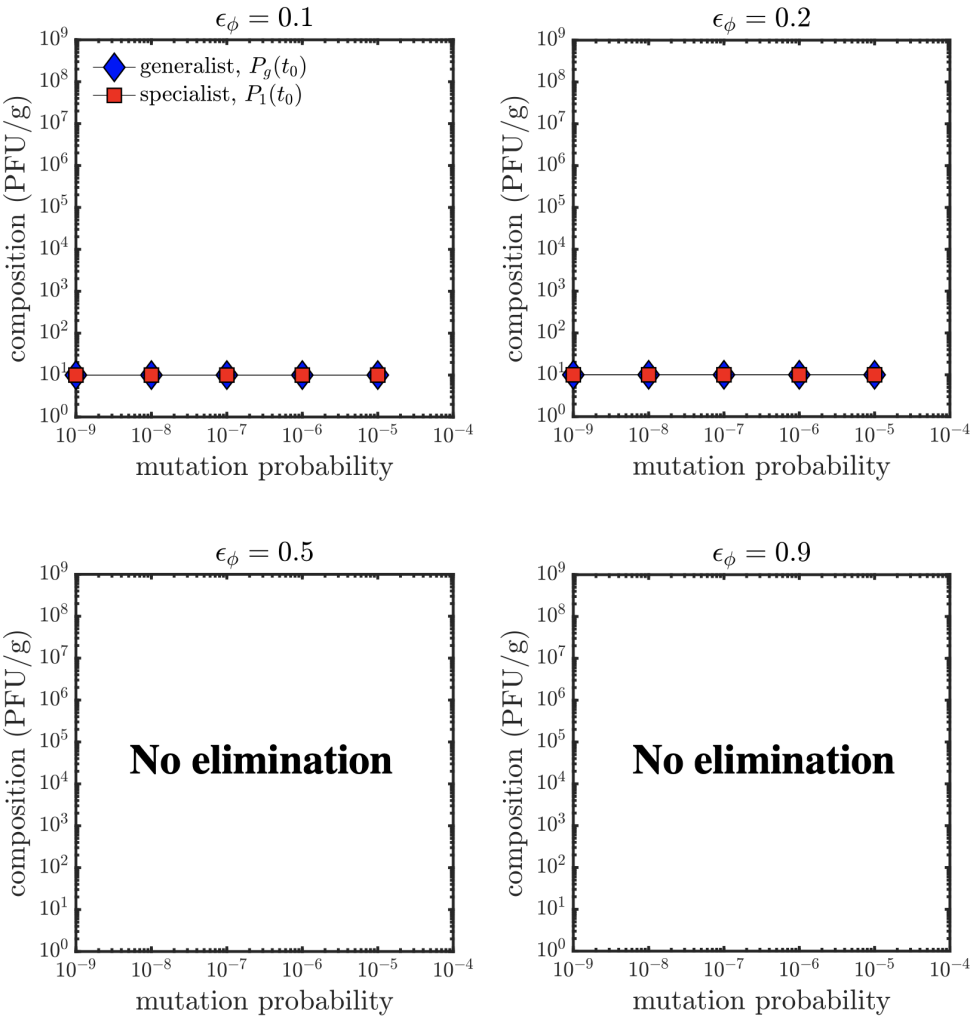

Figure 3.6: Minimal initial dosages for eliminating bacterial cells using optimized treatments with variations in mutation probability μ and generalist phage cost ϵ_ϕ. Two *in silico* experiments (high and low mutation probabilities with a relative low generalist phage cost, $\epsilon_\phi = 0.2$) are provided in Fig. 3.7. The timings of injecting two types of phage dose (blue for generalist phage dosage and red for symmetric specialist phage dosage) are fixed at two hours post infection. See model parameters in Table 3.1.

To begin, we ask a 'simple' question: *if a treatment can eliminate bacterial population with some phage dosage, does this implies bacterial population can be eliminated with*

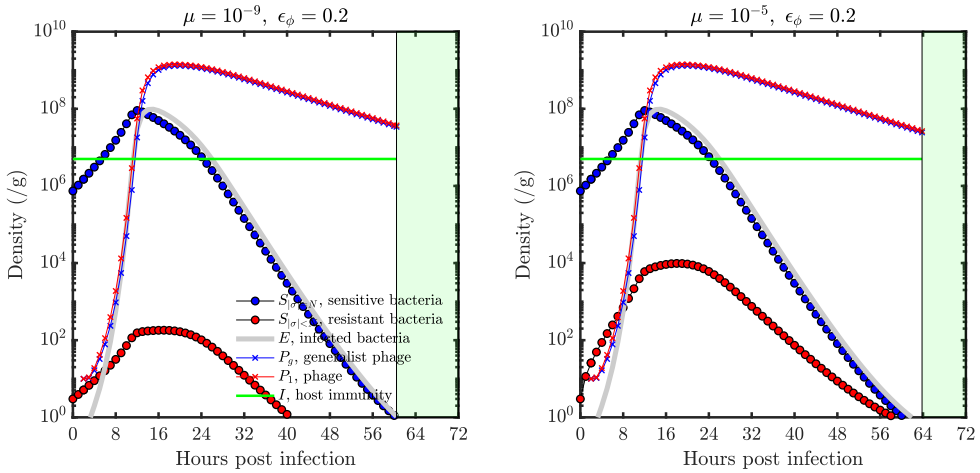

Figure 3.7: Comparison of time series of population densities with different mutation probabilities. (Left) Bacteria is eliminated around 60 hrs post infection in the case of low mutation probability. (Right) Bacteria is eliminated around 62 hrs post infection in the case of high mutation probability. See model parameters in Table 3.1.

higher phage dosage? The answer is No. In Fig. 3.8, we present two *in silico* experiments, one with high dosage treatment and the other one with low dosage treatment, low dosage treatment is curative while the high dosage treatment cannot eliminate bacteria. The bacteria and phage populations exhibit predator-prey oscillations. The phage drive the system to some lower level so that the bacteria is eventually eliminated with the aid of the immune response. The phage and innate immune response thus works in synergy to eliminate the bacteria. This synergistic effect is caused by a reduction of the bacterial population by phage below a desired level (which could be determined numerically as a function of model parameters), where the bacteria could be controlled by the innate immune response alone. Therefore, optimizing the use of multiphage 'cocktails' for treatment of immunodeficient hosts may not necessarily coincide with increasing to a higher dosage, the 'landing spot' (*i.e.,* initial state) in the transient prey-predator cycle plays a critical role. As shown in Fig. 3.8, the landing state on the phase plane for low dosage treatment initially follows the prey-predator oscillatory dynamics (large amplitude for the first cycle), then reaches

the regime (lower bacterial density) that can be eliminated by immune response. In contrast, the landing state on the phase plane for high dosage treatment drives small-amplitude prey-predator oscillations that cannot reach the space that can be eliminated by immune response. Note that the phase trajectories in Fig. 3.8 only present the transient ecological dynamics of susceptible bacteria, phage and innate immune response. On the other hand note that, due to the smaller amplitude oscillations, the "failing" high dosage treatment yields much lower concentrations of bacteria than the low dosage one. If bacteria don't go extinct, the fully resistant bacteria would be selected for by phage and become predominant over longer timescales dictated by mutation probability (μ) and phage numbers, which is why all treatments fail at high mutation probability (μ).

In summary, we found that the 8 by 4 infection networks with a generalist phage can also avert the failure in generic 8 by 3 infection networks. If the generalist cost is relatively low it seems to be favorable to use the one with generalist phage instead of the contingent specialist (much lower total dosages are needed, contrast Fig. 3.3 to Fig. 3.6) given the current model parameters. We caution that care must be taken regarding the the landing spot on virus-host phase plane.

3.5 Discussion

In this chapter, we proposed an eco-evolutionary synergy model and developed an optimization framework (initial condition optimization problem) to optimize the initial multiphage cocktail (delivered at beginning of treatment) for treating bacterial infections in immunodeficient hosts, coping with the risk of bacteria developing multi-resistance to the injected phage. By making a reasonable assumption on composition of symmetric phage dosage, we reduced the optimization problem (only two variables) and proposed a customized adaptive grid search algorithm to numerically solve it.

Our results provide important insights to guide the phage therapy in complex eco-evolutionary dynamics. We study a situation in which a cocktail with three phage alone

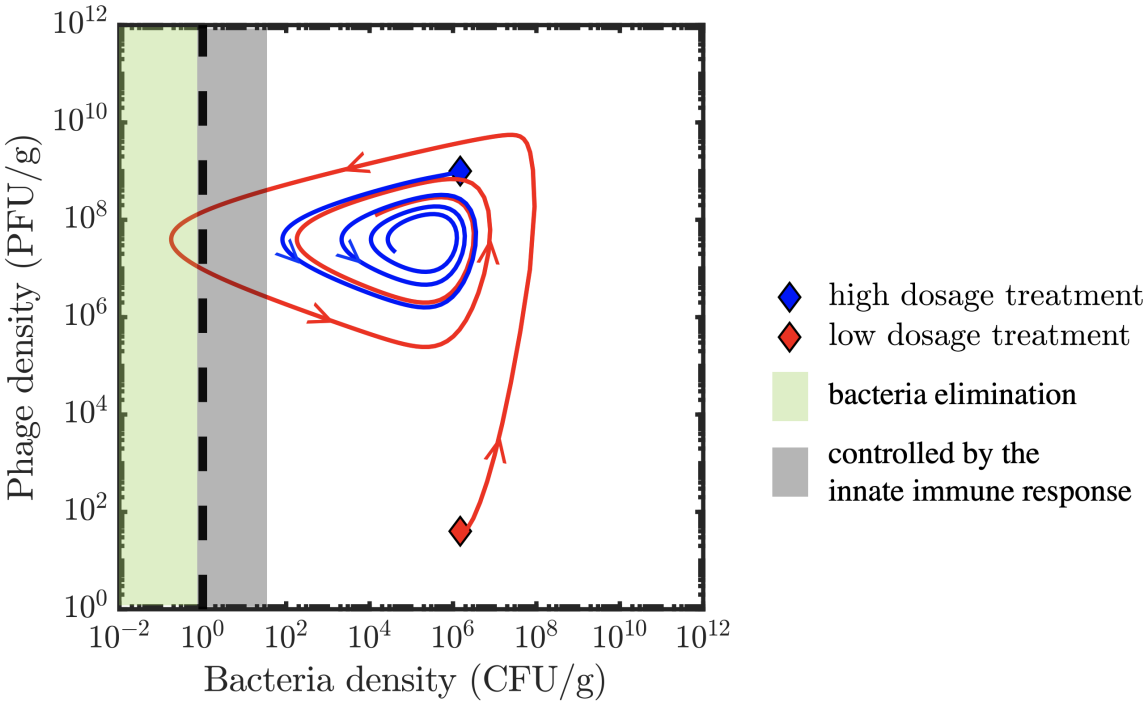

Figure 3.8: Comparison of phase portraits (projected on total bacteria - total phage plane) for high and low dosage treatments. The cost of generalist phage ϵ_ϕ is 0.2 and the mutation probability μ is 10^{-9}. Blue line is the phase trajectory when initial phage dosage is high while red line is the trajectory when initial phage dosage is low. The blue and red diamonds are corresponding initial state of two treatments. The vertical dotted line marks the position of bacteria elimination (threshold), the bacteria extinction regime is colored in green. The trajectory of low dosage treatment hits the bacteria elimination threshold, so it's curative. The gray area serves as a cartoon to sketch the regime where bacteria can be cleared by innate immune response alone. Note that gray area is only drawn to demonstrate the concept. See model parameters in Table 3.1.

cannot clear the infection due to the interplay between ecological predator-prey cycles and evolution of multi-resistance. We then show that adding to this cocktail either a contingent specialist or a generalist phage we can restore therapeutic success over a wide range of bacterial mutation rates.

For the 8 by 4 infection networks with a contingent specialist phage, due to the effect of competitive release, we need high dosages of symmetric specialist phage to control the rapid growth of resistant bacterial. In some related works (for prostate cancer treatment), continuous adaptive therapeutic strategies are developed using a game-theoretic model, to

control the competitive release of pre-existing resistant tumor cells [99, 100].

For the 8 by 4 infection networks with a generalist phage, we have to carefully administrate phage, so that the landing state on bacteria-phage plane can be driven by the prey-predator oscillations and reach the regime that bacterial population can be cleared by a fixed level of innate immune response [68]. In addition, one needs to be cautious about a potential severe consequence of low dosage treatments: the large oscillation (dynamics of low dosage treatment) shown in Fig. 3.8 eventually can drive bacteria population towards extinction (below the elimination threshold), but dynamics may lift bacteria density to potentially perilously high levels (e.g., around 10^8 CFU/g, see Fig. 3.8). This is risky, as in practice, those levels represent potentially serious physiological risks to the host organism.

Note that a number of simplifying assumptions have been made in the proposed eco-evolutionary model and optimization framework. As mentioned above, in this model we assume that phage types are fixed and don't evolve, assuming that the emergence of counter-resistance by phage would be rare on typical infection timescales. In future it will be important to remove this assumption and consider a setting where bacteria and phage evolve unconstrained affecting each other diversities, but this goes beyond the purpose of the current study.

Throughout this Chapter, we utilized a set of parameters close to those found to be relevant in mouse lung infections [69]. In such condition, the infection can be cleared by the synergy between immune response and phage dynamics, unless phage-resistance arises early enough. But with low enough immune response bacteria would be able to coexist with phage even without evolving resistance, albeit at concentrations much lower than carrying capacity (see Fig. S3 in [69]).

Therefore in such conditions, we posit that therapeutic success would depend on finding the right "landing spot" in the predator-prey dynamics plane driving the initial bacterial population to extinction, rather than targeting possible resistant mutants with adequate phage, which would not be able to drive their target bacteria to extinction alone. It shall

be noted that even in this case over longer timescales (dictated by mutation rate and selection pressure) resistant phage would become predominant and complete resistance would doom any therapy to fail. This why in most situations our optimal dosages are relatively insensitive to the mutation rate, until we reach high enough μ where fully resistant bacteria emerge over the considered timescales and therapy is expected to fail.

Another important assumption in our study lies in the fact that we chose to optimize the phage dosage conditioned to bacterial elimination, regardless of the total bacterial concentrations emerging during the course of infection. High concentrations of bacteria could induce severe harm to the lungs leading to complications even after the infection is cleared. In future it will be important to consider other possibilities and compare the corresponding results. Considering explicitly the total number of bacteria, the optimization framework then would also have to avoid big oscillations and overshoots. This may affect some of our results, especially the considerations on the right 'landing spot' (see Fig. 3.8), as discussed above.

Finally, in the adopted optimization framework, we assume the phage dosages except newly added engineered phage (contingent specialist or generalist) are all equal in optimal treatment. We verified the local optimality condition for the optimal strategy profile presented in Fig. 3.3, see Appendix 3.6.3 for details. However, this assumption may not hold (in global optimality perspective) due to the complex nonlinear effects in system (3.2). If this assumption is relaxed, there will be $(N + 1)$ variables in optimization problem. The proposed adaptive grid search algorithm is not scalable (time complexity exponentially increases as N increases). To resolve this issue, we have to modify the previous approach to make optimization algorithm scalable, see Appendix 3.6.4 for details.

3.6 Appendix

3.6.1 Adaptive grid search

The optimization problem (3.11) can be numerically solved via an evolutionary algorithm (e.g. genetic algorithm). However, there are some special structures in this problem can not be efficiently utilized by evolutionary algorithms, see Algorithm 1 for details. For example, suppose $(\widetilde{P}_c(t_0), \widetilde{P}_1(t_0))$ is feasible, then the optimal solution can not be found in $\{(x, y) \mid x > \widetilde{P}_c(t_0),\ y > \widetilde{P}_1(t_0)\}$.

3.6.2 Testing optimised treatment in the hybrid system

Note that system (3.2) is a mean-field model, which is justified by the large sizes of bacterial and phage populations. However, the *demographic stochasticity* is crucial to some 'reaction events', e.g. mutations. Here, we follow a similar hybrid stochastic-deterministic simulation protocol as the one introduced in Figure S6 in [92]. We further consider the probability of avoiding accidental extinction. The per-capita birth and death rates of the small mutant population are nearly constant at initial phase of growth, then we can model the number of individuals of the mutant population as a standard birth-death process with constant birth rate λ_b and death rate λ_d. The probability that the small mutant population escapes stochastic extinction is $(\lambda_b - \lambda_d)/\lambda_b$ if $\lambda_b > \lambda_d$; otherwise zero, where λ_b and λ_d are the birth rate per capita and death rate per capita (see Appendix C in [101] for details).

We tested the optimal treatments solved from deterministic system in the hybrid stochastic-deterministic system with the variation in mutation probability (μ) and WT phage benefit (α_ϕ). As shown in Fig. 3.3, we can write the optimal treatment $\mathcal{P}^*$ (dosage of WT phage and new type phage) as a function of (μ, α_ϕ), namely $\mathcal{P}^*(\mu, \alpha_\phi)$. For each (μ, α_ϕ), we ran the the hybrid stochastic-deterministic system 100 times with initial treatment $\mathcal{P}^*(\mu, \alpha_\phi)$. Success ratio is defined as the number of experiments with bacteria elimination over the total number of experiments. We found that success ratio is always 100/100 (obtained by

Algorithm 1 Customized adaptive grid search

Initialize $\ell \leftarrow 0$, cost $\leftarrow \infty$ and $\varepsilon_p \leftarrow$ desired grid resolution
Initialize finite grids $\mathcal{G}_0^{(0)} \subset [0, P_{max}]$ and $\mathcal{G}_1^{(0)} \subset [0, P_{max}/N]$
$n_0 \leftarrow$ size of $\mathcal{G}_0^{(0)}$ and $n_1 \leftarrow$ size of $\mathcal{G}_1^{(0)}$
Compute grid resolution $\leftarrow$ (max interval length)/P_{max}
while grid resolution $> \varepsilon_p$ **do**
  for $i_0 \leftarrow 1$ to n_0 **do**
    for $i_1 \leftarrow 1$ to n_1 **do**
      $P_c(t_0) \leftarrow \mathcal{G}_0^{(\ell)}[i_0]$ and $P_1(t_0) \leftarrow \mathcal{G}_1^{(\ell)}[i_1]$
      if $(P_c(t_0), P_1(t_0))$ is feasible **then**
        if $\mathcal{J}(P_c(t_0), P_1(t_0)) <$ cost **then**
          cost $\leftarrow \mathcal{J}(P_c(t_0), P_1(t_0))$
          grid index $(a, b) \leftarrow (i_0, i_1)$
        end if
        $n_1 \leftarrow (i_1 - 1)$
        Break i_1 loop
      end if
    end for
    if $n_1 = 0$ **then**
      Break i_0 loop
    end if
  end for
  $\ell \leftarrow \ell + 1$
  Refine grids $\mathcal{G}_0^{(\ell)} \subset \left[\mathcal{G}_0^{(\ell-1)}[a-1], \mathcal{G}_0^{(\ell-1)}[a]\right]$ and $\mathcal{G}_1^{(\ell)} \subset \left[\mathcal{G}_1^{(\ell-1)}[b-1], \mathcal{G}_1^{(\ell-1)}[b]\right]$
  $n_0 \leftarrow$ size of $\mathcal{G}_0^{(\ell)}$ and $n_1 \leftarrow$ size of $\mathcal{G}_1^{(\ell)}$
  Compute grid resolution $\leftarrow$ (max interval length)/P_{max}
end while
if cost $< \infty$ **then**
  Return searched grid $\left(\mathcal{G}_0^{(\ell)}[a],\ \mathcal{G}_1^{(\ell)}[b]\right)$
else
  Print no solution
end if

running hybrid stochastic-deterministic simulations) if $\mathcal{P}^*(\mu, \alpha_\phi)$ is a curative treatment in deterministic system, and success ratio is always 0/100 otherwise. This 'trivial' result suggested that the robustness of our optimal treatments (obtained from deterministic system) is guaranteed in the proposed hybrid stochastic-deterministic system. However, the robustness may not be guaranteed for fully stochastic simulation (worth to explore in future study).

3.6.3 Verification of optimization variable assumption

In Fig. 3.3, we write the optimal treatment $\mathcal{P}^*$ (dosage of contingent specialist phage and symmetric specialist phage) as a function of (μ, α_ϕ), namely $\mathcal{P}^*(\mu, \alpha_\phi)$. In our model, we let $N = 3$, then $\mathcal{P}^* = [P_i^*(t_0), P_1^*(t_0), P_1^*(t_0), P_1^*(t_0)]$, where $i \in \{c, g\}$. To test its local optimality, we generate a uniform random vector, $Z = [Z_i, Z_1, Z_2, Z_3]$, where $Z_i, Z_1, Z_2, Z_3 \sim U(-1, 1)$ *i.i.d.* Then, the locally perturbed treatment is given by $P_Z = 10^Z \odot \mathcal{P}^*$, where $\odot$ represents the element-wise multiplication of vectors. Note that a sample P_Z will be rejected if $\|P_Z\|_1 > P_{max}$. Then, we test if perturbed treatment P_Z is curative. For each (μ, α_ϕ), we ran above procedure for 2×10^3 times. To demonstrate how the local perturbation test works, we present a case of $\mu = 10^{-6}$ and $\alpha_\phi = 10$. The optimal treatment with equal dosage assumption is given as $\mathcal{P}^*(10^{-6}, 10) = [10^6, 1.78 \times 10^8, 1.78 \times 10^8, 1.78 \times 10^8]$ PFU/g, the total dosage of this treatment is 5.34×10^8 PFU/g. As we can see from Fig. 3.9, there is no treatment with less total dosage (comparing to the optimum obtained under equal dosage assumption) that can eliminate bacterial population, which proved it's local optimality. We use the same procedure and verify the local optimality condition hold for all μ, α and infection networks present in this chapter ($\mathcal{M}^0, \mathcal{M}^c$ and $\mathcal{M}^g$).

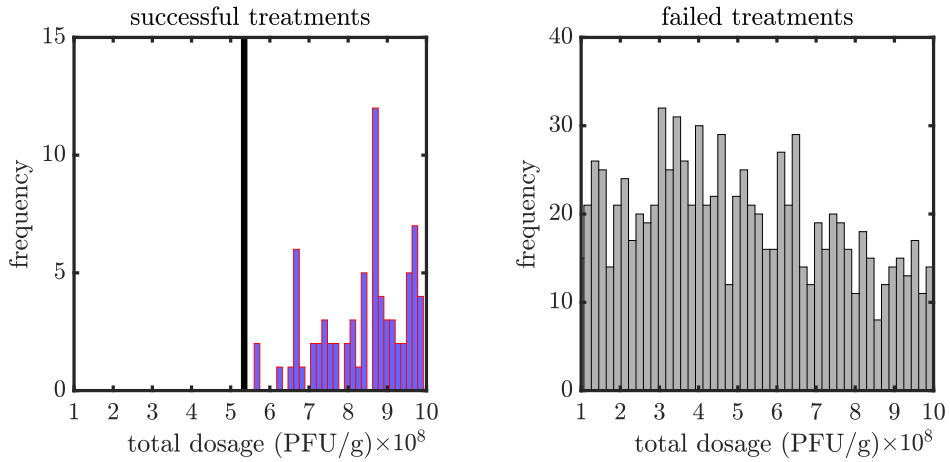

Figure 3.9: A demonstration of local perturbation test on dosage equal assumption when $\mu = 10^{-6}$ and $\alpha_\phi = 10$. (Left) Histogram of total dosage for successful treatments perturbed around optimal treatment $\mathcal{P}^*(10^{-6}, 10)$. All the successful treatments are with higher dosages than optimal treatment, all the samples are on the right side of a black vertical line (the total dosage of $\mathcal{P}^*(10^{-6}, 10)$). (Right) Histogram of total dosage for failed treatments perturbed around optimal treatment $\mathcal{P}^*(10^{-6}, 10)$.

3.6.4 Iterative projected gradient descent (PGD) method for a constrained initial condition optimization problem

We iteratively solve the following constrained initial condition optimization problem (3.12) to achieve the practical goal of eliminating bacteria with minimum dosage via a heuristic approach, see Algorithm 2.

Algorithm 2 Iterative PGD

Initialize left and right bounds: $L \leftarrow -2$ and $R \leftarrow \log(P_{max})$
Initialize $\varepsilon_p \leftarrow$ desired (log-scaled) precision
while $(R - L) > \varepsilon_p$ **do**
    Set total dosage upper bound $C \leftarrow 10^{(R+L)/2}$
    $\mathcal{P}_C^* \leftarrow$ optimal dosage by solving problem (3.12) with upper bound C (via PGD)
    if $\mathcal{P}_C^*$ is a curative treatment **then**
        $R \leftarrow (R + L)/2$
    else
        $L \leftarrow (R + L)/2$
    end if
end while

In this approach, we adaptively adjust the upper bound of constrain C and locate the

minimum value of C that results in bacterial elimination. For a fixed C, the optimization problem is

$$\min \mathcal{J}(P(t_0)) = \min \int_{t_0}^{t_f} \|S(t)\|_1 \, \mathrm{dt} \; + \; \|S(t_f)\|_1 \; , \text{ subject to } \|P(t_0)\|_1 \leq C. \quad (3.12)$$

We can numerically solve above constrained initial condition optimization problem (3.12) by projected gradient descent (PGD) method, the analytical expression of the derivative $d\mathcal{J}/dP(t_0)$ is derived in a more general form as following.

Consider the differential equation

$$\dot{x}(t) = f(x(t); x_0), \quad (3.13)$$

where $t \in [t_0, t_f]$, with initial condition $x(0) = x_0$, and define $\mathcal{J}$ by

$$\mathcal{J}(x_0) = \psi(x_0) + \int_{t_0}^{t_f} L(x(t)) \, dt + \phi(x(t_f)). \quad (3.14)$$

Here $x(t) \in \mathbb{R}^n$, $f : \mathbb{R}^n \to \mathbb{R}^n$, $L : \mathbb{R}^n \to \mathbb{R}$, $\phi : \mathbb{R}^n \to \mathbb{R}$, and $\psi : \mathbb{R}^n \to \mathbb{R}$. Considering $\mathcal{J}(x_0)$ as a function of x_0, then, we derive expression for the derivative $d\mathcal{J}/dx_0$ in terms of a costate. Denote $x(t)$ and $\widetilde{x}(t)$ as the corresponding state trajectory with initial state x_0 and $x_0 + \Delta x_0$ respectively, and $\Delta x(t) = \widetilde{x}(t) - x(t)$. Note that $x_0 + \Delta x_0$ is in a sufficiently small neighborhood of x_0. The first order difference in cost function is

$$\begin{aligned}
\Delta\mathcal{J} &= \mathcal{J}(x_0 + \Delta x_0) - \mathcal{J}(x_0) \\
&= \psi(x_0 + \Delta x_0) - \psi(x_0) + \int_{t_0}^{t_f} L(\widetilde{x}(t)) - L(x(t)) \, dt + \phi(\widetilde{x}(t_f)) - \phi(x(t_f)) \\
&= \frac{d\psi}{dx_0}(x_0)\Delta x_0 + \int_{t_0}^{t_f} \frac{dL}{dx}(x(t))\Delta x(t) \, dt + \frac{d\phi}{dx}(x(t_f))\Delta x(t_f) + \text{higher-order terms.}
\end{aligned} \quad (3.15)$$

The governing dynamics of difference term $\Delta x(t)$ is

$$\begin{aligned}\dot{\Delta x}(t) &= \dot{\tilde{x}}(t) - \dot{x}(t) \\ &= f(x(t) + \Delta x(t); x_0 + \Delta x_0) - f(x(t); x_0) \\ &= \underbrace{\frac{\partial f}{\partial x}(x(t); x_0)}_{n \times n} \underbrace{\Delta x(t)}_{n \times 1} + \text{higher-order terms},\end{aligned} \tag{3.16}$$

where initial condition is $\Delta x(t_0) = \Delta x_0$. Neglecting higher order terms and using the state-transition matrix $\Phi(t, \tau) \in \mathbb{R}^{n \times n}$, the solution is

$$\Delta x(t) = \Phi(t, t_0) \Delta x_0. \tag{3.17}$$

Then, we plug Eq. 3.17 in Eq. 3.15 to obtain (drop higher order terms),

$$\Delta \mathcal{J} = \frac{d\psi}{dx_0}(x_0) \Delta x_0 + \int_{t_0}^{t_f} \frac{dL}{dx}(x(t)) \Phi(t, t_0) \Delta x_0 dt \; + \frac{d\phi}{dx}(x(t_f)) \Phi(t_f, t_0) \Delta x_0. \tag{3.18}$$

Hence, the derivative (first-order variation) is

$$\frac{d\mathcal{J}}{dx_0} = \frac{d\psi}{dx_0}(x_0) + \int_{t_0}^{t_f} \frac{dL}{dx}(x(t)) \Phi(t, t_0) dt \; + \frac{d\phi}{dx}(x(t_f)) \Phi(t_f, t_0). \tag{3.19}$$

Define the costate $\lambda(\tau) \in \mathbb{R}^n$ as

$$\lambda^T(\tau) = \int_{\tau}^{t_f} \frac{dL}{dx}(x(t)) \Phi(t, \tau) \; dt + \frac{d\phi}{dx}(x(t_f)) \Phi(t_f, \tau). \tag{3.20}$$

Note that

$$\dot{\lambda^T}(\tau) = -\lambda^T(\tau) \frac{\partial f}{\partial x}(x(\tau); x_0) - \frac{dL}{dx}(x(\tau)), \tag{3.21}$$

with terminal condition $\lambda^T(t_f) = \frac{d\phi}{dx}(x(t_f))$. In doing so, we observe that Eq. 3.19 can be

written in terms of the initial condition of costate

$$\frac{d\mathcal{J}}{dx_0} = \frac{d\psi}{dx_0}(x_0) + \lambda^T(t_0). \tag{3.22}$$

Table 3.1: Parameters and initial conditions in the system (3.2)

Parameters	**Value**	**Source**
r_{max}, maximum growth rate	0.75 h^{-1}	[69]
r_{min}, minimum growth rate	0.5 h^{-1}	[69]
μ, probability of emergence of mutant per cellular division	$10^{-9} \sim 10^{-4}$	present
K_C, carrying capacity of bacteria (immunodeficient hosts)	8.5×10^{11} CFU/g	[69]
β, burst size of phage	100	[69]
w, decay rate of phage	0.07 h^{-1}	[69]
ϵ, killing rate parameter of immune response	8.2×10^{-8} g/(h cell)	[69]
α, maximum growth rate of immune response	0.97 h^{-1}	[69]
K_I, maximum capacity of immune response (no innate immune activation)	same as I_0	[69]
K_D, bacterial concentration at which immune response is half as effective	4.1×10^7 CFU/g	[69]
K_N, bacterial concentration when immune response growth rate is half its maximum	1.0×10^7 CFU/g	[69]
L, number of latent stages	2	present
τ_{inf}, mean infectious period	2 hs	present
ϕ, adsorption rate of phage	1.5×10^{-8} g/(h PFU)	present
α_ϕ, benefit of contingent specialist phage	$2 \sim 100$	present
ϵ_ϕ, cost of generalist phage	$0.1 \sim 0.9$	present
P_C, phage density at half saturation	1.5×10^7 PFU/g	[69]
$S_\sigma(0)$, initial (WT) bacterial density, immunodeficient hosts ($\|\sigma\|_1 = N$)	7.4×10^5 CFU/g	[69]
$S_\sigma(0)$, initial phage-resistant bacterial density ($\|\sigma\|_1 = N - 1$)	1 CFU/g	[69]
$S_\sigma(0)$, initial phage-resistant bacterial density ($\|\sigma\|_1 < N - 1$)	0 CFU/g	present
I_0, initial immune response (immunodeficient hosts)	5×10^6 cell/g	present
$P_j(0)$, initial phage density	0 PFU/g	[69]
P_{max}, maximal phage dosage	10^9 PFU/g	present

CHAPTER 4

DISEASE-DEPENDENT INTERACTION POLICIES TO SUPPORT HEALTH AND ECONOMIC OUTCOMES DURING THE COVID-19 EPIDEMIC

Adapted from:

Li, G., Shivam, S.*, Hochberg, M.E., Wardi, Y. and Weitz, J.S., 2020. Disease-dependent interaction policies to support health and economic outcomes during the COVID-19 epidemic. Available at SSRN 3709833.*

Weitz, J.S., Beckett, S.J., Coenen, A.R., Demory, D., Dominguez-Mirazo, M., Dushoff, J., Leung, C.Y., Li, G., Măgălie, A., Park, S.W., Rodriguez-Gonzalez, R., Shivam, S. and Zhao, C.Y., 2020. Modeling shield immunity to reduce COVID-19 epidemic spread. Nature medicine, 26(6), pp.849-854.

4.1 Introduction

Lockdowns and stay-at-home orders have partially mitigated the spread of COVID-19. However, *en masse* mitigation - applying to all individuals irrespective of disease status — has come with substantial socioeconomic costs. In this chapter we demonstrate how individualized policies based on disease status (e.g., susceptible, infectious, recovered/immune) can reduce transmission risk while minimizing impacts on economic outcomes. We design feedback control policies informed by optimal control solutions to modulate interaction rates of susceptible and immune individuals based on estimates of the epidemic state. We identify personalized interaction rates such that recovered/immune individuals elevate their interactions and susceptible individuals remain at home before returning to pre-lockdown levels. As we show, feedback control policies can yield mitigation policies with similar population-wide infection rates to total shutdown but with significantly lower economic costs and with greater robustness to uncertainty compared

to optimal control policies. The switching policy enables susceptible individuals to return to work when recovered/immune levels are sufficiently higher than circulating incidence. Our analysis shows that test-driven improvements in isolation efficiency of infectious individuals can inform disease-dependent interaction policies that mitigate transmission while enhancing the return of individuals to pre-pandemic economic activity.

4.2 Results

4.2.1 Optimal control framework for state-dependent contact rates policies that balance public health and socioeconomic costs

We develop an optimal control framework to identify policies that address the tension between decreasing contacts (that reduce new infections) with increasing contacts (that are linked to socio-economic benefits). We represent the epidemic using a Susceptible-Exposed-Infectious-Recovered (SEIR) nonlinear dynamic model (see Sect. 4.4.1 for complete details; see Fig. 4.1). In doing so, the force of infection is influenced by state-specific contact rates $c_S,\ c_E,\ c_I$ and c_R for susceptible, exposed, infectious and recovered/immune individuals, respectively - these different levels form the basis for a control policy that directs individuals to interact at different levels depending on their test status.

In the optimal control framework, a set of state-specific contact rates are identified that minimize the appropriately weighted sum of what we term 'public health' and 'socioeconomic' costs. Public health costs are quantified both by average infected levels and cumulative deaths. Socioeconomic costs are quantified in terms of reductions in the total rate of interactions and by shifts in state-specific contact rates. The optimal control 'solution' is then a time-dependent set of disease-specific rates which are both shaped by and shape the epidemic itself (see Sect. 4.4.3 for details on the gradient projection algorithm used to identify the solution). Note that we constrain the contact rate of exposed individuals to be equal to that of susceptible individuals given the challenges of timely identification of exposed individuals who are not yet infectious (and presumably have insufficient viral titer

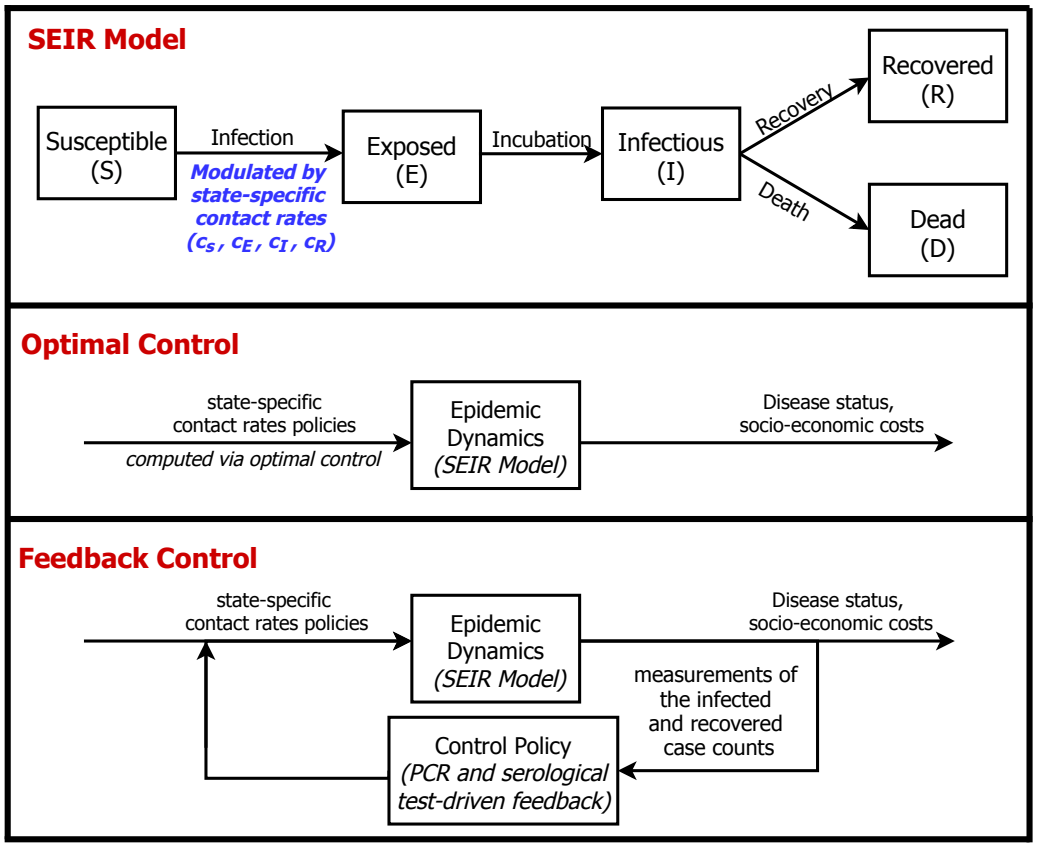

Figure 4.1: Epidemic dynamics with optimal and feedback control of disease-status driven contact rates. (Top) SEIR model schematic in which the force of infection is modulated by state-specific contact rates, see text and Sect. 4.4 for details. (Middle) Diagram of optimal control approach: contact rates are pre-specified given model structure and estimate of parameters and current conditions. (Bottom) Diagram of feedback control approach: contact rates are updated in real-time based on measurements of the infected and recovered/immune case counts via testing surveillance.

to be identified using screening tests; an issue we return to in the Discussion). Finally, we utilize the parameter ξ to regulate the relative importance of costs associated with death and spread of infection vs. socioeconomic impact.

Figure 4.2 shows the results of comparing a baseline outbreak (*i.e.,* neglecting public health costs, given weighting parameter $\xi = 0$) to a full lockdown scenario (*i.e.,* neglecting socioeconomic costs with 75% isolation for all, $\xi \gg 1$) and a balanced scenario with optimized contact-rates (*i.e.,* corresponding to $\xi \sim 1$). At the time intervention starts (without any intervention in first 60 days), the outbreak has an ongoing incidence of 19 (per 100,000)

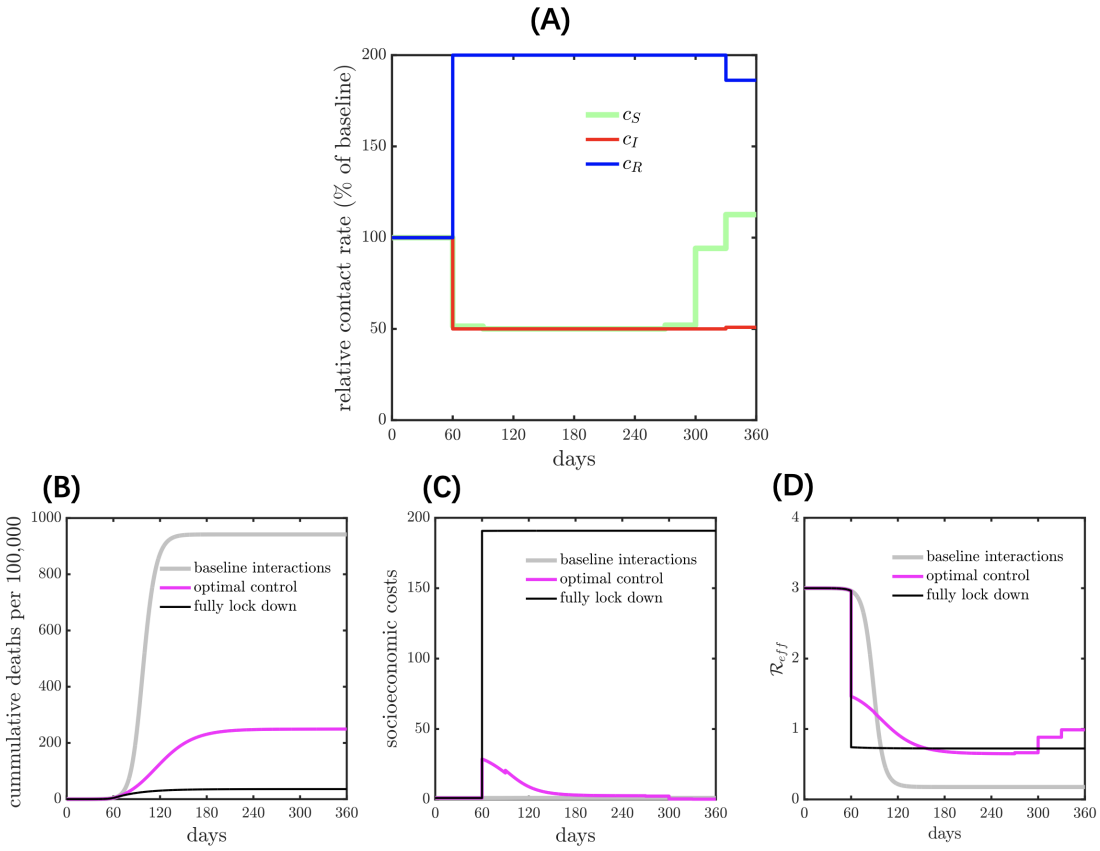

Figure 4.2: Comparison of health and economic outcomes of COVID-19 given various interventions: baseline interactions (*i.e.,* no intervention); optimal contact rate intervention (balance both health and economic outcomes) and fully lock down intervention (applied to all the subpopulations) with 75% isolation efficiency. (A) The optimal contact rate relative to the baseline contact rate (denoted as 100%) with 50% isolation effectiveness and shield immunity level 2. (B) Cumulative deaths (health outcome) during the epidemic. (C) Socio-economic costs (economic outcome) during the epidemic. (D) Measure of effective reproduction number ($\mathcal{R}_{eff}$) for different interventions during the epidemic.

per day, prevalence of 0.4%, and a cumulative infection level of 0.8%. As shown in Figure 4.2, in the baseline scenario, the disease spreads through the population leading to 94% cumulative infection (as expected given strength-size relationships for $\mathcal{R}_0 = 3$). In contrast, a full lockdown scenario with 75% reduction in contact rates of all individuals after 60 days leads to a total outbreak size of 4% of the population. The optimal control solution in the balanced case $\xi = 1$ reveals a potential route to jointly address public health and socioeconomic cost. From the perspective of public health, the optimal control solution leads to

25% cumulative infections. In addition, the socioeconomic costs in the optimal control case are higher in the short-term but approach that of the baseline scenario in the long-term. Indeed, the effective reproduction number identified via an optimal control framework in the balanced scenario gradually reduces to sub-critical levels (close to an effective reproduction number, $\mathcal{R}_{eff} = 0.75$) while gradually relaxing controls over time. The optimal control solutions are shown in Figure 4.2A. The optimal control solutions differ based on disease status, recovered/immune individuals elevate their interactions, infectious individuals isolate, and susceptible individuals lock-down before gradually returning to pre-lockdown levels.

4.2.2 Personalized, test-based optimal control policies and their impact on public health and socioeconomic outcomes.

In order to explore the mechanisms identified by the optimal control framework, we systematically modulate the effectiveness of isolation and evaluate its effect on the state-dependent optimal contact rates and disease dynamics. In practice, isolation effectiveness is influenced by availability, accuracy, and speed of testing as well as fundamental limitations on an individual's ability to isolate (which can vary with socioeconomic and other factors). Figures 4.3A-C evaluate low, medium, and high efficiency of isolation spanning 25%, 50% and 75% reduction in the contact rates of infected individuals, respectively. As is evident, the optimal control solutions for state-dependent contact rates vary significantly with isolation effectiveness; suggesting that COVID-19 response policies that can vary with disease status may open up new possibilities to balance public health and socioeconomic outcomes.

First, in the low (25%) or medium (50%) effectiveness cases, susceptible, exposed, and infectious individuals adopt the maximal level of isolation. Inefficient isolation of infectious individuals elevates risks of new transmission that are not outweighed by socioeconomic benefits. Notably, the optimal control solution includes an elevated level of interaction by recovered/immune individuals. This finding recapitulates 'shield immunity'

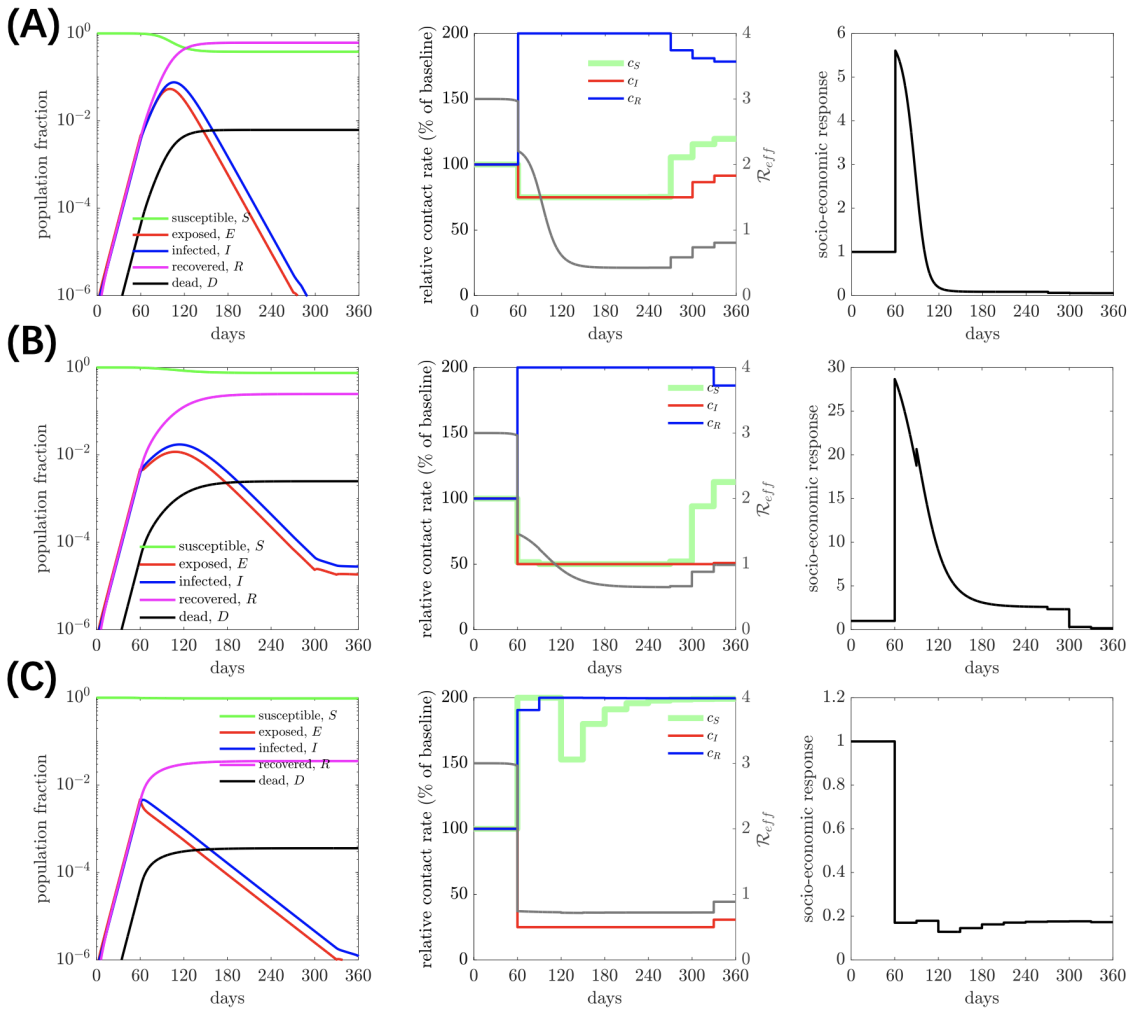

Figure 4.3: SEIR dynamics with contact rate interventions for various isolation efficiencies, (A) 25% isolation efficiency; (B) 50% isolation efficiency and (C) 75% isolation efficiency. The relative importance (ξ) is 1 for all the cases (A), (B) and (C). The contact rate interventions start at 60 days, people follow baseline (or normal) interactions before that. For all the isolation efficiency scenarios (three rows), the left panel shows the population dynamics given the optimal contact rate (related to the baseline contact rate, with 100% as baseline) shown in the middle panel. The gray curve in the middle panel represents the measure of corresponding effective reproduction number ($\mathcal{R}_{eff}$). The right panel shows the corresponding socio-economic costs. See Sect. 4.4 for additional scenarios.

[102, 61], insofar as recovered/immune individuals are protected from re-infection over the course of the intervention. The elevated contacts of recovered/immune individuals have multiple effects: both diluting interactions by susceptibles (and reducing transmission risk) and by increasing socioeconomic activity. In contrast, for sufficiently high levels of isola-

tion efficiency (75%), the optimal control solutions suggest there is no need for a general lockdown. Instead, the combination of infected case isolation and shielding by the subpopulation of recovered/immune individuals is sufficient to rapidly reduce and contain $\mathcal{R}_{eff}$ below 1, leading to a decreasing number of new infections. We note that irrespective of isolation effectiveness, balancing public health and economic outcomes drives $\mathcal{R}_{eff}$ below 1, but not necessarily to 0 (albeit, given the constraints imposed by lockdown efficiency, such an extreme reduction may not even be possible), and eventually increased immunity permits an easing-off in restrictions yielding an increase in $\mathcal{R}_{eff}$ [103].

4.2.3 Sensitivity of optimal control approach to mis-timed implementation of policies

Despite its potential to balance public health and socioeconomic costs, a central drawback of optimal control solutions is the potential exponential growth of errors. Given the fact the COVID-19 dynamics are only partially observed (with significant uncertainty in the actual state), application of a policy requires an estimate of the time since epidemic initiation, what we term 'epidemic age'. In order to evaluate the sensitivity of optimal control policies due to mis-timing, we first computed the optimal control policy for a system one month after an outbreak. However, instead of implementing the policy matched to the actual epidemic age, we enforce the optimal control policy 30 days later, *i.e.,* at the end of 60 days after the start of the outbreak. Figure 4.12 shows the difference in the mis-timed control policy vs. the optimal control policy; as is evident the mistimed policy relaxes stringent lockdown when the optimal policy continues to lock-down. As a consequence the total deaths are far higher for 25% and 50% isolation efficiency (see Table 4.1). The mistimed policy, in effect, biases the system towards minimizing socioeconomic rather than public health costs. This significant difference in performance metrics demonstrates the potential shortcomings of implementing a policy based on optimal control. However we note that with a stringent isolation efficiency, delays are less problematic. The reason is that with efficient infected case isolation, both the mis-timed and optimal control policy could enable

Optimal Control	Without Delay		With Delay	
Isolation Efficiency (shielding = 2)	Deaths (per 10,000)	Working Fraction	Total Deaths (per 10,000)	Working Fraction
25%	600	90.95%	720	94.96%
50%	250	67.13%	510	83.65%
75%	40	99.92%	40	99.95%

Table 4.1: Comparison between optimal control approach for contact policy with and without delay. The comparisons are made for isolation efficiencies of 25%, 50% and 75%, with performance metrics of total deaths and working fraction. The total death is significantly higher for the system with delay when the isolation efficiency is 25% and 50%, suggesting poor robustness of the computed optimal control to input-delay.

nearly all individuals to work, given that $\mathcal{R}_{eff}$ is held below 1 by infection isolation on its own.

Despite its fragility, we identify common features of the optimal control policy given variation in the effectiveness of infectious case isolation. First, the optimal control policy minimizes infected contact rates. The optimal control solutions also robustly identify an immune shielding strategy such that recovered/immune individuals elevate their interactions to the maximum possible relative to baseline. Importantly, differences in the optimal control policy are primarily centered on identifying a switch point in contact rate level for the susceptible population. From Figures 4.9, 4.10 and 4.11, we observe the switch point as a function of time, showing that irrespective of isolated case effectiveness and shield immunity constraints, the increase in susceptible contact rates happens later in the lockdown period. Switch over points correspond to times when the infection prevalence is relatively low compared to the recovered/immune population. This observation provides the basis for a feedback, rather than optimal, control policy.

4.2.4 Feedback-control policy for balancing public health and socioeconomic costs

We propose the use of a feedback control policy adapted from emergent features of the optimal control policy solutions: (i) infectious individuals isolate as far as is possible; (ii) recovered/immune individuals increase their activities as much as possible, *i.e.,* akin to shield

Feedback Control	Without Delay		With Delay	
Isolation Efficiency (shielding = 2)	Deaths (per 10,000)	Working Fraction	Total Deaths (per 10,000)	Working Fraction
25%	620	89.98%	620	89.94%
50%	250	62.40%	250	62.12%
75%	30	99.90%	30	99.90%

Table 4.2: Comparison between feedback control approach for contact policy with and without delay. Isolation efficiencies of 25%, 50% and 75% are used for the purpose of comparison, with performance metrics of total deaths and working fraction. Both of the performance metrics are nearly identical for all cases, which suggests high robustness to delay on the system.

immunity. Hence, we set out to identify a system-dependent change in the contact rate of susceptible individuals, separating lockdowns vs. return-to-work. In practice, we identify a critical curve in $I - R$ plane (*i.e.,* infected-recovered cases plane) via a genetic algorithm, such that the recommended behavior of susceptible individuals is dictated by surveillance-based estimates of infectious and recovered/immune individuals (see Sect. 4.4.5 for more details).

Figure 4.4 summarizes the results of the feedback control policy. From a policy perspective, the feedback control policy identifies a switch between lock-down and return-to-work when there are significantly more recovered/immune individuals than infectious individuals. The timing of the return from lockdowns is accelerated given increases in isolation efficiency (rows) with additional benefits from the implementation of shield immunity (columns). Typically, the transition between lockdown and re-openings occur when circulating case levels are low relative to recovered/immune individuals. The critical ratio of recovered to infectious individuals decreases as isolation increases. Notably when there are sufficiently high levels of isolation of infectious individuals then the optimal feedback policy suggests that no lockdown is required (note the entirely 'white' regions in the bottom row). In the Discussion we provide additional context on the potential impacts of vaccination on this central finding.

Critically, the performance of the test-driven feedback policy is nearly identical for the

performance metrics with or without mis-timing (see Table 4.2). This finding implies that state-based approaches will be less likely to have exponentially mis-timed applications, and reinforces the need for population-scale testing for both active infections and recovered/immune individuals. To examine the robustness of the feedback strategy in terms of model mis-specification, we consider three cases in which the isolation efficiency is unbiased, overestimated (by $\sim 10\%$) and underestimated (by $\sim 10\%$) relative to the true value. We then compare the total deaths and working fraction of a feedback strategy based on these (potentially incorrect) estimates of the isolation efficiency. We find that the feedback strategy is robust to such mis-specification, particularly when isolation efficiency is high or low (see SI Figure S10 for details). We also note that a simple policy with only two states - 'lockdown' and 'open', respectively, corresponding to minimum and baseline contact rates for the susceptible cases, would be easier to implement than one with continuous 'phases' or state changes. In Figure 4.13, we document the generalizability of results given variation in infected case isolation and the level of shield immunity.

The results presented in Chapter 4 so far are accepted for iScience journal publication, a pre-print is available at [60].

4.2.5 Optimised age-dependent immune shielding deployment

In this section, we apply an age-structured model to explore the outcome of having the shields act in positions where they could be more or less likely to interact with different age groups. For simplicity, we ignore births and other causes of death. We consider a population of susceptible (S), exposed (E), infectious asymptomatically (I_a), infectious symptomatically (I_s) and recovered (R) who are free to move without restrictions in a 'business as usual' scenario. A subset of symptomatic cases will require hospital care, which we further divide into subacute (I_{hsub}) and critical and/or acute (requiring intensive care unit (ICU) intervention, I_{hcri}) cases. We assume that a substantial fraction of critical cases will die. Age-stratified risk of hospitalization and acute cases are adapted from the

values from [57], which models potential outcomes in the United Kingdom and the United States. The rate of transmission is reduced by a factor of $1/(N_{tot} + \alpha R_{shields})$ where N_{tot} denotes the fraction of the population in the circulating baseline, and $R_{shields}$ denotes the total number of recovered individuals between the ages of 20 and 60 years (a subset of the total recovered population). In this model, we assume that all recovered individuals have immunity, but that only a subset are able to facilitate interaction substitutions. The model assumes that the individuals in the circulating pool are not interacting with hospitalized patients. Interactions with patients in the hospital setting need to be incorporated into specific implementation scenarios with healthcare workers [104]. The baseline epidemiological parameters, age-stratified risk and population structure are provided in Sect. 4.4.7.

Fig. 4.5 shows that an improved way of distributing shielding effort is to prioritize low, but non-zero, shielding of young and place increasing effort on shielding elderly members of the population (see Fig. 4.6 for shielding concentrations). Using the optimized shielding deployment, the reduction in deaths ($D_{tot}(t_f)$) is substantial ($\sim 30\%$). The results suggest advantages of preferentially shielding those who are most at risk.

The results presented in Chapter 4.2.5 are published [61].

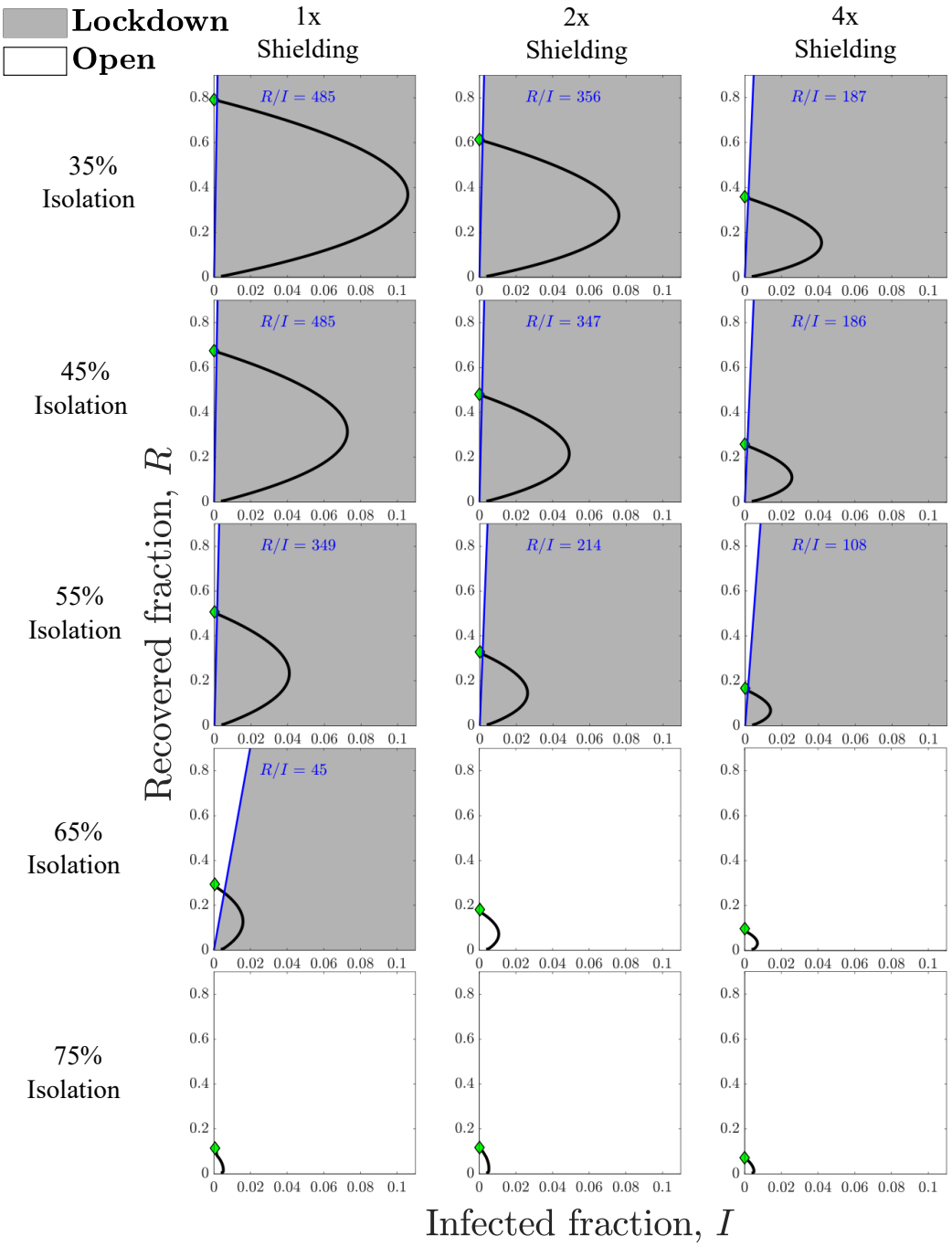

Figure 4.4: Heuristic state feedback intervention policies varying with isolation efficiency (rows) and shielding levels (columns). In each panel, the trajectory is noted in black with the final state as green diamond. An optimal line divides the plane into two regions which determines the optimal contact rate for the susceptible population for the current infected and recovered cases. The optimal policy in the dark grey region is lockdown and open in the white region. The phase plots show the dynamics of the infected and recovered case fractions over the period of 360 days, while applying the control strategy described above in the absence of shielding and for shielding levels of 2 and 4 respectively. For the case of isolation efficiency of 75%, no lockdown is needed at all for the susceptible population.

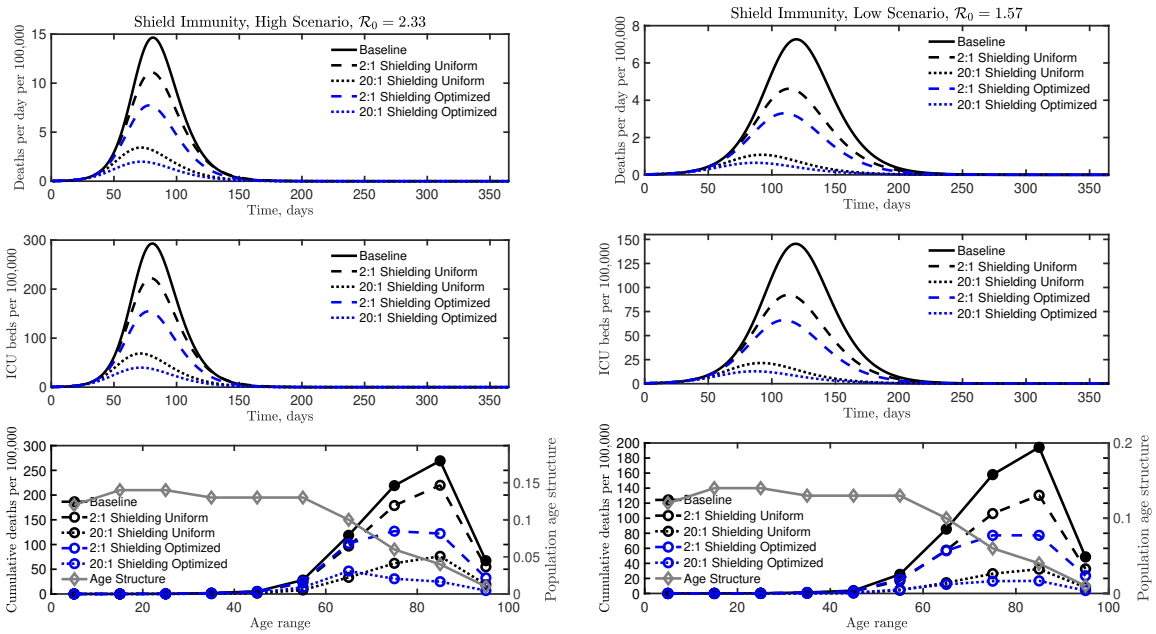

Figure 4.5: COVID-19 dynamics in the two shielding scenarios ($\alpha = 2$ and $\alpha = 20$), compared to the scenarios with optimized age dependent shield deployment for the same values of α with the baseline case included for reference. The results are displayed for both high (left) and low (right) R_0 scenarios. The optimal deployment significantly reduces the total death count and the need for ICU beds for both $\alpha = 2$ and $\alpha = 20$.

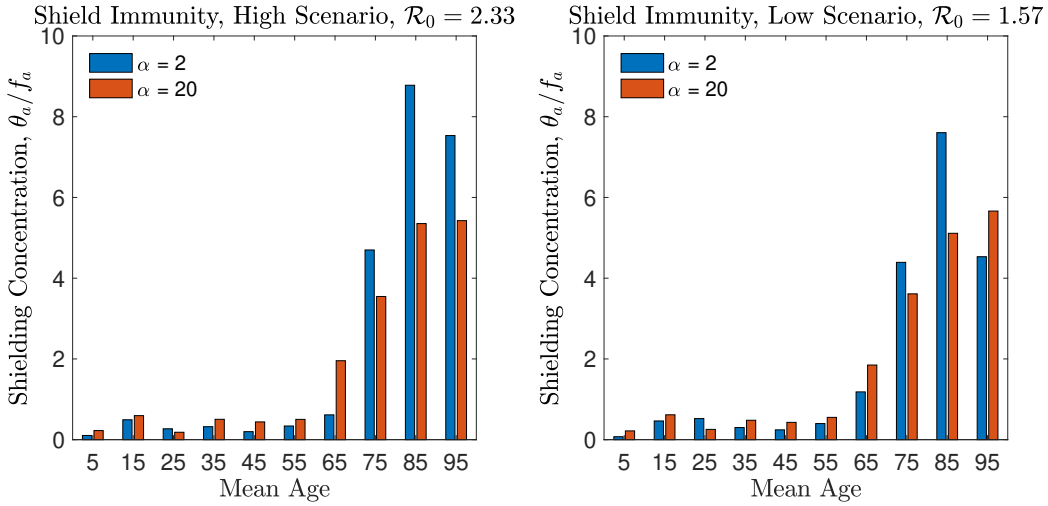

Figure 4.6: Optimal shielding concentration for all age classes for high (left) and low (right) $\mathcal{R}_0$ scenarios. The optimal shielding concentrations (for both scenarios) are obtained via solving an optimization problem with low and high shielding levels (see Methods). The optimal shielding concentration (θ_a / f_a) is larger for classes with a higher age, which would reduce casualties as the older population is disproportionately affected by COVID-19.

4.3 Discussion

We have developed a linked series of optimal- and feedback-control analyses to evaluate the effectiveness (and benefits) of modifying contact rates for managing the COVID-19 pandemic from both health and economic perspectives. Throughout, our central goal was to optimize the interactions between individuals based on disease status so as to achieve a defined balance between public health and economic outcomes. By explicitly incorporating contact rates as the control variables in a SEIR model, we were able to identify optimal control policies that could, in theory, significantly reduce expected infections (and fatalities) while reducing the negative socioeconomic costs of sustained lockdowns. Optimal control policies are unlikely to be applied in practice, given the potential exponential misspecification of policies over time. Hence, we leveraged insights from the optimal control solutions to guide a feedback control approach that performs nearly as well as the optimal control approach with significant improvements in robustness given uncertainty in estimating the epidemic state. Collectively, our control policies indicate that infected individuals should be isolated (as effectively as possible), recovered/immune individuals should be encouraged to return to work (given benefits accrued via shield immunity), while the release of other individuals from lock-down should be guided by the epidemic state. The transition from lock-down to return-to-work occurs when circulating case-loads are far lower than recovered case counts; with the scope of the epidemic sharply controlled by infection case isolation. A combination of policies, e.g., mask-wearing, physical distancing, will help to reduce transmission risk for individuals who do return to work.

The SEIR framework used as the basis for the present control study is intentionally simplified. The epidemic model does not account for process or observational noise, analytic test features, heterogeneity, stratified risk, asymptomatic cases, and detailed elaboration of severe cases. By reducing the model complexity, we have tried to shed light on the general problem of balancing public health with socioeconomic outcomes. In doing so,

we have highlighted a middle ground between dichotomous outcomes that focus on public health or socioeconomic costs solely. We recognize that extensions and applications of the present work will require consideration of additional epidemic complexities (e.g., asymptomatic transmission) and additional evaluation of joint public health and economic costs (e.g., arising from hospitalization burden). Translating the present findings into practical use will also require improved assessments of the ways in which behavior is influenced by awareness and communication of the pandemic state, in addition to the influences of formal implementation of policy campaigns [105, 106].

A salient point that emerged from the control analysis is the benefit of reducing interactions by infectious individuals and increasing interactions by recovered/immune individuals. In doing so, it is critical to note that the conception of the model preceded the availability of vaccines. The increase of activity by recovered/immune individuals effectively dilutes risky contacts between susceptible and infectious individuals. We contend that this principle of shield immunity is also relevant when individuals are vaccinated, and therefore move from susceptible directly to the recovered/immune category. Increases in vaccination may provide opportunities to reduce risk for susceptible individuals, beyond benefits accrued by susceptible depletion alone. We recognize that adopting policies that include individual disease status are likely to raise both privacy and ethical concerns [107, 108]. Yet, given the slow rate of vaccine dissemination, we suggest that the absence of action-taking that could increase protection to those yet to be vaccinated also comes at a public health and socioeconomic cost. Even now, more than a year after the identification of the first SARS-CoV-2 case, we remain closer to the beginning than the end of the COVID-19 pandemic. As we have shown, accelerating the slow-down of transmission while restoring economic activity may be enabled by both personalized, test-driven, policies as the basis for mitigation that reduce risk for all.

4.4 Methods

4.4.1 Model and parameters

The epidemic model analyzed here is an 'SEIR' model, including SEIR dynamics [109], susceptibles S, exposed E, infectious I, recovered R , with the total number of fatalities denoted by D. The *force of infection* is the contact rate of infectious individuals multiplied by the probability that the interaction is with a susceptible person multiplied by the probability that the event leads to an infection. Let c_S, c_E, c_I and c_R equal the contact rate of S, E, I, and R individuals respectively. Although such different rates imply the existence of an implicit contact matrix, we are only focused on infection dynamics associated with a single epidemiological birth state, such that the force of infection can be represented by a single term, $F(S, E, I, R; c)$. The force of infection is

$$F(S, E, I, R; c) = \eta_I c_I \left(\frac{c_S S}{c_S S + c_E E + c_I I + c_R R} \right), \tag{4.1}$$

where η_I is the measure of disease transmission effectiveness from I class to S class [110]. Suppose all the contact rates are equal to a baseline contact rate c_B. Assuming relatively few fatalities per-capita, then the total population is approximately constant at N, such that the force of infection can be approximated as $F \approx \eta_I c_B (S/N)$, which recovers the standard SEIR model by defining $\beta = \eta c_B$ as *infection rate*. In the generalized case, the model is

given by the following system of nonlinear differential equations

$$\begin{aligned}
\frac{dS}{dt} &= -F(S,E,I,R;c)I \\
\frac{dE}{dt} &= F(S,E,I,R;c)I - \frac{1}{T_E}E \\
\frac{dI}{dt} &= \frac{1}{T_E}E - \frac{1}{T_I}I \\
\frac{dR}{dt} &= (1-\mu)\frac{1}{T_I}I \\
\frac{dD}{dt} &= \mu\frac{1}{T_I}I,
\end{aligned} \tag{4.2}$$

where $F(S,E,I,R;c)$ is the force of infection given in Eq. 4.1, and T_I is the infectious period, T_E is the incubation period, μ is the case fatality ratio for infected individuals, see SEIR model schematic in Fig. 4.7. At the start of an outbreak ($t = 0$), the contact rate of

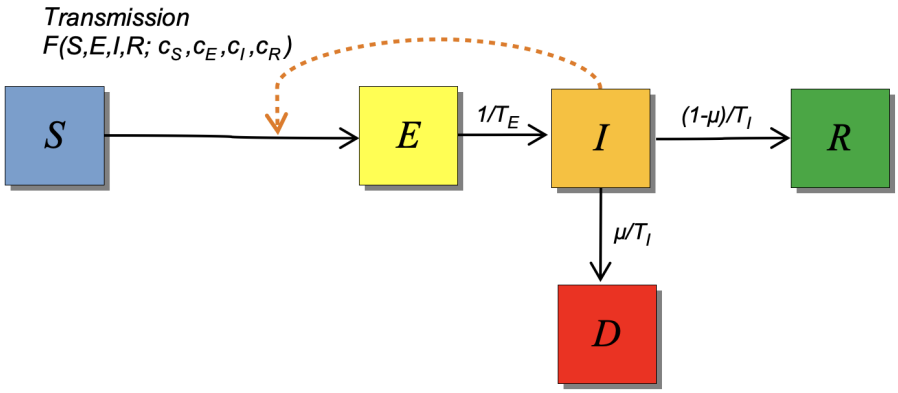

Figure 4.7: SEIR Model Schematic. The interactions between susceptible and infected individuals lead to newly exposed cases. These interactions are modeled by the force of infection $F(S,E,I,R;c)$. The exposed individuals undergo an incubation period (T_E) before the onset of infectiousness. Infectious individuals will either recover (and develop protective immunity) or die after an infectious period (T_I), see model equations in Eq. 4.2.

each individual is c_B. The basic reproduction number $\mathcal{R}_0$ of this compartmental model is

$$\mathcal{R}_0 = \overbrace{T_I}^{\text{average infectious time}} \times \overbrace{\eta_I c_B}^{\text{infection rate}} . \tag{4.3}$$

The initial exponential growth rate (r) of the epidemic spread is given by the largest eigenvalue of the Jacobian matrix evaluated around the disease-free equilibrium (DFE). Linearizing system (4.2) about the DFE, the Jacobian matrix of infected subsystem reads

$$J_0 = \begin{bmatrix} -1/T_E & \eta_I c_B \\ 1/T_E & -1/T_I \end{bmatrix}. \tag{4.4}$$

Then, the largest eigenvalue of J_0 (*i.e.,* early exponential growth rate r) is

$$r = \frac{1}{2}\left[-\left(\frac{1}{T_E}+\frac{1}{T_I}\right) + \sqrt{\left(\frac{1}{T_E}-\frac{1}{T_I}\right)^2 + 4\frac{\eta_I c_B}{T_E}}\right]. \tag{4.5}$$

The assumed model parameters used in the model are shown in Table 4.3.

We denote $c(t) = (c_S(t), c_E(t), c_I(t), c_R(t))^T$ as the contact rate vector at time t, where $(\cdot)^T$ denotes a matrix transpose. The effective reproduction number $\mathcal{R}_{\mathit{eff}}(t)$ is

$$\mathcal{R}_{\mathit{eff}}(t) = \overbrace{T_I}^{\text{average infectious time}} \times \overbrace{\eta_I(t)c_I(t)\frac{c_S(t)S(t)}{Q(t)}}^{\text{infection rate in susceptible population}}, \tag{4.6}$$

where $Q(t) = c_S(t)S(t) + c_E(t)E(t) + c_I(t)I(t) + c_R(t)R(t)$.

Initial conditions and contact rate. The model assumes an initial total population of $1,000,000$ (one million) denoted as N_0. An initial outbreak is seeded in this population given one infected individual. The simulation is run for two months (60 days) with fixed baseline contact rate (all c's are equal to c_B) - we use this time point (which we denote time t_0 in our simulations) as the time at which intervention policies might be applied. The individual behaviors (or activities) are quantified by contact rates, $c_S(t),\ c_E(t),\ c_I(t)$ and $c_R(t)$, thus the control of contact rates can be mapped to intervention strategies. For examples, when c_S goes down that means shelter-in-place, when c_E or c_I goes down that can mean quarantine and isolation. When there is no intervention during the epidemic, the

population dynamics of SEIR model is shown in Fig. 4.8. At the time intervention starts (60 days), the disease spreads through the population without any intervention leading to incidence 19 (per 10,000), prevalence 0.4%, and a cumulative infection level of 0.8%.

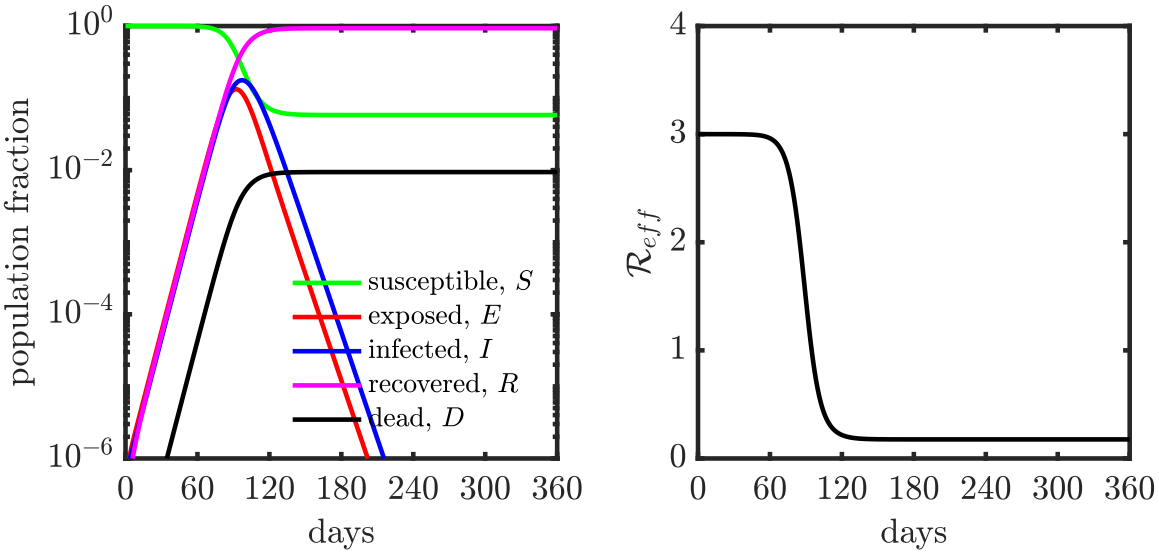

Figure 4.8: Population dynamics of SEIR model without control, *i.e.,* all $c's$ are equal c_B from t_0 to t_f. (Left) Population dynamics of SEIR model without control. (Right) Epidemic growth as measured by the effective reproduction number ($\mathcal{R}_{eff}$), the basic reproduction number $\mathcal{R}_0$ is 3.

4.4.2 Optimal control formulation

Here, we aim to optimally deploy public health control strategies (via control of the contact rates) that minimizes deaths during the outbreak while keeping the socioeconomic costs low. The baseline average of contacts at time t, $Q(t)$, equals $c_B N(t)$, where c_B is the baseline contact rate and $N(t) = S(t) + E(t) + I(t) + R(t)$ is the total number of alive individuals. The socioeconomic costs may result from two consequences of contact rate interventions: (1) loss of essential connections; (2) shifting of roles relative to baseline, as quantified by variation in contact rates by testing status. Given the intervention policy $c(t)$ at time t, we quantify the socioeconomic costs as $\mathcal{E}_1 + \mathcal{E}_2$, where $\mathcal{E}_1$ and $\mathcal{E}_2$ may take form

of

$$\begin{aligned}\mathcal{E}_1(Q(t);W_1) &= W_1\text{exp}\left(K\left(\frac{c_B N(t)-Q(t)}{c_B N(t)}\right)\right)\\ \mathcal{E}_2(c(t);W_2) &= \frac{1}{2}\sum_{i\in\{S,E,I,R\}} w_i\left(\frac{c_B-c_i(t)}{c_B}\right)^2\\ &= \frac{1}{2}\left(\frac{c_B-c(t)}{c_B}\right)^T W_2\left(\frac{c_B-c(t)}{c_B}\right),\end{aligned} \tag{4.7}$$

where $W_1 \geq 0$, $W_2 = \text{diag}(w_S, w_E, w_I, w_R) \succ 0$ are weight parameters, and K is a constant shape parameter for the exponential function. In the absence of any strategy, there are few deaths. This would mean that $N(t) \approx N_0$. For the sake of simplicity, $\mathcal{E}_1$ is approximated as $W_1\text{exp}\left(K\left(c_B N_0 - Q(t)\right)/c_B N_0\right)$. For every t, we restrict the contact rate vector $c(t) \in [c_{min}, c_{max}]^4$, where c_{min} and c_{max} are the minimum contact rate and maximum contact rate. The set $C = [c_{min}, c_{max}]^4$ is a convex and compact set in $\mathbb{R}^4$. We define the space of *admissible controls*, denoted by $\mathcal{A}$, as the set of Lebesgue-measurable functions $c : [t_0, t_f] \longrightarrow C$. The (dimensionless) cost functional is written in the following Bolza form,

$$\mathcal{J}(c) = \overbrace{W_D\frac{D(t_f)}{N_0}}^{\text{costs of deaths}} + \int_{t_0}^{t_f} \overbrace{\mathcal{E}_1(Q(t);W_1)+\mathcal{E}_2(c(t);W_2)}^{\text{socioeconomic costs}} + \overbrace{W_I\frac{I(t)}{N_0}}^{\text{infectious case costs}} \text{ dt}, \tag{4.8}$$

where $W_I \geq 0$ and $W_D \geq 0$ are weight regulators. The optimal control problem is

$$\min\{\mathcal{J}(c)|c \in \mathcal{A}\}. \tag{4.9}$$

The weight parameters used in Eq. 4.8 are shown in table 4.4, these weight parameters are set to balance the scale of different cost components in Eq. 4.8.

However, frequent and continuous updates bring in practical issues in terms of (1) establishing how subtle changes in contact rates actually translate into applicable changes in individual behaviors (*i.e.*, a continuous strategy can not be practically implemented), and

(2) individual fatigue (and reduced adherence to proposed measures) due to frequent behavioral adjustments (*i.e.*, frequent update is also impractical). To address these concerns, we need to modify the space of controls $\mathcal{A}$.

To begin with, we fix the full time horizon of control as $[t_0, t_f]$. For example, t_0 is fixed to 60 days after outbreak (see Sect. 4.4.1) and t_f to 360 days after outbreak, where we set the timing of the outbreak to 0. We only consider an intervention policy which is updated a finite number of times in the interval $[t_0, t_f]$. These epochs are denoted by $t_0 < t_1 < t_2 < \cdots < t_M = t_f$. Let $\mathcal{O}$ denote the corresponding partition of $[t_0, t_f]$, and denote by $\mathcal{F}(\mathcal{O})$ the space of functions $c : [t_0, t_f] \to \mathbb{R}^4$ which have constant values in the intervals $[t_{m-1}, t_m)$, $m = 1, 2, \ldots$. The resulting optimal control problem is

$$\min \{\mathcal{J}(c) | c \in \mathcal{A} \cap \mathcal{F}(\mathcal{O})\}. \tag{4.10}$$

In most cases, the exposed individuals are unaware of their infection status, so it's impractical to control their behaviors separately from the susceptible individuals. Hence, we view them as susceptibles for the purpose of policy setting and set $c_E(t) = c_S(t)\ \forall t \in [t_0, t_f]$. In doing so, the contact rate vector $c(t)$ actually is a three dimensional vector consisting of $c_S(t)$, $c_I(t)$ and $c_R(t)$.

4.4.3 Numerical algorithm and simulation details

We follow the framework presented in Polak [111] for computational optimal control based on optimization on Hilbert spaces. We first discuss the conceptual algorithm in an abstract setting of infinite-dimensional spaces, and then provide approximation details in the sequel.

Let $L_2^n[t_0, t_f]$ denote the space of equivalence classes of square integrable functions from $[t_0, t_f]$ into $\mathbb{R}^n$ ($n = 3$ in our case). We use the notation $\|\cdot\|$ and $\langle \cdot, \cdot \rangle$ for the norm and scalar product in Euclidean space (e.g. $\mathbb{R}^n$), and use $\|.\|_{\mathcal{H}}$ and $\langle ., . \rangle_{\mathcal{H}}$ for the norm and scalar product in a Hilbert space $\mathcal{H}$. For example, given $u, v \in L_2^n[t_0, t_f]$ (a Hilbert

space), the norm $\|.\|_2$ and scalar product $\langle .,. \rangle_2$ are: $\|u\|_2 = \sqrt{\int_{t_0}^{t_f} \|u(t)\|^2 \, \mathrm{dt}}$; $\langle u, v \rangle_2 = \int_{t_0}^{t_f} \langle u(t), v(t) \rangle \mathrm{dt}$.

In the optimal control problem under consideration, we define the state variable of the system, $x \in \mathbb{R}^5$, by $x = (S, E, I, R, D)^T$. We also define the control variable, $c \in \mathbb{R}^3$, by $c = (c_S, c_I, c_R)^T$. The dynamic equation of the system, Eq. 4.2, can be rewritten in a compact form:

$$\dot{x}(t) = f(x(t), c(t)), \tag{4.11}$$

where dot represents differentiation with respect to time t, and $f(x(t), c(t))$ is the right hand side (RHS) of equations 4.2. The cost functional defined by Eq. 4.8 can be written succintly as

$$\mathcal{J}(c) = \phi(x(t_f)) + \int_{t_0}^{t_f} L(x(t), c(t)) \, \mathrm{dt}, \tag{4.12}$$

where $L(x(t), c(t)) := \mathcal{E}_1(Q(t); W_1) + \mathcal{E}_2(c(t); W_2) + W_I \frac{I(t)}{N_0}$ and $\phi(x(t_f)) = W_D \frac{D(t_f)}{N_0}$. The costate (adjoint) variable, $\lambda(t) \in \mathbb{R}^5$, is defined by the following equation,

$$\dot{\lambda}(t) = -\left(\frac{\partial f}{\partial x}(x(t), c(t))\right)^T \lambda(t) - \left(\frac{\partial L}{\partial x}(x(t), c(t))\right)^T, \quad \lambda(t_f) = \nabla_x \phi(x(t_f)). \tag{4.13}$$

Next, recall the optimal control problem defined by Eq. 4.10, where the cost functional (performance integral) $\mathcal{J} : \mathcal{A} \to \mathbb{R}$ is defined by Eq. 4.12. We will propose a gradient-descent algorithm for solving this problem, where the gradient $\nabla \mathcal{J}(c(t))$ is given by the following equation,

$$\nabla \mathcal{J}(c(t)) = \left(\frac{\partial f}{\partial c}(x(t), c(t))\right)^T \lambda(t) + \left(\frac{\partial L}{\partial c}(x(t), c(t))\right)^T; \tag{4.14}$$

see [111, 112, 113].

The principal elements of most gradient-descent algorithms (including the one described here) are the descent direction and the stepsize. For our problem, the descent

direction is based on $-\nabla\mathcal{J}(c(t))$; in fact, it is the projection of $c(t) - \nabla\mathcal{J}(c(t))$ into the constraint-set $C = [c_{min}, c_{max}]^3$ as defined in Sect. 4.4.2. The stepsize that we use is the Armijo stepsize (see [111]) described in the sequel, which gives an approximate line minimization of $\mathcal{J}$ in the computed descent direction from the control $c(t)$.

Consider first the conceptual algorithm. In its formal presentation by Algorithm 1, below, we use the term "compute" in a conceptual sense, since the 'computations' refer to elements in the Hilbert space $L_2^n[t_0, t_f]$. Also, we use the notation $\mathcal{P}_{\mathcal{A}}$ to mean the projection from $L_2^n[t_0, t_f]$ into the space $\mathcal{A}$.

Algorithm $\star\star$: Conceptual. Given a control iteration $c^{(i)} \in \mathcal{A}$, compute from it the next iteration, $c^{(i+1)} \in \mathcal{A}$, as follows.

Parameters: Constants $\alpha \in (0, 1)$ and $\beta \in (0, 1)$. (*These parameters play a role in the computation of the step size.*)

1. Compute the state trajectory $x(t)$ and costate trajectory $\lambda(t)$ by Eqs. 4.11 and 4.13, respectively.

2. Compute $\nabla\mathcal{J}(c(t))$ by Eq. 4.14.

3. $\Big($*Here we define, for all* $y \geq 0$, $h^{(i)}(y) = \mathcal{P}_{\mathcal{A}}(c^{(i)} - y\nabla\mathcal{J}(c^{(i)}))\Big)$. Compute $\ell(i) > 0$ defined as follows,

$$\ell(i) = \min\{\ell = 0, 1, ...|\mathcal{J}(h^{(i)}(\beta^\ell)) - \mathcal{J}(c^{(i)}) \leq -\alpha\langle\, \nabla\mathcal{J}(c^{(i)}), c^{(i)} - h^{(i)}(\beta^\ell)\rangle_2\}.$$

4. Set $\gamma(i) = \beta^{\ell(i)}$, and set

$$c^{(i+1)} = \mathcal{P}_{\mathcal{A}}(c^{(i)} - \gamma(i)\nabla\mathcal{J}(c^{(i)})).$$

We remark that $\mathcal{P}_{\mathcal{A}}(c^{(i)} - \gamma(i)\nabla\mathcal{J}(c^{(i)})) - c^{(i)}$ is descent direction for $\mathcal{J}$ from $c^{(i)}$, and $\gamma(i)$, the Armijo stepsize, provides an approximate-line minimization in that direction.

The main modification of Algorithm 1 towards implementation is in numerical solutions of the state equation and costate equation. Furthermore, the time-interval $[t_0, t_f]$ has to be discretized by a suitable grid in order to adequately represent various time-dependent functions such as $c^{(i)}(t)$ and $\nabla\mathcal{J}(c(t))$. All of this can be achieved by a common grid, $\mathcal{G}_0 := \{t_0, t_1, \ldots, t_N\} \subset [t_0, t_f]$. Furthermore, the projection $\mathcal{P}_{\mathcal{A}}(c^{(i)} - \beta^\ell \nabla\mathcal{J}(c^{(i)}))$ in Step 3 of Algorithm $\star\star$ can be computed as follows: For a given grid-point $t_j \in \mathcal{G}_0$, project the point $c^{(i)}(t_j) - \beta^\ell \nabla\mathcal{J}(c^{(i)})(t_j) \in \mathbb{R}^3$ into the set C, where $C = [c_{min}, c_{max}]^3 \subset \mathbb{R}^3$. This can be done by a simple co-ordinate projection since C is a box. Denote the result of this pointwise projection by $\mathcal{P}_C(c^{(i)}(t_j) - \beta^\ell \nabla\mathcal{J}(c^{(i)})(t_j)) \in C$, and observe that the function comprised of a zero-order or first-order interpolation of these points can serve to approximate the functional projection $\mathcal{P}_{\mathcal{A}}(c^{(i)} - \beta^\ell \nabla\mathcal{J}(c^{(i)}))$.

These modifications of the conceptual algorithm give an implementable version for it. The resulting implementable algorithm falls in Polak's framework of numerical optimal control [111] which includes results pertaining to asymptotic convergence.

As noted, the control $c(t)$ must be piecewise constant and maintain constant values for substantial periods. At the same time, the state trajectory typically is continuous and not piecewise constant. Therefore, it is natural to maintain the present framework of continuous-time optimal control and not to consider the problem in the setting of discrete-time systems. To do that, we have to consider a form of projection of the control functions, $c(t)$, into the space of piecewise-constant functions. We next describe the specific way we did that in our simulations.

Consider an increasing set of points $\{t_0 = t_0 < t_1 < t_2 < \ \ldots \ < t_M = t_f\}$, and the corresponding partition of the time-interval $[t_0, t_f)$ by the subintervals $[t_{m-1}, t_m)$, $m = 1, \ldots, M$. Denote the interval $[t_{m-1}, t_m)$, $m = 1, \ldots, M$, by Δ_m; right-close the last interval to be $\Delta_M = [t_{M-1}, t_M]$, and denote the partition by $\mathcal{O}$. Let $\psi_m(t)$, $m = 1, \ldots, M$ denote the indicator function of the subinterval ψ_m, namely $\psi_m(t) = 1$ for $t \in \psi_m$ and $\psi_m(t) = 0$ otherwise. A continuous-time signal can be approximated over an interval by

a constant equal to its average value over that interval. Given a continuous-time policy $c : [t_0, t_f] \to \mathbb{R}^3$, the piecewise constant reconstruction is

$$\widetilde{c}(t) = \sum_{m=1}^{M-1} \theta_m \psi_m(t), \quad \theta_m = \frac{1}{|\Delta_m|} \int_{t_m}^{t_{m+1}} c(s)\, \mathrm{ds}, \tag{4.15}$$

here $\theta_m \in \mathbb{R}^3$. Let $\mathcal{V}_{\mathcal{O}}$ denotes the operator comprising this piecewise- constant reconstruction procedure. Then Eq. 4.15 can be written as $\widetilde{c} = \mathcal{V}_{\mathcal{O}}(c)$. Now we modify the algorithm by replacing the projection operator $\mathcal{P}_{\mathcal{A}}$ in Step 3 by the operator $\mathcal{V}_{\mathcal{O}} \circ \mathcal{P}_{\mathcal{A}}$, comprised of $\mathcal{P}_{\mathcal{A}}$ followed by $\mathcal{V}_{\mathcal{O}}$.

In summary, the implementable algorithm that we use consists of the following modification of Algorithm $\star\star$:

1. Compute $x(t)$ and $\lambda(t)$ by numerical integrations using the forward-Euler method.
2. Compute $\nabla \mathcal{J}(c(t))$ only at the points t_j on the grid $\mathcal{G}_0$.
3. Redefine $h^{(i)}(y)$ as $h^{(i)}(y) = \mathcal{V}_{\mathcal{O}} \circ \mathcal{P}_{\mathcal{A}}(c^{(i)} - y \nabla \mathcal{J}(c^{(i)}))$.
4. Replace $\mathcal{P}_{\mathcal{A}}$ by $\mathcal{V}_{\mathcal{O}} \circ \mathcal{P}_{\mathcal{A}}$.

Simulation details. The model assumes an initial total population of $1,000,000$ (one million) denoted as N_0. An initial outbreak is seeded in this population given one infected individual. The simulation is run for two months (60 days) with fixed baseline contact rate (all c's are equal to c_B) - we use this time point (which we denote time t_0 in our simulations) as the time at which intervention policies might be applied: we have $c(t) = c_B \; \forall t \in [0, t_0]$, and we set the initial state to $x_0 = x(t_0)$.

For the algorithm, we set $\alpha = 0.1$ and $\beta = 0.5$, the grid's time increments to 0.05, $\Delta_m = 30$ days, $t_0 = 60$ and $t_f = 360$ days. For the uncontrolled part of the simulation we take $c(t) = c_B$ for all $t \in [0, t_0]$. The term $\Theta(i) := |\mathcal{J}(c^{(i+1)}) - \mathcal{J}(c^{(i)})|/\mathcal{J}(c^{(i)})$ acts as a convergence indicator for stopping the algorithm. The algorithm is terminated whenever

$\Theta(i) \leq 10^{-6}$.

4.4.4 Optimised time-dependent contact rate

Fraction of working-days recovered. One way of estimating the economic impact is measuring the *fraction of working-days recovered*, *i.e.,* how many days are people working. We assume that if a person has a contact rate less than the base contact rate (c_B), it implies a proportional reduction of in-person contacts that have a direct economic benefit. For example, for a susceptible individual, the working fraction at day t can be computed as $c_S^*(t) = \min\{1, c_S(t)/c_B\}$, where c_B is the baseline contacting rate. This ensures that contact rates above the baseline does not correspond to an increase in hours worked. For a given contact rate policy $c = (c_S, c_E, c_I, c_R)^T$, the working days restored in the period $[t_0, t_f]$ is

$$\Psi_{\textit{restored}} = \int_{t_0}^{t_f} c_S^*(t)S(t) + c_E^*(t)E(t) + c_I^*(t)I(t) + c_R^*(t)R(t)\ \text{dt}, \tag{4.16}$$

where $c_k^*(t) = \min\{1, c_k(t)/c_B\}$, $k \in \{S, E, I, R\}$, is the working fraction of an individual in subpopulation class k at day t. When there is no policy intervention, the contact rate of each individual is c_B for all time, the working days will be maximized, which can be written as

$$\Psi_{max} = \int_{t_0}^{t_f} S(t) + E(t) + I(t) + R(t)\ \text{dt}. \tag{4.17}$$

Then, the fraction of working days restored can be written as

$$\Psi(c) = \frac{\Psi_{\textit{restored}}}{\Psi_{max}}. \tag{4.18}$$

Economic costs are proportional to $1 - \Psi(c)$; such that economic impacts of policies are minimized as $\Psi(c)$ approaches 1

Varying the relative importance of the illness-related cost vs. socioeconomic costs. The relative importance given to the socioeconomic impact of the epidemic and the cost associated with deaths and infection spread is critical to design intervention policies. From Eq. 4.8, we note that the cost function $\mathcal{J}$ can be decomposed into the two parts, socioeconomic costs ($\mathcal{J}_E$) and costs of infectious diseases ($\mathcal{J}_I$), $\mathcal{J} = \mathcal{J}_E + \mathcal{J}_I$, where

$$\begin{aligned} \mathcal{J}_E &= \int_{t_0}^{t_f} \mathcal{E}_1(Q(t); W_1) + \mathcal{E}_2(c(t); W_2)\, \mathrm{dt} \\ \mathcal{J}_I &= W_D \frac{D(t_f)}{N_0} + \int_{t_0}^{t_f} W_I \frac{I(t)}{N_0}\, \mathrm{dt}. \end{aligned} \tag{4.19}$$

In order to explore how to manage and control disease outbreak with low socioeconomic costs, we need to balance the importance of these two seemingly conflicting objectives. To this end, we define a new cost function where the relative importance of $\mathcal{J}_E$ and $\mathcal{J}_I$ can be parameterized. With this parameter, optimal policy decisions can be made based on the relative importance assigned to the socioeconomic effect and public health impacts. Define the relative weight ratio as ξ and the altered cost function is $\mathcal{J}(c; \xi) = \mathcal{J}_E + \xi \mathcal{J}_I$. As ξ increases, the relative importance of costs associated with death and spread of infection are increased vis-a-vis the socioeconomic impact and vice versa. The optimal intervention policies with different relative importance ratios ($\xi = 10^{-4},\ 1,$ and 10^4) vary with isolation efficiencies ($25\%,\ 50\%,\ 75\%$) are shown in Figs. 4.9, 4.10, 4.11.

For example of balance case ($\xi = 1$) in the case of 50% isolation efficiency, Fig. 4.10 (middle) shows that the way of managing the epidemic while considering the socioeconomic impact is to isolate all the infected cases and enhance the interactions of recovered cases (*i.e., shielding*, [61]), the susceptible cases are stay home first and slowly go back to normal towards the end of intervention period. Using the optimized intervention policy (*i.e.,* optimal contact rate), the reduction in final deaths ($D(t_f)$) is substantial ($\sim 75\%$). The fraction of working-days recovered is about $\sim 66\%$. The results suggest advantages of isolation of infected cases and shielding enhancement of recovered cases.

4.4.5 Inferring state-dependent heuristic policies from optimal control solutions

In the previous sections, an optimal policy based on contact rates of different sub-populations was derived. However, as is often the case with optimal control solutions, these policies are open-loop, that is, once computed, they are prescribed to the system without feedback. Therefore, open-loop policies can have large sensitivities to modeling errors and signal-delays in the loop, especially if the system is unstable, as is the case with dynamic models of epidemics near the disease-free equilibrium at the onset of an outbreak. To address this, we design a feedback law for optimizing a 'reasonable' performance metric which, though different from the one of the optimal control problem, gives similar respective measures of two important performance metrics: total mortality ($D(t_f)$), and working fractions (Ψ). In Sect. 4.4.6 we verify this point by comparative simulations of the optimal control solution and the feedback control system, and not surprisingly, the sensitivity of the former with respect to a one-cycle (30-days) delay is much larger than that of the latter.

The optimal control solutions reveal a general structure that guides us in the choice of the feedback control law. The patterns observed in the computed optimal-policy solutions (see Figs. 4.9, 4.10, 4.11) suggest that the contact rates for the infected cases should be the smallest possible while the recovered population should be used as shields. Further, they display switch overs between the low and high contact rates for the susceptible populations, and these tend to occur towards the end of the lock-down period in a way that depends on the numbers of infected and recovered individuals.

To find the state feedback policy, the I-R (Infected-Recovered) phase plane is divided into 2 parts - one where the susceptibles need to isolate and another where they can get back to work. If the number of infected cases is high, the susceptible population should isolate to reduce the infection spread. For simplicity, the I-R plane is divided by a line, though better classification boundaries may exist. On one side of the line, the contact rate for the susceptible population is set to the minimum while on the other side, it is equal to the baseline (corresponding to opening the system).

The optimal slope of the dividing line is found via a *genetic algorithm* [114] using Matlab's built-in optimization function `ga`, with the maximum generation number (set to 30) serving as the stopping criterion [115]. The intercept of the line is fixed to a small negative number (10^{-3}) as the results are not affected by the intercept. The slope parameter is called θ, and the following cost function is minimized:

$$\mathcal{J}(\theta) = \widetilde{w}\frac{D(t_f)}{N_0} + \Psi(c), \tag{4.20}$$

where $D(t_f)/N_0$ gives the normalized casualties, $\Psi(c)$ is the fraction of working-days restored and $\widetilde{w}$ is a weight to bring the two terms on the same scale (see Table 4.4). The output of the genetic algorithm is θ^*, the slope of the optimal dividing line. We assume that the divided plane on the side of the line with the origin, *i.e.,* zero infected and recovered cases, is the side where the susceptibles are free to work, while the divided plane on the other side corresponds to lockdown. The simulation is run for different isolation and shielding levels and the compiled results are shown in Fig. 4.4. The isolation efficiencies vary from 35% to 75% while the shielding ratio varies from no shielding to $4\times$ shielding.

We note that as the efficiency of isolation increases, the susceptible population can be let out for a longer duration towards the end of the epidemic. This is because the reduced contact rate of the infected population reduces the spread of infection. If the isolation efficiency is 65% or more, there is no need for the susceptible population to be in lockdown. Similar observations can be made for the shielding ratio. While the effects of it are not as dramatic, an increase in shielding ratio decreases the force of infection, resulting in a a lower time necessary for lockdown.

4.4.6 Sensitivity analysis

Sensitivity of optimal control and feedback control to mis-timed implementation of policies. We compute an optimal control for a system with a delayed input. We do not

assume any modeling uncertainty, and attribute the perturbation only to the delayed application of the computed control. Suppose that an optimal control is computed for a scenario where its application is slated to commence 30 days after the outbreak of an epidemic, but the computed input control is uniformly delayed by 30 days. Then, by simulating the epidemic with a delayed policy, we can compare total deaths and working fraction for the delayed system with the results obtained without delay and with the same initial conditions.

The results, comprising total death and working fraction, are presented in Table 4.1 for various isolation efficiencies. These findings indicate higher death rates as well as higher working fractions for the delayed system except for the third, and highest efficiency of isolation, where the respective performance measures are similar. For the case of 50% isolation, the death count is more than doubled due to delay. This significant difference in performance metrics demonstrates the shortcomings of implementing a policy based on optimal control if the system is not precise.

We also tested the sensitivities of the total death and working fraction to 30-day delays. The results, shown in Table 4.2 below, indicate low sensitivity compared to the observed results for the optimal control solution. We compared these performance metrics obtained from applications of the optimal control vs. feedback control to the system without delay. The results, summarized in Tables 4.1 and 4.2 respectively, indicate similar performance with respect to the performance metrics used. Thus, feedback control is nearly as good as optimal control if there is no delay; while having more robust features in the event that there is a delay in application.

Sensitivity of feedback control for mis-estimated isolation efficiency. Robustness of the feedback strategy (in terms of model mis-specification) can be studied by computing the total deaths and working fraction for the system with mis-specified isolation efficiency (c_{min}). In doing so, health and economic outcomes for the mis-specified system (i.e., overestimate or underestimate of isolation efficiency) are compared with the results obtained

from the system with an accurately estimated isolation efficiency.

The isolation efficiency is varied from 35% to 75% with a 2% increment. For every isolation efficiency (for example with a true isolation efficiency of 50%), we consider three cases - unbiased, overestimated and underestimated isolation efficiency. For the unbiased case, i.e., when the isolation efficiency is accurate, we apply the feedback strategy (optimal line) associated with 50% isolation efficiency to the system to obtain the total deaths and working fraction. Second, for the case of overestimation, the isolation efficiency is assumed to be $\epsilon\%$ higher, so we apply the feedback strategy associated with $(50 + \epsilon)\%$ isolation efficiency to obtain the total deaths and working fraction in the overestimated scenario. Finally, we consider the underestimated case that is similar to the overestimated case, in which the feedback strategy associated with $(50 - \epsilon)\%$ isolation efficiency is applied to the system.

The results are presented in Fig. 4.13. The feedback strategy is robust, especially when isolation efficiency is either low ($< 40\%$) or high ($> 65\%$). The results are expected as the feedback strategy is stationary in those ranges, i.e., when isolation efficiency is low, our policy suggests lockdown (for susceptible individuals) most of time; when isolation efficiency is high, our policy suggests staying open (for susceptible individuals), see Fig. 4.4. However, the feedback strategy is (slightly) sensitive when the isolation efficiency is in the range of $40\% \sim 65\%$. From 40% isolation efficiency to 65% isolation efficiency, lockdown policy (for susceptible individuals) switches to full open decision (for susceptible individuals), hence a small estimation error may cause to nonnegligible changes in policy, which may lead to the variability in working fraction and total deaths. As we can observe from Fig. 4.4, the feedback strategy varies rapidly from $40\% \sim 65\%$, i.e., from lockdown most of time to open entirely.

4.4.7 An age-structured model and age-dependent immune shielding deployment

An age-structured model. We present the age-structured epidemiological model discussed in the Sect. 4.2.5. Consider a population of susceptible S, exposed E, infectious asymptomatic I_{asym}, infectious symptomatic I_{sym}, and recovered R who are free to move, without restrictions in a 'business as usual' scenario. A subset of symptomatic cases will require hospital care, which we further divide into subacute I_{hsub}, and critical/acute (*i.e.,* requiring ICU intervention) I_{hcrit} cases. Vital dynamics (births and other causes of death) are ignored for simplicity. The model is visually represented in Fig. 4.14 and the system of nonlinear differential equations governing this age-structured epidemiological model are shown below:

$$
\begin{aligned}
\frac{dS(a)}{dt} &= -\overbrace{\frac{\beta_s S(a) I_{sym,tot}}{N_{tot}+\alpha R_{Shields}}}^{symptomatic\ contact} - \overbrace{\frac{\beta_{asym} S(a) I_{asym,tot}}{N_{tot}+\alpha R_{Shields}}}^{asymptomatic\ contact} \\
\frac{dE(a)}{dt} &= \overbrace{\frac{\beta_{sym} S(a) I_{sym,tot}}{N_{tot}+\alpha R_{Shields}}}^{symptomatic\ contact} + \overbrace{\frac{\beta_{asym} S(a) I_{asym,tot}}{N_{tot}+\alpha R_{Shields}}}^{asymptomatic\ contact} - \overbrace{\gamma_e E(a)}^{onset\ of\ infectiousness} \\
\frac{dI_{asym}(a)}{dt} &= \overbrace{p(a)\gamma_e E(a)}^{asymptomatic\ onset} - \overbrace{\gamma_a I_{asym}(a)}^{recovery} \\
\frac{dI_{sym}(a)}{dt} &= \overbrace{(1-p(a))\gamma_e E(a)}^{symptomatic\ onset} - \overbrace{\gamma_s I_{sym}(a)}^{transfer\ from\ I_{sym}} \\
\frac{dI_{hsub}(a)}{dt} &= \overbrace{h(a)(1-\xi(a))\gamma_s I_{sym}(a)}^{subcritical\ cases} - \overbrace{\gamma_h I_{hsub}(a)}^{transfer\ from\ I_{hsub}} \\
\frac{dI_{hcrit}(a)}{dt} &= \overbrace{h(a)\xi(a)\gamma_s I_{sym}(a)}^{critical\ (ICU)\ cases} - \overbrace{\gamma_h I_{hcrit}(a)}^{transfer\ from\ I_{hcrit}} \\
\frac{dR(a)}{dt} &= \overbrace{\gamma_a I_{asym}(a)}^{recovery\ from\ I_{asym}} - \overbrace{(1-h(a))\gamma_s I_{sym}(a)}^{recovery\ from\ I_{sym}} - \overbrace{\gamma_h I_{hsub}(a)}^{recovery\ from\ I_{hsub}} - \overbrace{(1-\mu)\gamma_h I_{hcrit}(a)}^{recovery\ from\ I_{hcrit}} \\
\frac{dD(a)}{dt} &= \overbrace{\mu\gamma_h I_{hcrit}(a)}^{mortality},
\end{aligned}
\tag{4.21}
$$

where $I_{sym,tot}$ are the total number (across all age classes) of symptomatic infectious individuals, $I_{asym,tot}$ are the total number of asymptomatic infectious individuals, N_{tot} is the total number of alive individuals (not in the D state), and $R_{Shields}$ are the number of recovered individuals who could serve as serological shields - which we define as those of ages between 20 and 59. The assumed model parameters used in the baseline models are shown in Tables 4.5 and 4.6.

Basic reproduction number $\mathcal{R}_0$. Based on the parameters in Tables 4.5 and 4.6, $\mathcal{R}_0$ is calculated as a weighted average between the symptomatic and asymptomatic reproduction numbers $\mathcal{R}_{asym}$ and $\mathcal{R}_{sym}$ respectively:

$$\mathcal{R}_0 = p\mathcal{R}_{asym} + (1-p)\mathcal{R}_{sym}. \tag{4.22}$$

These can be further expanded based on age groups to obtain:

$$\mathcal{R}_0 = \sum_{a \in \text{Age Groups}} p(a) \cdot f(a) \cdot \mathcal{R}_{asym}(a) + (1-p(a)) \cdot f(a) \cdot \mathcal{R}_{sym}(a), \tag{4.23}$$

which yields a basic reproduction number of about 1.57 in the low scenario and 2.33 in the high scenario.

Initial condition of age-structured model. The baseline model assumes a population of 10,000,000 with age demographics as given in Table 4.6 unless stated otherwise. An initial outbreak is seeded in this population given one exposed individual in the 20-29 age class. The simulation is run forward until 10,000 people have been exposed to the virus (*i.e.,* 10,000 people are no longer in the susceptible states) - we use this time point (which we denote time 0 in our simulations) as the time at which intervention policies might be applied. At this point, once 10,000 people have already been exposed we simulate the dynamics forward either with, or without the interventions.

Age-dependent immune shielding deployment. In system (4.21), we assumed that shields (recovered individuals aged 20-59) were deployed such that they interact with people of all ages equally. In other words, all the susceptible individuals (across ages) have an infection rate that scales with $I_{tot}/(N_{tot} + \alpha R_{shields})$ such that the shields are uniformly interacting with all ages. Here, we explore the outcome of having the shields act in positions where they could be more or less-likely to interact with different age groups, *i.e.,* using the same effort as in the core model, then taking the $\alpha R_{shields}$ of effort but distributing it non-uniformly across ages. To explore the 'optimised' distributions of the shields effort, we introduce non-uniform shield interactions in the model. To do so, we modify the equations of $S(a)$ and $E(a)$ in the core model as follows:

$$\begin{aligned}\frac{dS(a)}{dt} &= -\beta_a \frac{S(a)I_{asym,tot}}{N_{tot} + \alpha R_{shields}(\theta_a/f_a)} - \beta_s \frac{S(a)I_{sym,tot}}{N_{tot} + \alpha R_{shields}(\theta_a/f_a)} \\ \frac{dE(a)}{dt} &= \beta_a \frac{S(a)I_{asym,tot}}{N_{tot} + \alpha R_{shields}(\theta_a/f_a)} + \beta_s \frac{S(a)I_{sym,tot}}{N_{tot} + \alpha R_{shields}(\theta_a/f_a)} - \gamma_e E(a),\end{aligned} \tag{4.24}$$

where f_a is the fraction of the population of age a (f_a-s are fixed parameters) and θ_a is the distributed shielding fraction of the sub-population class of age a, i.e. how we distribute the shields to interact across different age classes. θ_a are the optimization variables. In addition, we define the ratio θ_a/f_a as the age-dependent shielding concentration. When $f_a/\theta_a = 1$ for all ages a, the uniform shields interactions case is recovered *i.e.,* we recover the core model. We note that $\sum_a \theta_a = 1$ such that the effort is the same as in the core model, but allowing for asymmetric distribution across ages. For example, if 25% percent of the population belongs to class a and gets all the shields protection, then $f_a = 0.25$ and $\theta_a = 1$, this implies $\theta_a/f_a = 4$, *i.e.,* a 4-fold boosted protection for that particular class.

Optimization objective. The optimization objective here is to minimize total deaths $D_{tot}(t_f)$, where t_f is the final time of the simulation – 1 year after shielding begins, while keeping ICU beds less than the maximum carrying capacity B at every time instant. We seek to find the optimum distribution for deploying the effort of the serological shields. The

non-uniform shielding fraction can be represent by a vector $\Theta = [\theta_a]_{a=1:10} = [\theta_1,\ ...,\ \theta_{10}]$, and we aim to solve the following minimization problem:

$$\begin{aligned} \min \mathcal{J}(\Theta) = \int_{t_0}^{t_f} \overbrace{W_i \times d(I_{hcri}^{tot}(t))}^{\text{barrier function (constraint)}}\ dt\ +\ \overbrace{W_d \times D_{tot}(t_f)}^{\text{costs of deaths}}, \\ \text{subject to } \sum_{a=1}^{10} \theta_a = 1\ ,\ \theta_a \geq 0 \quad \forall\, a = 1,\ 2,\ ...,\ 10; \end{aligned} \tag{4.25}$$

where W_i are W_d are weight regulators. The barrier function d is chosen such that it increases the cost dramatically as the number of ICU beds in use approach the capacity B of the system, to prevent overloading the healthcare system. To satisfy this property, we pick $d(x) = \log\left(\frac{1}{B-x}\right)$. The barrier function goes to infinity as x approaches B from the left. Here, we consider the maximum capacity B as a 'strict' (or 'hard') constraint and any distributed shielding fraction Θ that leads to the ICU beds exceeding B is not considered a feasible shielding deployment. Given the simulation results shown in main text, we set B as 200 ICU beds per 100,000 for the high scenario case and $B = 80$ ICU beds per 100,000 people for the low scenario case. Note that at this point we are trying to see if we can improve the effectiveness of serological shields, by deploying them unevenly across a population. Moreover, the barrier function in the cost function is negative if $I_{hcri}(t) < B - 1$, which is a 'reward' if occupancy of the ICU beds is low. In practice, we set W_i to be arbitrarily small since it serves much like a constraint, e.g., $W_i = 10^{-7}$. We let $W_d = 1$ as minimizing deaths is the primary goal. The optimization problem (4.25) is solved via a *genetic algorithm* [114] using Matlab's built-in optimization function `ga`, with the maximum generation number (set to 30) serving as the stopping criterion [115]. Genetic (or evolutionary) optimization algorithms do not scale well with complexity, we may choose first-order algorithms (e.g. gradient descent) as our numerical optimization solvers to handle more complex system parameter optimization problems. The derivation of gradient in a more general parameter optimization problem is present in Appendix 4.5.1.

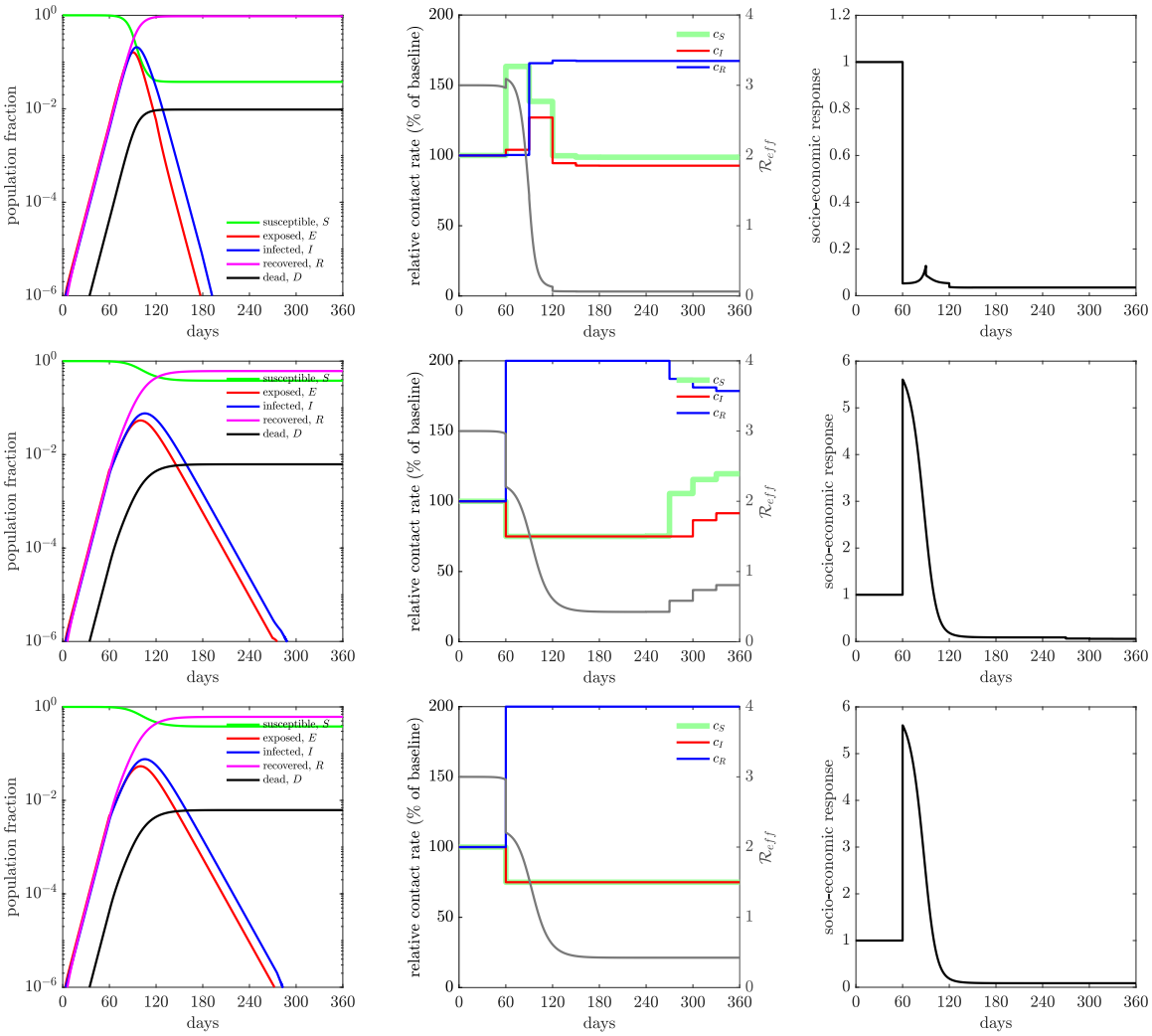

Figure 4.9: Population dynamics in a SEIR model with controlled contact rate (25% isolation efficiency). (Top) The relative importance ratio (ξ) is set as 10^{-4}, the policy (*i.e.,* contact rate) is deployed to primarily minimize socioeconomic costs ($\mathcal{J}_E$). The socioeconomic costs are maintained at low level for all the policy intervention period (see the right panel after 60 days). Final state of the system in terms of population fraction is: $D(t_f) \approx 1\%$, $S(t_f) \approx 4\%$ and $R(t_f) \approx 95\%$, where $t_f = 360$ days. The fraction of working-days recovered is about 100%. (Middle) The relative importance ratio (ξ) is set as 1, the policy (*i.e.,* contact rate) is deployed to minimize infectious diseases costs ($\mathcal{J}_I$) while keeping the socioeconomic impacts low. The Final state of the system in terms of population fraction is: $D(t_f) \approx 0.6\%$, $S(t_f) \approx 38\%$ and $R(t_f) \approx 61\%$, where $t_f = 360$ days. The fraction of working-days recovered is about 91%. (Bottom) The relative importance ratio (ξ) is set as 10^4, the policy (*i.e.,* contact rate) is deployed to primarily minimize infectious diseases costs ($\mathcal{J}_I$). The controlled contact rates of susceptible cases (c_S) and infected cases (c_I) are overlapped at minimum contact rate boundary (c_{min}). The Final state of the system in terms of population fraction is: $D(t_f) \approx 0.6\%$, $S(t_f) \approx 38\%$ and $R(t_f) \approx 61\%$, where $t_f = 360$ days. The fraction of working-days recovered is about 88%. Here, we set $c_{min} = (3/4)c_B$ (*i.e.,* up to 25% isolation efficiency) and $c_{max} = 2c_B$ (*i.e.,* up to twice enhanced interactions).

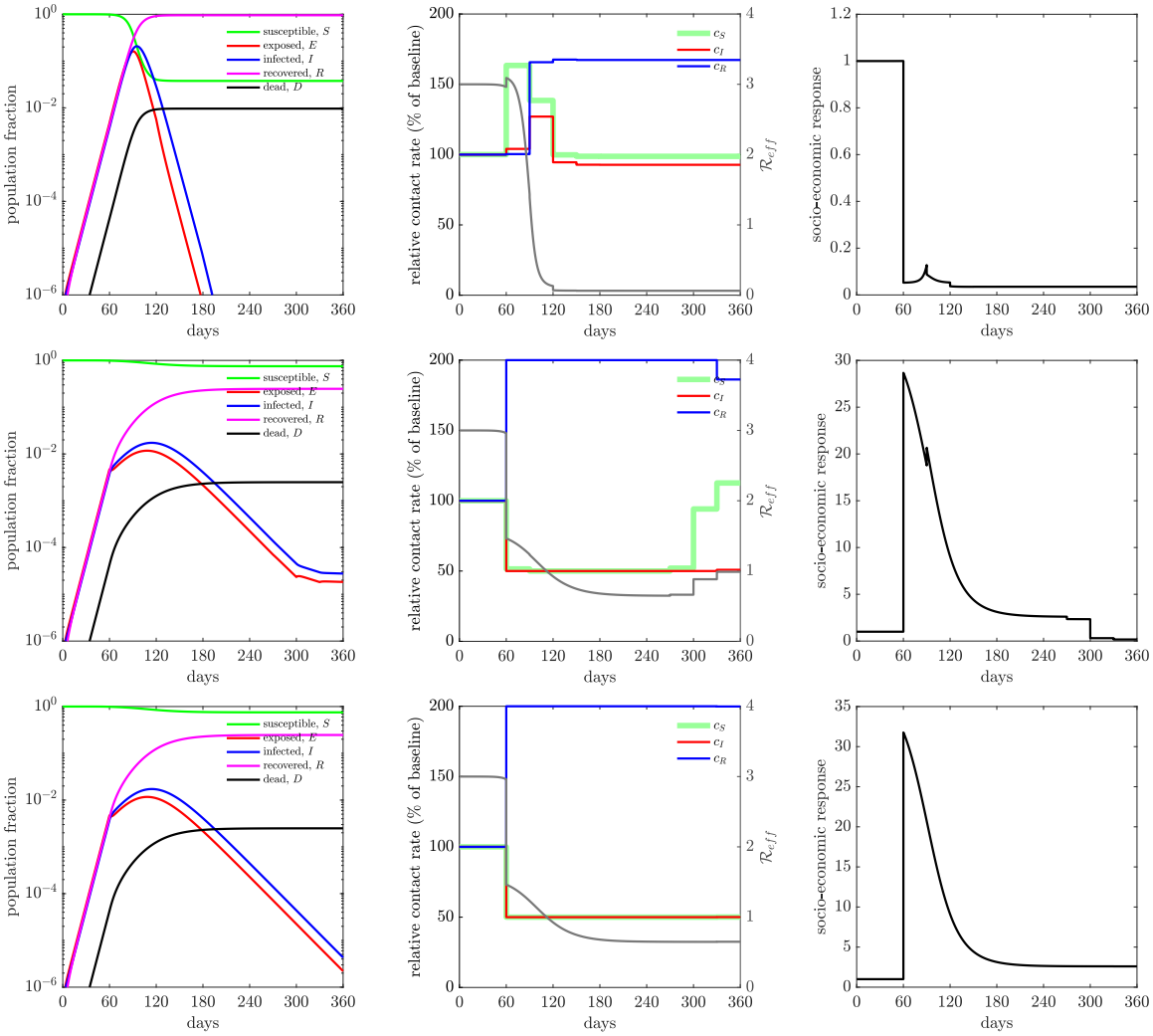

Figure 4.10: Population dynamics in a SEIR model with controlled contact rate (50% isolation efficiency). (Top) The relative importance ratio (ξ) is set as 10^{-4}, the policy (*i.e.,* contact rate) is deployed to primarily minimize socioeconomic costs ($\mathcal{J}_E$). The socioeconomic costs are maintained at low level for all the policy intervention period (see the right panel after 60 days). Final state of the system in terms of population fraction is: $D(t_f) \approx 1\%$, $S(t_f) \approx 3\%$ and $R(t_f) \approx 96\%$, where $t_f = 360$ days. The fraction of working-days recovered is about 100%. (Middle) The relative importance ratio (ξ) is set as 1, the policy (*i.e.,* contact rate) is deployed to minimize infectious diseases costs ($\mathcal{J}_I$) while keeping the socioeconomic impacts low. The Final state of the system in terms of population fraction is: $D(t_f) \approx 0.25\%$, $S(t_f) \approx 75\%$ and $R(t_f) \approx 25\%$, where $t_f = 360$ days. The fraction of working-days recovered is about 66%. (Bottom) The relative importance ratio (ξ) is set as 10^4, the policy (*i.e.,* contact rate) is deployed to primarily minimize infectious diseases costs ($\mathcal{J}_I$). The Final state of the system in terms of population fraction is: $D(t_f) \approx 0.25\%$, $S(t_f) \approx 75\%$ and $R(t_f) \approx 25\%$, where $t_f = 360$ days. The fraction of working-days recovered is about 59%. Here, we set $c_{min} = c_B/2$ (*i.e.,* up to 50% isolation efficiency) and $c_{max} = 2c_B$ (*i.e.,* up to twice enhanced interactions).

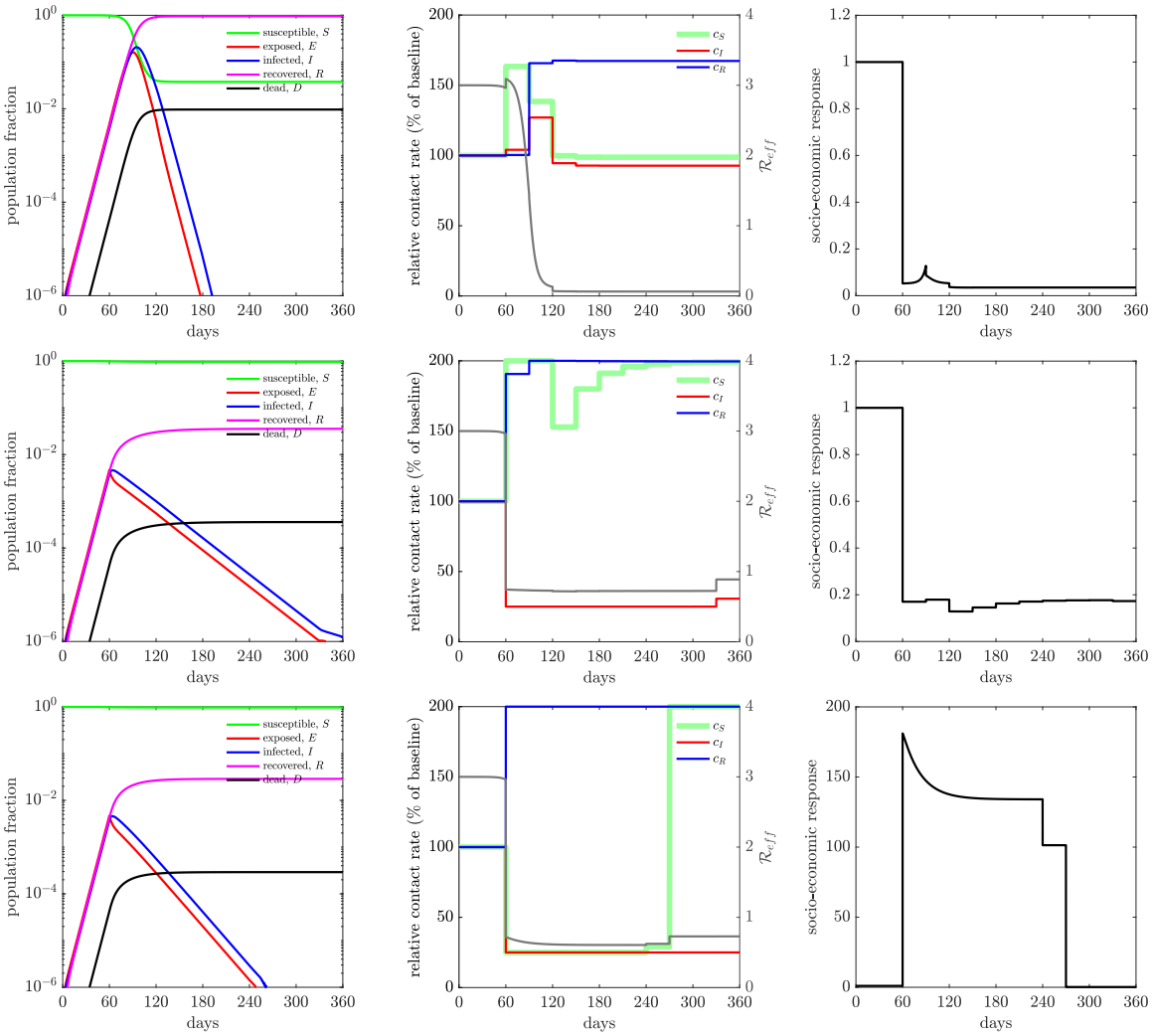

Figure 4.11: Population dynamics in a SEIR model with controlled contact rate (75% isolation efficiency). (Top) The relative importance ratio (ξ) is set as 10^{-4}, the policy (*i.e.,* contact rate) is deployed to primarily minimize socioeconomic costs ($\mathcal{J}_E$). The socioeconomic costs are maintained at low level for all the policy intervention period (see the right panel after 60 days). Final state of the system in terms of population fraction is: $D(t_f) \approx 1\%$, $S(t_f) \approx 4\%$ and $R(t_f) \approx 95\%$, where $t_f = 360$ days. The fraction of working-days recovered is about 100%. (Middle) The relative importance ratio (ξ) is set as 1, the policy (*i.e.,* contact rate) is deployed to minimize infectious diseases costs ($\mathcal{J}_I$) while keeping the socioeconomic impacts low. Infected individuals are locked down at home for all intervention period while susceptible and recovered individuals are free to go out. The Final state of the system in terms of population fraction is: $D(t_f) \approx 0.04\%$, $S(t_f) \approx 96\%$ and $R(t_f) \approx 4\%$, where $t_f = 360$ days. The fraction of working-days recovered is about 100%. (Bottom) The relative importance ratio (ξ) is set as 10^4, the policy (*i.e.,* contact rate) is deployed to primarily minimize infectious diseases costs ($\mathcal{J}_I$). The Final state of the system in terms of population fraction is: $D(t_f) \approx 0.03\%$, $S(t_f) \approx 97\%$ and $R(t_f) \approx 3\%$, where $t_f = 360$ days. The fraction of working-days recovered is about 50%. Here, we set $c_{min} = c_B/4$ (*i.e.,* up to 75% isolation efficiency) and $c_{max} = 2c_B$ (*i.e.,* up to twice enhanced interactions).

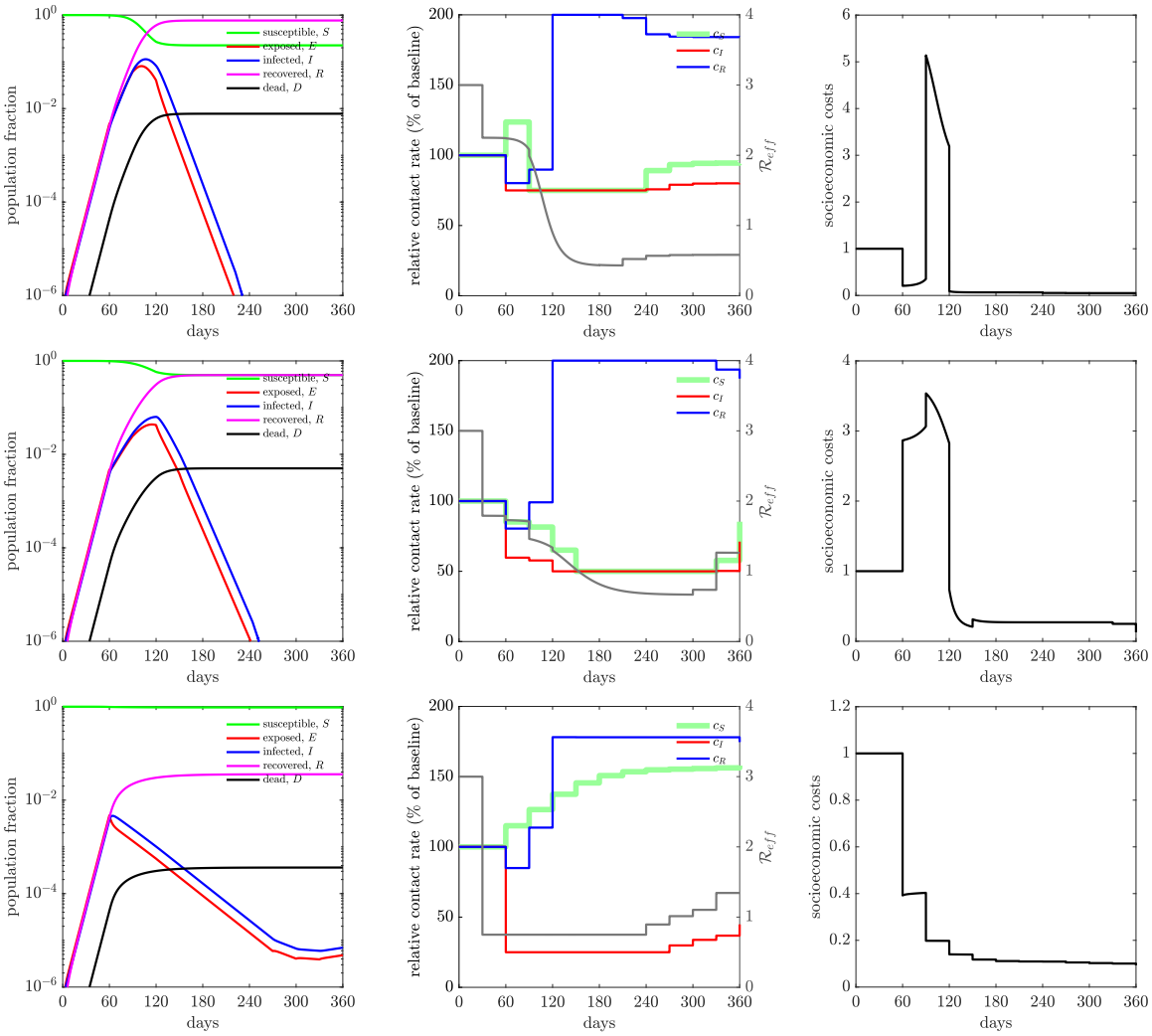

Figure 4.12: Population dynamics in a SEIR model with mis-timed control policy for various isolation efficiencies: (Top) 25% isolation efficiency; (Middle) 50% isolation efficiency and (Bottom) 75% isolation efficiency. The relative importance (ξ) is 1 for all the cases. The optimal control policy is computed for a system one month after an outbreak. Then, we enforce the optimal control policy 30 days later, *i.e.,* at the end of 60 days after the start of the outbreak. The contact rate interventions start at 60 days. The total deaths and working fraction for the delayed system are presented in Table 4.1 for various isolation efficiencies. The optimal control policies and their corresponding dynamics without mistiming are shown in the middle row of Figs. 4.9, 4.10, 4.11.

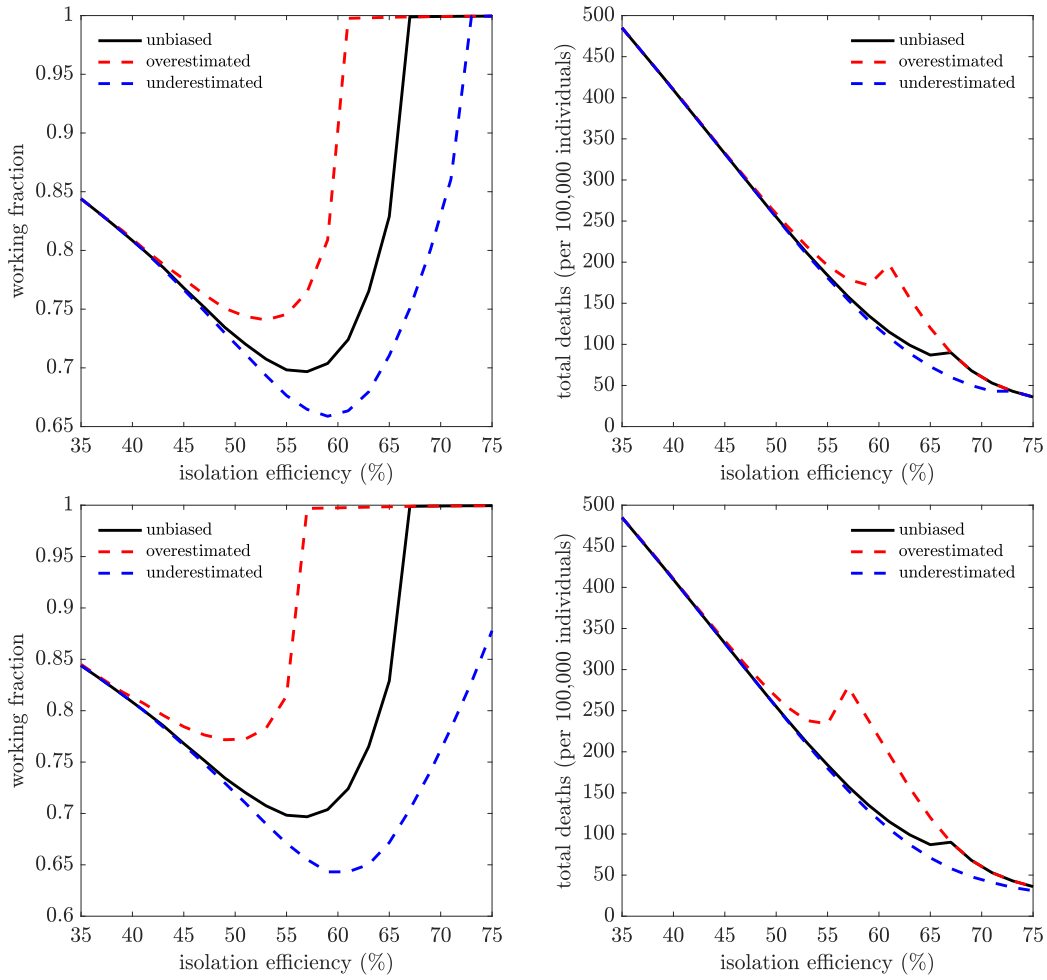

Figure 4.13: Health and economic outcomes of the feedback control system with estimation error in isolation efficiency. The shielding level is fixed at 2, the isolation efficiency varies from 35% to 75% with a 2% increment. (Top) Low uncertainty case. The range of uncertainty is $+/-6\%$, i.e., $\epsilon = 6$. The blue dashed lines represent the working fraction and total death for the system outputs with 6% higher isolation efficiency. The red dashed lines represent the working fraction and total death for the system outputs with 6% lower isolation efficiency. The black lines represent system outputs without mis-specification in isolation efficiency. (Bottom) High uncertainty case. The range of uncertainty is $+/-10\%$, i.e., $\epsilon = 10$. The blue dashed lines represent the working fraction and total death for the system outputs with 10% higher isolation efficiency. The red dashed lines are the working fraction and total death for the system outputs with 10% lower isolation efficiency. The black lines represent system outputs without mis-specification on isolation efficiency.

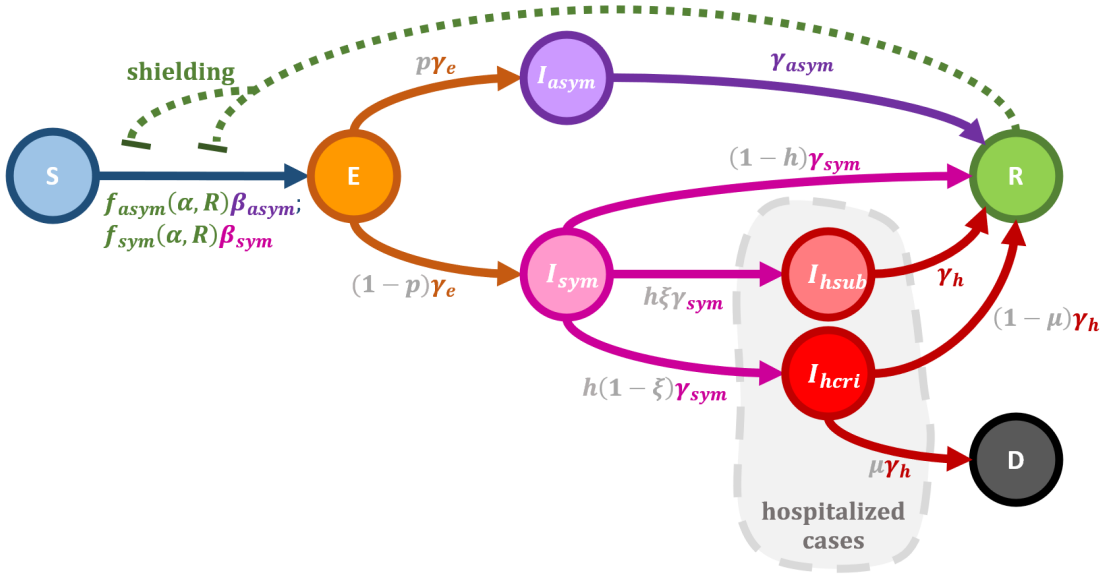

Figure 4.14: Model schematic of system (4.21). We consider a population susceptible individuals (S), interacting with infected (I_{sym}, I_{asym}) and recovered (R) individuals. Interactions between susceptible and infectious individuals lead to new exposed cases (E). Exposed individuals undergo a period of latency before disease onset, which are symptomatic (I_{sym}) or asymptomatic (I_{asym}). A subset of symptomatic individuals require hospitalization (I_h) which we further categorize as acute/subcritical (I_{hsub}) and critical (I_{hcri}) cases, the latter of which can be fatal. Individuals who recover can then mitigate the rate of new exposure cases by interaction substitution - what we denote as *immune shielding* - by modulating the rate of susceptible-infectious interactions by $f_{asym}(\alpha, R)$ and $f_{sym}(\alpha, R)$ respectively, where $f_{asym}(\alpha, R) = \frac{S(a)I_{asym,tot}}{N_{tot}+\alpha R_{shields}}$. Here, the tot subscript denotes the total number of cases across all ages, *i.e.*, $I_{sym,tot} = \sum_a I_{sym}(a)$.

4.5 Appendix

4.5.1 Control system parameter optimization

Consider the differential equation

$$\dot{x}(t) = f(x(t); \theta), \tag{4.26}$$

where $t \in [t_0, t_f]$, with initial condition $x(t_0) = x_0$ and parameter vector θ, and define $\mathcal{J}$ by

$$\mathcal{J}(\theta) = \psi(\theta) + \int_{t_0}^{t_f} L(x(t), \theta)\, dt + \phi(x(t_f), \theta). \tag{4.27}$$

Here $x(t) \in \mathbb{R}^n$, $\theta \in \mathbb{R}^p$, $f : \mathbb{R}^n \times \mathbb{R}^p \to \mathbb{R}^n$, $L : \mathbb{R}^n \times \mathbb{R}^p \to \mathbb{R}$, $\phi : \mathbb{R}^n \times \mathbb{R}^p \to \mathbb{R}$, and $\psi : \mathbb{R}^p \to \mathbb{R}$. Considering $\mathcal{J}(\theta)$ as a function of θ, then, we derive expression for the derivative $d\mathcal{J}/d\theta$ in terms of a costate. Denote $x_\theta(t)$ and $x_{\theta+\Delta\theta}(t)$ as the corresponding state trajectory with model parameter θ and $\theta + \Delta\theta$ respectively, and $\Delta x_\theta(t) = x_{\theta+\Delta\theta}(t) - x_\theta(t)$. Note that $\theta + \Delta\theta$ is in a sufficiently small neighborhood of θ. The first order difference in cost function is

$$\begin{aligned}
\Delta\mathcal{J} &= \mathcal{J}(\theta + \Delta\theta) - \mathcal{J}(\theta) \\
&= \psi(\theta + \Delta\theta) - \psi(\theta) + \int_{t_0}^{t_f} L(x_{\theta+\Delta\theta}(t), \theta + \Delta\theta) - L(x_\theta(t), \theta)\, dt \\
&+ \phi(x_{\theta+\Delta\theta}(t_f), \theta + \Delta\theta) - \phi(x_\theta(t_f), \theta) \\
&= \frac{d\psi}{d\theta}(\theta)\Delta\theta + \int_{t_0}^{t_f} \frac{dL}{dx}(x_\theta(t), \theta)\Delta x_\theta(t) + \frac{dL}{d\theta}(x_\theta(t), \theta)\Delta\theta\, dt \\
&+ \frac{d\phi}{dx}(x_\theta(t_f), \theta)\Delta x_\theta(t_f) + \frac{d\phi}{d\theta}(x_\theta(t_f), \theta)\Delta\theta \ + \text{higher-order terms.}
\end{aligned} \tag{4.28}$$

The governing dynamics of difference term $\Delta x_\theta(t)$ is

$$\begin{aligned}\dot{\Delta x_\theta} &= \dot{x_{\theta+\Delta\theta}} - \dot{x_\theta} \\ &= f(x_{\theta+\Delta\theta}; \theta+\Delta\theta) - f(x_\theta;\theta) \\ &= \underbrace{\frac{\partial f}{\partial x}(x_\theta(t);\theta)}_{n\times n}\underbrace{\Delta x_\theta}_{n\times 1} + \underbrace{\frac{\partial f}{\partial \theta}(x_\theta(t);\theta)}_{n\times p}\underbrace{\Delta\theta}_{p\times 1} + \text{higher-order terms},\end{aligned} \tag{4.29}$$

where initial condition is $\Delta x_\theta(t_0) = 0$. Neglecting higher order terms and using the state-transition matrix $\Phi(t,\tau) \in \mathbb{R}^{n\times n}$, the solution is

$$\Delta x_\theta(t) = \int_{t_0}^{t} \Phi(t,\tau)\frac{\partial f}{\partial \theta}(x_\theta(\tau);\theta)\Delta\theta \, d\tau. \tag{4.30}$$

Then, we plug Eq. 4.30 in Eq. 4.28 to obtain (drop higher order terms),

$$\begin{aligned}\Delta\mathcal{J} = \frac{d\psi}{d\theta}(\theta)\Delta\theta &+ \int_{t_0}^{t_f}\left[\frac{dL}{dx}(x_\theta(t))\int_{t_0}^{t}\Phi(t,\tau)\frac{\partial f}{\partial\theta}(x_\theta(\tau);\theta)\Delta\theta\, d\tau\right] + \frac{dL}{d\theta}(x_\theta(t),\theta)\Delta\theta\, dt \\ &+ \frac{d\phi}{dx}(x_\theta(t_f))\int_{t_0}^{t_f}\Phi(t,\tau)\frac{\partial f}{\partial\theta}(x_\theta(\tau);\theta)\Delta\theta\, d\tau + \frac{d\phi}{d\theta}(x_\theta(t_f),\theta)\Delta\theta\end{aligned} \tag{4.31}$$

Changing the order of integral for the second term of right hand side (RHS), we have

$$\begin{aligned}\Delta\mathcal{J} = \frac{d\psi}{d\theta}(\theta)\Delta\theta &+ \int_{t_0}^{t_f}\left[\int_{\tau}^{t_f}\frac{dL}{dx}(x_\theta(t))\Phi(t,\tau)\, dt\right]\frac{\partial f}{\partial\theta}(x_\theta(\tau);\theta)\Delta\theta\, d\tau \\ &+ \int_{t_0}^{t_f}\frac{dL}{d\theta}(x_\theta(\tau),\theta)\Delta\theta\, d\tau \\ &+ \int_{t_0}^{t_f}\frac{d\phi}{dx}(x_\theta(t_f))\Phi(t_f,\tau)\frac{\partial f}{\partial\theta}(x_\theta(\tau);\theta)\Delta\theta\, d\tau \\ &+ \frac{d\phi}{d\theta}(x_\theta(t_f),\theta)\Delta\theta.\end{aligned} \tag{4.32}$$

Hence, the derivative (first-order variation) is

$$\begin{aligned}\frac{d\mathcal{J}}{d\theta} = &\int_{t_0}^{t_f} \left[\int_{\tau}^{t_f} \frac{dL}{dx}(x_\theta(t))\Phi(t,\tau)\, dt\right] \frac{\partial f}{\partial \theta}(x_\theta(\tau);\theta) + ... \\ &... + \frac{d\phi}{dx}(x_\theta(t_f))\Phi(t_f,\tau)\frac{\partial f}{\partial \theta}(x_\theta(\tau);\theta) + \frac{dL}{d\theta}(x_\theta(\tau),\theta)\, d\tau \\ &+ \frac{d\psi}{d\theta}(\theta) + \frac{d\phi}{d\theta}(x_\theta(t_f),\theta).\end{aligned} \tag{4.33}$$

Define the costate $\lambda(\tau) \in \mathbb{R}^n$ as

$$\lambda^T(\tau) = \int_{\tau}^{t_f} \frac{dL}{dx}(x_\theta(t))\Phi(t,\tau)\, dt + \frac{d\phi}{dx}(x_\theta(t_f))\Phi(t_f,\tau). \tag{4.34}$$

Note that

$$\dot{\lambda^T}(\tau) = -\lambda^T(\tau)\frac{\partial f}{\partial x}(x_\theta(\tau);\theta) - \frac{dL}{dx}(x_\theta(\tau)), \tag{4.35}$$

with terminal condition $\lambda^T(t_f) = \frac{d\phi}{dx}(x_\theta(t_f))$. Then, Eq. 4.33 can be rewritten in terms of costate

$$\frac{d\mathcal{J}}{d\theta} = \frac{d\psi}{d\theta}(\theta) + \frac{d\phi}{d\theta}(x_\theta(t_f),\theta) + \int_{t_0}^{t_f} \lambda^T(\tau)\frac{\partial f}{\partial \theta}(x_\theta(\tau);\theta) + \frac{dL}{d\theta}(x_\theta(\tau),\theta)\, d\tau. \tag{4.36}$$

4.5.2 Supplementary tables

Parameter	Meaning	Value
η_I	Measure of disease transmission effectiveness	0.1
T_E	Mean incubation period	4 days
T_I	Mean infectious period	6 days
μ	Case fatality ratio of infected cases	0.01
c_B	Baseline potentially infectious contact rate	5/day
$\mathcal{R}_0$	Basic reproduction number	3
r	early exponential growth rate	0.15/day

Table 4.3: Epidemiological characteristics for SEIR model (4.2).

Parameter	Meaning	Value
W_1	Weight of $\mathcal{E}_1$	1
W_2	Weight matrix of $\mathcal{E}_2$	$0.1\mathcal{I}$, $\mathcal{I}$ is identify matrix
W_I	Weight of infection control cost	10^4
W_D	Weight of final deaths cost	10^5
K	Shape parameter in exponential function $\mathcal{E}_1$	7
$\widetilde{w}$	weight of final deaths in heuristic cost	5×10^2

Table 4.4: Weight regulators and optimization parameters.

Parameter	Meaning	Value
β_a	Asymptomatic transmission	0.3/day
β_s	Symptomatic transmission	0.6/day
$1/\gamma_e$	Mean exposed period	4 days
$1/\gamma_a$	Mean asymptomatic period	4 (low) and 6 (high) days
$1/\gamma_s$	Mean symptomatic period	4 (low) and 6 (high) days
$1/\gamma_h$	Mean hospital period	10 days
$\mathcal{R}_0$	Basic reproduction number	1.57 (low) and 2.33 (high)

Table 4.5: Epidemiological characteristics for age-structure model (4.21). Parameters based on [57, 116]

Age	Frac. Population f	Frac. Asymp p	Hospital Frac. h	ICU Frac. ξ
0-9	0.12	0.95	0.001	0.05
10-19	0.14	0.95	0.003	0.05
20-29	0.14	0.9	0.012	0.05
30-39	0.13	0.8	0.032	0.05
40-49	0.13	0.7	0.049	0.063
50-59	0.13	0.6	0.102	0.122
60-69	0.10	0.4	0.166	0.274
70-79	0.06	0.2	0.243	0.432
80-89	0.04	0.2	0.273	0.709
90-99	0.01	0.2	0.273	0.709

Table 4.6: Age-stratified risk for COVID-19. Of note, the model assumes that 50% of ICU cases die. Parameters based on [57, 117, 116, 118, 119].

CHAPTER 5

CONCLUSIONS

In this thesis, we applied mathematical tools of optimization and control to identify and propose management and decisions for virus-host systems at multiple scales, from microbial systems to epidemiological systems. Optimization and control applied to virus-host systems also provide valuable insights into the application of optimization principle to more general complex biological systems.

5.1 Rational design of phage therapy

Bacteriophage therapy is increasingly being put to the test – both in the lab and in compassionate use cases in the clinic. In practice, clinical use of phage often involves the application of multiple therapeutic phage, either together or sequentially. In Chapters 2 and 3, our results give practical insights on how to rationally and optimally design phage therapy via integrating computational modeling with control theory.

The theoretical framework presented in Chapter 2 is intended to help advance the rational design of monophage and phage cocktail therapy. Phage cocktails have been proposed as a solution to tackle phage resistance and broaden the antimicrobial spectrum of phage preparations [3, 120, 121], but it is often unclear how to optimize their composition to obtain maximum effectiveness. Part of the difficulty in determining the appropriate dosage and composition of phage treatments is due to the self-amplifying nature of phage. Our work demonstrates how control theory can be applied to optimize the dose and timing of therapeutic agents that have the ability to proliferate *in vivo*, find the minimal phage dosage required to eliminate bacteria, and provide insights, both of a conceptual and practical nature, in the development of phage therapy. In contrast to the observed failure of single-strain phage therapy in immunodeficient hosts due to phage resistance [69], our optimal control

analysis shows that the optimized treatment with a two-phage cocktail, one strain of which is a counter-resistant phage, can restore therapeutic efficacy in immunodeficient hosts. The framework can also be extended to other therapeutic contexts with replicating agents, such as the use of probiotic bacteria [122, 123], as well as cancer therapies involving oncolytic viruses [124, 125] and live immune cells [126, 127].

To mitigate the risk of using cocktails of different phage (could potentially lead to the emergence of bacteria simultaneously resistance to all injected phage), we proposed an initial condition optimization framework (*i.e.,* 'early-hit', phage cocktails are injected at start of treatment) to exploit how to efficiently utilize the 'future' phage (*i.e.,* identified in the aforementioned phage therapy experiments) to clear the bacterial infections. The results in Chapter 3 provide important insights to guide the phage therapy in complex eco-evolutionary dynamics. The cocktail treatment that contains contingent specialist phage is a 'double-edged sword', the treatment should be administrated carefully due to the interplay between competitive release and multi-resistance emergence. The cocktail treatment with generalist phage seems to be favorable as much less phage are required to eliminate bacterial cells. During the treatment, total bacterial density might increase to high level which could be detrimental to the host before the bacterial population is eliminated. Clinical researchers may have to be particularly careful in considering the dynamical consequences of nonlinear feedback mechanisms arising from the use of generalist phage in a therapeutic context.

Altogether, Chapters 2 and 3 provide principled control and optimization frameworks for devising evolutionarily robust phage cocktails and delivery schedules to control the bacterial populations. We hope the theoretical and computational frameworks developed in this thesis can facilitate the development and deployment of therapeutic phage cocktails for future clinical translation.

5.2 Epidemics, behavior, and policy

It is evident that strategic interventions are needed to mitigate against COVID-19 and future pandemics. Our approach presented in Chapter 4 is enabled by extending phenomenological SEIR like models to a framework that explicitly incorporates disease-dependent contact rates, *i.e.,* human behavior while aiming to jointly optimize public health and economic outcomes. First, our framework goes beyond an optimal control framework to develop a feedback control approach that is robust to mis-timing of applications and, robust to mis-specification of the modeled vs. realized level of isolation efficiency. Second, the increase in test capacity has revealed the potential to control outbreaks when used at scale. Third, we show that testing for virus alone (via a PCR or antigen approach) is sufficient to switch from *en masse* to individualized policies; a process that can be augmented by serological testing but does not require 100% coverage to achieve qualitatively improved outcomes.

We recognize that the epidemiological intervention model (a SEIR framework) and control frameworks used in Chapter 4 are intentionally simplified. The extensions and applications of the present model will require consideration of additional epidemic complexities (e.g., asymptomatic transmission), pharmaceutical interventions (e.g., large-scale vaccination) and additional evaluation of joint public health and economic costs (e.g., arising from hospitalization burden). The explicit consideration of test status (for both virus and antibodies) should also be part of future work to scale the concepts here into practice [102]. On the other hand, the feedback control framework solves the issue of model mis-specification (fragility w.r.t. parameters of the model) to some degree (better than optimal control). However, a full treatment, including estimation methods that incorporates gaps between prediction and measurement as a means to refine state specification is in fact a target for extensions of this research initiative.

Our work advances the foundation for practical interventions, providing novel and timely evidence that large-scale testing for infected and recovery status can help reduce

the risk of transmission for all and enable safer economic re-engagement. We hope our work will provide a framework to mitigate future epidemics. We hope that the policymakers would also benefit from the focus on non-dichotomous approaches to action-taking that explicitly balances public health and economic outcomes in a single analytical framework.

5.3 Control of viral systems across scales

Our results showed that open-loop optimal control policies can significantly improve the decision-making processes in virus-host systems across scales under the assumption of exact model knowledge. This thesis tended to use optimal control as a starting point, but not the ending point. Moving beyond optimal control approach, here we used certain heuristics to make strategies and policies more robust to mis-estimates and mis-specifications (w.r.t system states and dynamics). To further advance and scale the conceptual efforts here into practice, in a more realistic scenario with uncertain data (e.g., with observation noise) and model mismatch, integrating control theoretic framework with a system identification module may lead to a more reliable performance (e.g., model predictive control, MPC). The system identification algorithm compares model and system output given the same control input, and leverages differences in output to refine the model specification [128]. For bacteria-phage-immune systems, the model parameters may vary in time, e.g., infection networks and life-history traits may evolve due to mutations and extinctions. We need to collect experimental measurements to update the model (via computational Bayesian frameworks, e.g., particle Markov Chain Monte Carlo [129, 130]) and adjust control accordingly. While for epidemiological systems, the isolation efficiency and other epidemiological characteristics may vary in time due to the attention, awareness and preparedness of pandemics [105]. As such, the individualized control policy should be updated frequently via a predictive control framework (e.g., MPC) using new data (e.g., new cases, fatalities, released government public health news).

Altogether, we hope the optimization- and control-theoretic frameworks developed in

this thesis shed light on more general disease control problems, and provide a path forward for combining systems-model refinement via model-data integration.

REFERENCES

[1] J. O'neill, "Antimicrobial resistance: Tackling a crisis for the health and wealth of nations," *Review on antimicrobial resistance*, vol. 1, no. 1, pp. 1–16, 2014.

[2] K. E. Kortright, B. K. Chan, J. L. Koff, and P. E. Turner, "Phage therapy: A renewed approach to combat antibiotic-resistant bacteria," *Cell Host & Microbe*, vol. 25, no. 2, pp. 219–232, 2019.

[3] B. K. Chan, S. T. Abedon, and C. Loc-Carrillo, "Phage cocktails and the future of phage therapy," *Future Microbiology*, vol. 8, no. 6, pp. 769–783, 2013.

[4] E. M. Kutter, S. J. Kuhl, and S. T. Abedon, "Re-establishing a place for phage therapy in western medicine," *Future Microbiology*, vol. 10, no. 5, pp. 685–688, 2015.

[5] R. Young and J. J. Gill, "Phage therapy redux-—what is to be done?" *Science*, vol. 350, no. 6265, pp. 1163–1164, 2015.

[6] C. R. Merril, D. Scholl, and S. L. Adhya, "The prospect for bacteriophage therapy in western medicine," *Nature Reviews Drug Discovery*, vol. 2, no. 6, p. 489, 2003.

[7] B. K. Chan, M. Sistrom, J. E. Wertz, K. E. Kortright, D. Narayan, and P. E. Turner, "Phage selection restores antibiotic sensitivity in mdr pseudomonas aeruginosa," *Scientific Reports*, vol. 6, p. 26 717, 2016.

[8] B. K. Chan, P. E. Turner, S. Kim, H. R. Mojibian, J. A. Elefteriades, and D. Narayan, "Phage treatment of an aortic graft infected with pseudomonas aeruginosa," *Evolution, Medicine, and Public Health*, vol. 2018, no. 1, pp. 60–66, 2018.

[9] R. T. Schooley, B. Biswas, J. J. Gill, A. Hernandez-Morales, J. Lancaster, L. Lessor, J. J. Barr, S. L. Reed, F. Rohwer, S. Benler, *et al.*, "Development and use of personalized bacteriophage-based therapeutic cocktails to treat a patient with a disseminated resistant acinetobacter baumannii infection," *Antimicrobial Agents and Chemotherapy*, vol. 61, no. 10, e00954–17, 2017.

[10] F. Forti, D. R. Roach, M. Cafora, M. E. Pasini, D. S. Horner, E. V. Fiscarelli, M. Rossitto, L. Cariani, F. Briani, L. Debarbieux, and D. Ghisotti, "Design of a broad-range bacteriophage cocktail that reduces pseudomonas aeruginosa biofilms and treats acute infections in two animal models," *Antimicrobial Agents and Chemotherapy*, vol. 62, no. 6, 2018.

[11] N. Dufour, R. Delattre, A. Chevallereau, J.-D. Ricard, and L. Debarbieux, "Phage therapy of pneumonia is not associated with an overstimulation of the inflamma-

tory response compared to antibiotic treatment in mice," *Antimicrobial Agents and Chemotherapy*, vol. 63, no. 8, 2019.

[12] S. McCallin, J. C. Sacher, J. Zheng, and B. K. Chan, "Current state of compassionate phage therapy," *Viruses*, vol. 11, no. 4, 2019.

[13] R. M. Dedrick, C. A. Guerrero-Bustamante, R. A. Garlena, D. A. Russell, K. Ford, K. Harris, K. C. Gilmour, J. Soothill, D. Jacobs-Sera, R. T. Schooley, *et al.*, "Engineered bacteriophages for treatment of a patient with a disseminated drug-resistant mycobacterium abscessus," *Nature Medicine*, vol. 25, no. 5, p. 730, 2019.

[14] S. Jennes, M. Merabishvili, P. Soentjens, K. W. Pang, T. Rose, E. Keersebilck, O. Soete, P.-M. François, S. Teodorescu, G. Verween, *et al.*, "Use of bacteriophages in the treatment of colistin-only-sensitive pseudomonas aeruginosa septicaemia in a patient with acute kidney injury—a case report," *Critical Care*, vol. 21, no. 1, p. 129, 2017.

[15] S. A. Sarker, S. Sultana, G. Reuteler, D. Moine, P. Descombes, F. Charton, G. Bourdin, S. McCallin, C. Ngom-Bru, T. Neville, *et al.*, "Oral phage therapy of acute bacterial diarrhea with two coliphage preparations: A randomized trial in children from bangladesh," *EBioMedicine*, vol. 4, pp. 124–137, 2016.

[16] P. Jault, T. Leclerc, S. Jennes, J. P. Pirnay, Y.-A. Que, G. Resch, A. F. Rousseau, F. Ravat, H. Carsin, R. L. Floch, J. V. Schaal, C. Soler, C. Fevre, I. Arnaud, L. Bretaudeau, and J. Gabard, "Efficacy and tolerability of a cocktail of bacteriophages to treat burn wounds infected by pseudomonas aeruginosa (phagoburn): A randomised, controlled, double-blind phase 1/2 trial," *The Lancet Infectious Diseases*, vol. 19, no. 1, pp. 35–45, 2019.

[17] S. K. Sahani and S. Gakkhar, "A mathematical model for phage therapy with impulsive phage dose," *Differential Equations and Dynamical Systems*, pp. 1–12, 2016.

[18] R. V. Culshaw, S. Ruan, and R. J. Spiteri, "Optimal HIV treatment by maximising immune response," *Journal of Mathematical Biology*, vol. 48, no. 5, pp. 545–562, 2004.

[19] T. Jang, H.-D. Kwon, and J. Lee, "Free terminal time optimal control problem of an HIV model based on a conjugate gradient method," *Bulletin of Mathematical Biology*, vol. 73, no. 10, pp. 2408–2429, 2011.

[20] A.-M. Croicu, "Short-and long-term optimal control of a mathematical model for HIV infection of $CD4^{+}$T cells," *Bulletin of Mathematical Biology*, vol. 77, no. 11, pp. 2035–2071, 2015.

[21] A.-M. Croicu, A. M. Jarrett, N. Cogan, and M. Y. Hussaini, "Short-term antiretroviral treatment recommendations based on sensitivity analysis of a mathematical model for HIV infection of $CD4^+T$ cells," *Bulletin of Mathematical Biology*, vol. 79, no. 11, pp. 2649–2671, 2017.

[22] R. Peña-Miller, D. Lähnemann, H. Schulenburg, M. Ackermann, and R. Beardmore, "Selecting against antibiotic-resistant pathogens: Optimal treatments in the presence of commensal bacteria," *Bulletin of Mathematical Biology*, vol. 74, no. 4, pp. 908–934, 2012.

[23] J. J. Thibodeaux and T. P. Schlittenhardt, "Optimal treatment strategies for malaria infection," *Bulletin of Mathematical Biology*, vol. 73, no. 11, pp. 2791–2808, 2011.

[24] F. Castiglione and B. Piccoli, "Optimal control in a model of dendritic cell transfection cancer immunotherapy," *Bulletin of Mathematical Biology*, vol. 68, no. 2, pp. 255–274, 2006.

[25] L. G. de Pillis, K. R. Fister, W. Gu, T. Head, K. Maples, T. Neal, A. Murugan, and K. Kozai, "Optimal control of mixed immunotherapy and chemotherapy of tumors," *Journal of Biological systems*, vol. 16, no. 01, pp. 51–80, 2008.

[26] U. Ledzewicz, M. Naghnaeian, and H. Schättler, "Optimal response to chemotherapy for a mathematical model of tumor–immune dynamics," *Journal of Mathematical Biology*, vol. 64, no. 3, pp. 557–577, 2012.

[27] K. Blayneh, Y. Cao, and H.-D. Kwon, "Optimal control of vector-borne diseases: Treatment and prevention," *Discrete and Continuous Dynamical Systems B*, vol. 11, no. 3, pp. 587–611, 2009.

[28] R. L. M. Neilan, E. Schaefer, H. Gaff, K. R. Fister, and S. Lenhart, "Modeling optimal intervention strategies for cholera," *Bulletin of Mathematical Biology*, vol. 72, no. 8, pp. 2004–2018, 2010.

[29] A.-M. Croicu, "An optimal control model to reduce and eradicate anthrax disease in herbivorous animals," *Bulletin of Mathematical Biology*, vol. 81, no. 1, pp. 235–255, 2019.

[30] R. Rowthorn and S. Walther, "The optimal treatment of an infectious disease with two strains," *Journal of Mathematical Biology*, vol. 74, no. 7, pp. 1753–1791, 2017.

[31] G. Li, C. Y. Leung, Y. Wardi, L. Debarbieux, and J. S. Weitz, "Optimizing the timing and composition of therapeutic phage cocktails: A control-theoretic approach," *Bulletin of Mathematical Biology*, vol. 82, no. 6, pp. 1–29, 2020.

[32] M. Henry, R. Lavigne, and L. Debarbieux, "Predicting in vivo efficacy of therapeutic bacteriophages used to treat pulmonary infections," *Antimicrobial agents and chemotherapy*, vol. 57, no. 12, pp. 5961–5968, 2013.

[33] K. E. Kortright, B. K. Chan, J. L. Koff, and P. E. Turner, "Phage therapy: A renewed approach to combat antibiotic-resistant bacteria," *Cell host & microbe*, vol. 25, no. 2, pp. 219–232, 2019.

[34] J. M. Borin, S. Avrani, J. E. Barrick, K. L. Petrie, and J. R. Meyer, "Coevolutionary phage training leads to greater bacterial suppression and delays the evolution of phage resistance," *bioRxiv*, 2020.

[35] W. H. Organization *et al.*, "Covid-19 weekly epidemiological update, 9 march 2021," 2021.

[36] S. Flaxman, S. Mishra, A. Gandy, H. J. T. Unwin, T. A. Mellan, H. Coupland, C. Whittaker, H. Zhu, T. Berah, J. W. Eaton, *et al.*, "Estimating the effects of non-pharmaceutical interventions on covid-19 in europe," *Nature*, vol. 584, no. 7820, pp. 257–261, 2020.

[37] M. Chinazzi, J. T. Davis, M. Ajelli, C. Gioannini, M. Litvinova, S. Merler, A. P. y Piontti, K. Mu, L. Rossi, K. Sun, *et al.*, "The effect of travel restrictions on the spread of the 2019 novel coronavirus (covid-19) outbreak," *Science*, vol. 368, no. 6489, pp. 395–400, 2020.

[38] C. R. Wells, P. Sah, S. M. Moghadas, A. Pandey, A. Shoukat, Y. Wang, Z. Wang, L. A. Meyers, B. H. Singer, and A. P. Galvani, "Impact of international travel and border control measures on the global spread of the novel 2019 coronavirus outbreak," *Proceedings of the National Academy of Sciences*, vol. 117, no. 13, pp. 7504–7509, 2020.

[39] B. J. Cowling, S. T. Ali, T. W. Ng, T. K. Tsang, J. C. Li, M. W. Fong, Q. Liao, M. Y. Kwan, S. L. Lee, S. S. Chiu, *et al.*, "Impact assessment of non-pharmaceutical interventions against coronavirus disease 2019 and influenza in hong kong: An observational study," *The Lancet Public Health*, vol. 5, no. 5, e279–e288, 2020.

[40] N. Ferguson, D. Laydon, G. Nedjati Gilani, N. Imai, K. Ainslie, M. Baguelin, S. Bhatia, A. Boonyasiri, Z. Cucunuba Perez, G. Cuomo-Dannenburg, *et al.*, "Report 9: Impact of non-pharmaceutical interventions (npis) to reduce covid19 mortality and healthcare demand," 2020.

[41] M. U. Kraemer, C.-H. Yang, B. Gutierrez, C.-H. Wu, B. Klein, D. M. Pigott, L. Du Plessis, N. R. Faria, R. Li, W. P. Hanage, *et al.*, "The effect of human mobility and control measures on the covid-19 epidemic in china," *Science*, vol. 368, no. 6490, pp. 493–497, 2020.

[42] R. Zhang, Y. Li, A. L. Zhang, Y. Wang, and M. J. Molina, "Identifying airborne transmission as the dominant route for the spread of covid-19," *Proceedings of the National Academy of Sciences*, vol. 117, no. 26, pp. 14 857–14 863, 2020.

[43] P. G. Walker, C. Whittaker, O. J. Watson, M. Baguelin, P. Winskill, A. Hamlet, B. A. Djafaara, Z. Cucunubá, D. O. Mesa, W. Green, *et al.*, "The impact of covid-19 and strategies for mitigation and suppression in low-and middle-income countries," *Science*, vol. 369, no. 6502, pp. 413–422, 2020.

[44] D. Allain-Dupré, I. Chatry, V. Michalun, and A. Moisio, *The territorial impact of covid-19: Managing the crisis across levels of government*, 2020.

[45] T. Greenhalgh, M. B. Schmid, T. Czypionka, D. Bassler, and L. Gruer, "Face masks for the public during the covid-19 crisis," *Bmj*, vol. 369, 2020.

[46] D. K. Chu, E. A. Akl, S. Duda, K. Solo, S. Yaacoub, H. J. Schünemann, A. El-harakeh, A. Bognanni, T. Lotfi, M. Loeb, *et al.*, "Physical distancing, face masks, and eye protection to prevent person-to-person transmission of sars-cov-2 and covid-19: A systematic review and meta-analysis," *The Lancet*, vol. 395, no. 10242, pp. 1973–1987, 2020.

[47] E. Brynjolfsson, J. J. Horton, A. Ozimek, D. Rock, G. Sharma, and H.-Y. TuYe, "Covid-19 and remote work: An early look at us data," National Bureau of Economic Research, Tech. Rep., 2020.

[48] C. Bodkin, V. Mokashi, K. Beal, J. Wiwcharuk, R. Lennox, D. Guenter, M. Smieja, and T. O'Shea, "Pandemic planning in homeless shelters: A pilot study of a covid-19 testing and support program to mitigate the risk of covid-19 outbreaks in congregate settings," *Clinical Infectious Diseases*, 2020.

[49] S. Feng, C. Shen, N. Xia, W. Song, M. Fan, and B. J. Cowling, "Rational use of face masks in the covid-19 pandemic," *The Lancet Respiratory Medicine*, vol. 8, no. 5, pp. 434–436, 2020.

[50] V. C.-C. Cheng, S.-C. Wong, V. W.-M. Chuang, S. Y.-C. So, J. H.-K. Chen, S. Sridhar, K. K.-W. To, J. F.-W. Chan, I. F.-N. Hung, P.-L. Ho, *et al.*, "The role of community-wide wearing of face mask for control of coronavirus disease 2019 (covid-19) epidemic due to sars-cov-2," *Journal of Infection*, vol. 81, no. 1, pp. 107–114, 2020.

[51] A. Atkeson, M. C. Droste, M. Mina, and J. H. Stock, "Economic benefits of covid-19 screening tests," National Bureau of Economic Research, Tech. Rep., 2020.

[52] D. Baqaee, E. Farhi, M. J. Mina, and J. H. Stock, "Reopening scenarios," National Bureau of Economic Research, Tech. Rep., 2020.

[53] *Flattening the unemployment curve? policies to support workers' income and promote a speedy labour market recovery*, 2020.

[54] M. Douglas, S. V. Katikireddi, M. Taulbut, M. McKee, and G. McCartney, "Mitigating the wider health effects of covid-19 pandemic response," *Bmj*, vol. 369, 2020.

[55] S. Hsiang, D. Allen, S. Annan-Phan, K. Bell, I. Bolliger, T. Chong, H. Druckenmiller, L. Y. Huang, A. Hultgren, E. Krasovich, *et al.*, "The effect of large-scale anti-contagion policies on the covid-19 pandemic," *Nature*, vol. 584, no. 7820, pp. 262–267, 2020.

[56] J. F. Bonnans and J. Gianatti, "Optimal control techniques based on infection age for the study of the covid-19 epidemic," *Mathematical Modelling of Natural Phenomena*, vol. 15, p. 48, 2020.

[57] N. Ferguson *et al.*, *Impact of non-pharmaceutical interventions (NPIs) to reduce COVID19 mortality and healthcare demand*, 2020.

[58] D. H. Morris, F. W. Rossine, J. B. Plotkin, and S. A. Levin, "Optimal, near-optimal, and robust epidemic control," *arXiv preprint arXiv:2004.02209*, 2020.

[59] H. Zhao and Z. Feng, "Staggered release policies for covid-19 control: Costs and benefits of relaxing restrictions by age and risk," *Mathematical biosciences*, vol. 326, p. 108 405, 2020.

[60] G. Li, S. Shivam, M. E. Hochberg, Y. Wardi, and J. S. Weitz, "Disease-dependent interaction policies to support health and economic outcomes during the covid-19 epidemic," *Available at SSRN 3709833*,

[61] J. S. Weitz, S. J. Beckett, A. R. Coenen, D. Demory, M. Dominguez-Mirazo, J. Dushoff, C.-Y. Leung, G. Li, A. Măgălie, S. W. Park, *et al.*, "Modeling shield immunity to reduce covid-19 epidemic spread," *Nature medicine*, vol. 26, no. 6, pp. 849–854, 2020.

[62] H. L. Smith, "Models of virulent phage growth with application to phage therapy," *SIAM Journal on Applied Mathematics*, vol. 68, no. 6, pp. 1717–1737, 2008.

[63] R. J. Payne and V. A. Jansen, "Understanding bacteriophage therapy as a density-dependent kinetic process," *Journal of Theoretical Biology*, vol. 208, no. 1, pp. 37–48, 2001.

[64] S. Gakkhar and S. K. Sahani, "A time delay model for bacteria bacteriophage interaction," *Journal of Biological Systems*, vol. 16, no. 03, pp. 445–461, 2008.

[65] B. R. Levin and J. Bull, "Phage therapy revisited: The population biology of a bacterial infection and its treatment with bacteriophage and antibiotics," *The American Naturalist*, vol. 147, no. 6, pp. 881–898, 1996.

[66] B. R. Levin and J. J. Bull, "Population and evolutionary dynamics of phage therapy," *Nature Reviews Microbiology*, vol. 2, no. 2, pp. 166–173, 2004.

[67] W. Wang, "Dynamics of bacteria-phage interactions with immune response in a chemostat," *Journal of Biological Systems*, vol. 25, no. 04, pp. 697–713, 2017.

[68] C. Y. (Leung and J. S. Weitz, "Modeling the synergistic elimination of bacteria by phage and the innate immune system," *Journal of Theoretical Biology*, vol. 429, pp. 241–252, 2017.

[69] D. R. Roach, C. Y. Leung, M. Henry, E. Morello, D. Singh, J. P. Di Santo, J. S. Weitz, and L. Debarbieux, "Synergy between the host immune system and bacteriophage is essential for successful phage therapy against an acute respiratory pathogen," *Cell Host & Microbe*, vol. 22, no. 1, pp. 38–47, 2017.

[70] L. S. Pontryagin, *Mathematical theory of optimal processes*. Routledge, 2018.

[71] M. Hale, Y. Wardi, H. Jaleel, and M. Egerstedt, "Hamiltonian-based algorithm for optimal control," *arXiv preprint arXiv:1603.02747*, 2016.

[72] Y. Wardi, M. Egerstedt, and M. U. Qureshi, "Hamiltonian-based algorithm for relaxed optimal control," in *2016 IEEE 55th Conference on Decision and Control (CDC)*, IEEE, 2016, pp. 7222–7227.

[73] E. Beretta and Y. Kuang, "Modeling and analysis of a marine bacteriophage infection," *Mathematical Biosciences*, vol. 149, no. 1, pp. 57–76, 1998.

[74] W. H. Fleming and R. W. Rishel, *Deterministic and stochastic optimal control*. Springer Science & Business Media, 2012, vol. 1.

[75] E. Camacho, L. Melara, M. Villalobos, and S. Wirkus, "Optimal control in the treatment of retinitis pigmentosa," *Bulletin of Mathematical Biology*, vol. 76, no. 2, pp. 292–313, 2014.

[76] S. Boyd and L. Vandenberghe, *Convex optimization*. Cambridge University Press, 2004.

[77] J. Stoer and R. Bulirsch, *Introduction to numerical analysis*. Springer Science & Business Media, 2013, vol. 12.

[78] N. Hashemian and A. Armaou, "Stochastic mpc design for a two-component granulation process," in *2017 American Control Conference (ACC)*, IEEE, 2017, pp. 4386–4391.

[79] K. Hodyra-Stefaniak, P. Miernikiewicz, J. Drapała, M. Drab, E. Jończyk-Matysiak, D. Lecion, Z. Kaźmierczak, W. Beta, J. Majewska, M. Harhala, *et al.*, "Mammalian host-versus-phage immune response determines phage fate in vivo," *Scientific Reports*, vol. 5, p. 14 802, 2015.

[80] A. Go'rski, R. Miedzybrodzki, J. Borysowski, K. Dabrowska, P. Wierzbicki, M. Ohams, G. Korczak-Kowalska, N. Olszowska-Zaremba, M. Lusiak-Szelachowska, M. Klak, *et al.*, "Phage as a modulator of immune responses: Practical implications for phage therapy," in *Advances in virus research*, vol. 83, Elsevier, 2012, pp. 41–71.

[81] C. O. Flores, J. R. Meyer, S. Valverde, L. Farr, and J. S. Weitz, "Statistical structure of host–phage interactions," *Proceedings of the National Academy of Sciences*, vol. 108, no. 28, E288–E297, 2011.

[82] J. Weitz, *Quantitative viral ecology: dynamics of viruses and their microbial hosts*. Princeton University Press, 2016, vol. 55.

[83] S. J. Beckett and H. T. Williams, "Coevolutionary diversification creates nested-modular structure in phage–bacteria interaction networks," *Interface focus*, vol. 3, no. 6, p. 20 130 033, 2013.

[84] J. S. Weitz, H. Hartman, and S. A. Levin, "Coevolutionary arms races between bacteria and bacteriophage," *Proceedings of the National Academy of Sciences*, vol. 102, no. 27, pp. 9535–9540, 2005.

[85] F. Rodriguez-Valera, A.-B. Martin-Cuadrado, B. Rodriguez-Brito, L. Pasic, T. F. Thingstad, F. Rohwer, and A. Mira, "Explaining microbial population genomics through phage predation," *Nature Precedings*, pp. 1–1, 2009.

[86] A. R. Hall, P. D. Scanlan, A. D. Morgan, and A. Buckling, "Host–parasite coevolutionary arms races give way to fluctuating selection," *Ecology Letters*, vol. 14, no. 7, pp. 635–642, 2011.

[87] S. Gandon, A. Buckling, E. Decaestecker, and T. Day, "Host–parasite coevolution and patterns of adaptation across time and space," *Journal of evolutionary biology*, vol. 21, no. 6, pp. 1861–1866, 2008.

[88] B. Koskella and M. A. Brockhurst, "Bacteria–phage coevolution as a driver of ecological and evolutionary processes in microbial communities," *FEMS microbiology reviews*, vol. 38, no. 5, pp. 916–931, 2014.

[89] J. M. Broniewski, S. Meaden, S. Paterson, A. Buckling, and E. R. Westra, "The effect of phage genetic diversity on bacterial resistance evolution," *The ISME journal*, vol. 14, no. 3, pp. 828–836, 2020.

[90] A. R. Hall, P. D. Scanlan, and A. Buckling, "Bacteria-phage coevolution and the emergence of generalist pathogens," *The American Naturalist*, vol. 177, no. 1, pp. 44–53, 2011.

[91] B. J. Bohannan, B. Kerr, C. M. Jessup, J. B. Hughes, and G. Sandvik, "Trade-offs and coexistence in microbial microcosms," *Antonie Van Leeuwenhoek*, vol. 81, no. 1-4, pp. 107–115, 2002.

[92] L. M. Childs, N. L. Held, M. J. Young, R. J. Whitaker, and J. S. Weitz, "Multiscale model of crispr-induced coevolutionary dynamics: Diversification at the interface of lamarck and darwin," *Evolution: International Journal of Organic Evolution*, vol. 66, no. 7, pp. 2015–2029, 2012.

[93] H. T. Williams, "Phage-induced diversification improves host evolvability," *BMC evolutionary biology*, vol. 13, no. 1, p. 17, 2013.

[94] L. F. Jover, M. H. Cortez, and J. S. Weitz, "Mechanisms of multi-strain coexistence in host–phage systems with nested infection networks," *Journal of theoretical biology*, vol. 332, pp. 65–77, 2013.

[95] N. R. Record, D. Talmy, and S. Våge, "Quantifying tradeoffs for marine viruses," *Frontiers in Marine Science*, vol. 3, p. 251, 2016.

[96] W. L. Brown and E. O. Wilson, "Character displacement," *Systematic zoology*, vol. 5, no. 2, pp. 49–64, 1956.

[97] P. R. Grant, "Convergent and divergent character displacement," *Biological journal of the Linnean Society*, vol. 4, no. 1, pp. 39–68, 1972.

[98] F. Azevedo, R. A. Kraenkel, and D. P. da Silva, "Competitive release and area effects," *Ecological complexity*, vol. 11, pp. 154–159, 2012.

[99] J. West, Y. Ma, and P. K. Newton, "Capitalizing on competition: An evolutionary model of competitive release in metastatic castration resistant prostate cancer treatment," *Journal of Theoretical Biology*, vol. 455, pp. 249–260, 2018.

[100] J. West, L. You, J. Zhang, R. A. Gatenby, J. S. Brown, P. K. Newton, and A. R. Anderson, "Towards multidrug adaptive therapy," *Cancer research*, vol. 80, no. 7, pp. 1578–1589, 2020.

[101] F. Dercole and S. Rinaldi, *Analysis of evolutionary processes: the adaptive dynamics approach and its applications*. Princeton University Press, 2008, vol. 3.

[102] A. N. Kraay, K. N. Nelson, C. Y. Zhao, J. S. Weitz, and B. A. Lopman, "Modeling serological testing to inform relaxation of social distancing for covid-19 control," *medRxiv*,

[103] M. E. Hochberg, "Importance of suppression and mitigation measures in managing covid-19 outbreaks," *arXiv preprint arXiv:2005.03323*, 2020.

[104] M. Klompas, *Coronavirus disease 2019 (covid-19): Protecting hospitals from the invisible*, 2020.

[105] J. S. Weitz, S. W. Park, C. Eksin, and J. Dushoff, "Awareness-driven behavior changes can shift the shape of epidemics away from peaks and toward plateaus, shoulders, and oscillations," *Proceedings of the National Academy of Sciences*, vol. 117, no. 51, pp. 32 764–32 771, 2020.

[106] E. Franco, "A feedback sir (fsir) model highlights advantages and limitations of infection-based social distancing," *arXiv preprint arXiv:2004.13216*, 2020.

[107] A. L. Phelan, "Covid-19 immunity passports and vaccination certificates: Scientific, equitable, and legal challenges," *The Lancet*, vol. 395, no. 10237, pp. 1595–1598, 2020.

[108] O. F. Norheim, "Protecting the population with immune individuals," *Nature medicine*, vol. 26, no. 6, pp. 823–824, 2020.

[109] R. M. Anderson, B. Anderson, and R. M. May, *Infectious diseases of humans: dynamics and control*. Oxford university press, 1992.

[110] C. N. Ngonghala, E. Iboi, S. Eikenberry, M. Scotch, C. R. MacIntyre, M. H. Bonds, and A. B. Gumel, "Mathematical assessment of the impact of non-pharmaceutical interventions on curtailing the 2019 novel coronavirus," *arXiv preprint arXiv:2004.07391*, 2020.

[111] E. Polak, *Optimization Algorithms and Consistent Approximations*. Springer-Verlag, New York, New York, 1997.

[112] D. E. Kirk, *Optimal control theory: an introduction*. Courier Corporation, 2004.

[113] D. Liberzon, *Calculus of variations and optimal control theory: a concise introduction*. Princeton University Press, 2011.

[114] D. Whitley, "A genetic algorithm tutorial," *Statistics and computing*, vol. 4, no. 2, pp. 65–85, 1994.

[115] I. The MathWorks, *Global optimization toolbox*, Natick, Massachusetts, United State, 2020.

[116] J. T. Wu, K. Leung, M. Bushman, N. Kishore, R. Niehus, P. M. de Salazar, B. J. Cowling, M. Lipsitch, and G. M. Leung, "Estimating clinical severity of covid-19 from the transmission dynamics in wuhan, china," *Nature medicine*, vol. 26, no. 4, pp. 506–510, 2020.

[117] S. W. Park, D. M. Cornforth, J. Dushoff, and J. S. Weitz, "The time scale of asymptomatic transmission affects estimates of epidemic potential in the covid-19 outbreak," *Epidemics*, vol. 31, p. 100 392, 2020.

[118] J. T. Wu, K. Leung, and G. M. Leung, "Nowcasting and forecasting the potential domestic and international spread of the 2019-ncov outbreak originating in wuhan, china: A modelling study," *The Lancet*, vol. 395, no. 10225, pp. 689–697, 2020.

[119] R. Li, S. Pei, B. Chen, Y. Song, T. Zhang, W. Yang, and J. Shaman, "Substantial undocumented infection facilitates the rapid dissemination of novel coronavirus (sars-cov-2)," *Science*, vol. 368, no. 6490, pp. 489–493, 2020.

[120] Y. Tanji, T. Shimada, M. Yoichi, K. Miyanaga, K. Hori, and H. Unno, "Toward rational control of escherichia coli o157: H7 by a phage cocktail," *Applied Microbiology and Biotechnology*, vol. 64, no. 2, pp. 270–274, 2004.

[121] J. Zhang, B. L. Kraft, Y. Pan, S. K. Wall, A. C. Saez, and P. D. Ebner, "Development of an anti-salmonella phage cocktail with increased host range," *Foodborne Pathogens and Disease*, vol. 7, no. 11, pp. 1415–1419, 2010.

[122] W. Manzanares, M. Lemieux, P. L. Langlois, and P. E. Wischmeyer, "Probiotic and synbiotic therapy in critical illness: A systematic review and meta-analysis," *Critical Care*, vol. 20, no. 1, p. 262, 2016.

[123] E. A. Parker, T. Roy, C. R. D'Adamo, and L. S. Wieland, "Probiotics and gastrointestinal conditions: An overview of evidence from the cochrane collaboration," *Nutrition*, vol. 45, pp. 125–134, 2018.

[124] S. E. Lawler, M.-C. Speranza, C.-F. Cho, and E. A. Chiocca, "Oncolytic viruses in cancer treatment: A review," *JAMA oncology*, vol. 3, no. 6, pp. 841–849, 2017.

[125] H. Fukuhara, Y. Ino, and T. Todo, "Oncolytic virus therapy: A new era of cancer treatment at dawn," *Cancer Science*, vol. 107, no. 10, pp. 1373–1379, 2016.

[126] C. H. June, R. S. O'Connor, O. U. Kawalekar, S. Ghassemi, and M. C. Milone, "CAR T cell immunotherapy for human cancer," *Science*, vol. 359, no. 6382, pp. 1361–1365, 2018.

[127] K. F. Bol, G. Schreibelt, W. R. Gerritsen, I. J. M. De Vries, and C. G. Figdor, *Dendritic cell–based immunotherapy: State of the art and beyond*, 2016.

[128] L. Ljung, "System identification," *Wiley encyclopedia of electrical and electronics engineering*, pp. 1–19, 1999.

[129] C. Andrieu, A. Doucet, and R. Holenstein, "Particle markov chain monte carlo methods," *Journal of the Royal Statistical Society: Series B (Statistical Methodology)*, vol. 72, no. 3, pp. 269–342, 2010.

[130] A. Golightly and D. J. Wilkinson, "Bayesian parameter inference for stochastic biochemical network models using particle markov chain monte carlo," *Interface focus*, vol. 1, no. 6, pp. 807–820, 2011.